1-1-2013

# Structure and Coarsening of Foams: Beyond von Neumann's Law

Adam E. Roth
*University of Pennsylvania*, aeroth@sas.upenn.edu

# Structure and Coarsening of Foams: Beyond von Neumann's Law

**Abstract**
We report on the statistics of bubble size, topology, and shape and on their role in the coarsening dynamics for foams consisting of bubbles compressed between two parallel plates. We find that in the scaling regime, all bubble distributions are independent not only of time, but also of liquid content. For coarsening, the average rate decreases with liquid content due to the blocking of gas diffusion by Plateau borders inflated with liquid. By observing the growth rate of individual bubbles, we find that von Neumann's law becomes progressively violated with increasing wetness and decreasing bubble size. We successfully model this behavior by explicitly incorporating the border-blocking effect into the von Neumann argument.

We report on bubble growth rates and on the statistics of bubble topology for the coarsening of a dry foam contained in the gap between two hemispheres. By contrast with coarsening in flat space, we observe that six-sided bubbles grow with time at a rate that depends on their size. We measure the statistics of bubble topology, and find distributions that differ from the scaling state of a flat two dimensional foam.

We report on the statistics of bubble distribution and coarsening of the two dimensional surface of a three dimensional foam. The surface of a three dimensional foam obeys Plateau's laws, but does not obey von Neumann's law on the individual bubble level, although it holds on average. We measure bubble distributions, which to not change with time, but have different values from an ordinary two dimensional foam.

We report on a method for optical tomography of three dimensional foams. Using a bottle filled with dry foam that is mounted on a rotation stage, we take pictures of the foam at many different angles. Using these images, it is possible to reconstruct horizontal slices of the foam. By controlling the parameters of this system, it is possible to get good slices, for possible use in reconstruction of the foam structure.

**Degree Type**
Dissertation

**Degree Name**
Doctor of Philosophy (PhD)

**Graduate Group**
Physics & Astronomy

**First Advisor**
Douglas J. Durian

**Keywords**
Foam

**Subject Categories**
Physics

# STRUCTURE AND COARSENING OF FOAMS: BEYOND VON NEUMANN'S LAW

Adam E Roth

A DISSERTATION

in

Physics and Astronomy

Presented to the Faculties of the University of Pennsylvania

in

Partial Fulfillment of the Requirements for the

Degree of Doctor of Philosophy

2013

Douglas J. Durian, Professor of Physics and Astronomy
Supervisor of Dissertation

A.T. Charlie Johnson, Jr., Professor of Physics and Astronomy
Graduate Group Chairperson

Dissertation Committee
Randall D. Kamien, Professor of Physics and Astronomy
John C. Crocker, Associate Professor of Chemical and Biomolecular Engineering
Douglas J. Jerolmack, Assistant Professor of Earth and Environmental Science
Ravi K. Sheth, Professor of Physics and Astronomy

STRUCTURE AND COARSENING OF FOAMS: BEYOND VON NEUMANN'S LAW

# Acknowledgements

The work contained herein represents not just my own work, but a collaboration with many other people, without whom all this would not have been possible.

Chris Jones did much crucial work on the early stages of both the experiment on the effect of liquid content and the dome experiment. He helped design and build the apparatuses and helped me a lot with experimental technique.

Jennifer Reiser also worked on the early stages of the dome experiment. Her great skill in programming and image analysis was helpful to me at all stages of my work.

Klebert Feitosa was heavily involved in the optical tomography experiment, and that work is as much his as mine. He also worked closely with me at the early stages of my graduate studies and provided a strong role model of an experimental physicist.

Sal Torquato suggested applying a number of measurements used to characterize

point patterns to our foams. His expertise made it possible to do so.

Buddy Borders was always willing to help me in the machine shop. Every time I went I learned something new.

Bryan Chen provided hours of discussion specific to these projects, and helped me greatly with my understanding of foams in general. Whenever there was something I didn't understand, Bryan was an inexhaustible resource.

The entire Durian group was a helpful and friendly community that always gave me ideas and assistance whenever I needed it.

Finally, I would like to thank my advisor Doug. His guidance and patience have made me the scientist I am today.

ABSTRACT

STRUCTURE AND COARSENING OF FOAMS: BEYOND VON NEUMANN'S LAW

Adam E Roth

Douglas J. Durian

We report on the statistics of bubble size, topology, and shape and on their role in the coarsening dynamics for foams consisting of bubbles compressed between two parallel plates. We find that in the scaling regime, all bubble distributions are independent not only of time, but also of liquid content. For coarsening, the average rate decreases with liquid content due to the blocking of gas diffusion by Plateau borders inflated with liquid. By observing the growth rate of individual bubbles, we find that von Neumann's law becomes progressively violated with increasing wetness and decreasing bubble size. We successfully model this behavior by explicitly incorporating the border-blocking effect into the von Neumann argument.

We report on bubble growth rates and on the statistics of bubble topology for the coarsening of a dry foam contained in the gap between two hemispheres. By contrast with coarsening in flat space, we observe that six-sided bubbles grow with time at a rate that depends on their size. We measure the statistics of bubble topology, and find distributions that differ from the scaling state of a flat two dimensional foam.

We report on the statistics of bubble distribution and coarsening of the two dimensional surface of a three dimensional foam. The surface of a three dimensional foam obeys Plateau's laws, but does not obey von Neumann's law on the individual bubble level, although it holds on average. We measure bubble distributions, which to not change with time, but have different values from an ordinary two dimensional foam.

We report on a method for optical tomography of three dimensional foams. Using a bottle filled with dry foam that is mounted on a rotation stage, we take pictures of the foam at many different angles. Using these images, it is possible to reconstruct horizontal slices of the foam. By controlling the parameters of this system, it is possible to get good slices, for possible use in reconstruction of the foam structure.

# Contents

# List of Tables

# List of Figures

# Chapter 1

# Introduction

*Charm'd magic casements, opening on the foam*
*Of perilous seas, in faery lands forlorn*
-John Keats

Foams comprise a broad class of substances, many of which are commonly encountered in daily life. The bread we eat at dinner and the soap suds we use to clean up afterwards both can be classified as foams. In the broadest sense, foams consist of a dispersed phase of gas (bubbles) enclosed by a continuous phase of either solid or liquid. These materials have complex properties that differ from their component materials. Though air and water are both Newtonian fluids, an aqueous foam has much more complex rheology. The specific properties of foam make it useful in a number of contexts, ranging from food science, to cosmetics, to mining, to fire fighting. A greater understanding of foams can have wide applicability in a

number of fields.

Though foams can take many forms, this thesis will deal exclusively with aqueous foams. These consist of a dispersed phase of gas in a continuous phase of liquid. These two phases are kept apart by the force of surface tension. In order to make water/air foams that are long lived, it is necessary to add molecules called surfactants. These molecules consist of a hydrophilic 'head' attached to a hydrophobic 'tail'. Because of the different preferences of the two ends, these molecules prefer to live at an interface, so that both ends can be satisfied simultaneously. This lowers the surface tension, thus reducing the energy cost of maintaining separate phases in the foam. Additionally, layers of these molecules at the interface create a disjoining pressure that prevents film rupture. In this way, long-lived aqueous foams can be created.

These foams can be characterized by their relative amounts of liquid and gas. So called 'wet' foams, which typically consist of 10% - 20% liquid by volume, have nearly spherical bubbles. In contrast, in 'dry' foams, which generally are those with less than 10% liquid by volume, the bubbles form polyhedra. This thesis will focus primarily on foams in the dry limit. In the limit of perfectly dry foams, requiring force balance can give us information about the structure of the foam. These results are known as Plateau's laws. First, the films will form surfaces of constant mean curvature. Second, all intersections of films consist of threefold junctions with an angle of $2\pi/3$. These intersections are called Plateau borders. Third, Plateau

borders always meet at fourfold nodes with the tetrahedral angle of $\arccos(-1/3)$. These nodes are called vertices.

Aqueous foams are fundamentally non-equilibrium. Even with the addition of surfactant, there is an energy cost associated with keeping the bubbles separate, and this energy is proportional to the surface area of the interface. The lowest energy state is for the gas and liquid phase to be completely separate, and the foam evolves over time to minimize the interface. There are three primary mechanism by which the foam evolves over time: coalescence, drainage, and coarsening. Coalescence occurs when a film ruptures and two bubbles become one. In the presence of gravity, liquid, being denser than gas, is pulled downward, decreasing the liquid fraction of the foam. This process is called drainage. Lastly, there is gas diffusion between bubbles, such that some bubbles grow and others shrink. This process, known as coarsening, increases the average bubble length scale over time through the disappearance of small bubbles. By these mechanisms, the foam lowers its interfacial area and evolves to a lower energy state.

In the foams considered in this thesis, the films are very stable and rupture is never observed. Our foams drain at early times, but at the times that our experiments occur, gravity is balance by capillary forces, and the liquid fraction profile of the foam is constant in time. Therefore, in our experiments our foams are evolving only by coarsening. Foams evolving in this way reach what is know as a 'scaling state'. This is a state where, although the length scale of the foam is

increasing, statistical descriptors of the foam are not changing with time. Regardless of the initial preparation of the foam, all foams reach a scaling state, and they all reach the same scaling state. The foam remains in this state as it evolves through coarsening. There has never been observed, either experimentally or in simulation, any pathological distributions that do not settle to this scaling state.

Coarsening is a complicated process, but it is made more tractable by reducing to two dimensions. In two dimensions Plateau's laws are simpler. In this case the films form arcs of circles, and films meet at threefold vertices at an angle of $2\pi/3$. This means that the bubbles consist of polygons with the sides replaced with circular arcs. Let us now do a simple geometric calculation. We know that the sum of turning angles around the bubble must be equal to $2\pi$. Because the films are arcs of circles, the turning angle around film $i$ is just $l_i/R_i$, where $l$ is the length of the film and $R$ is the radius of curvature of the film. Also, because the films all meet threefold at an angle of $2\pi/3$, we know that the turning angle at each vertex is $\pi/3$. This gives us the following equation for a bubble with $n$ sides:

$$2\pi = \sum_{i=1}^{n} \frac{l_i}{R_i} + n \cdot \frac{\pi}{3} \tag{1.0.1}$$

Next, we note that the diffusion is proportional to the pressure difference across a film times the length of the film. We know from the Laplace-Young pressure law that the pressure is inversely proportional to the radius of curvature, so we know

that

$$\frac{dA}{dt} \propto -\sum_{i=1}^{n} \frac{l_i}{R_i} \tag{1.0.2}$$

Combining these two equations gives the remarkable result

$$\frac{dA}{dt} = K(n-6) \tag{1.0.3}$$

where $K$ is a constant of proportionality. This relationship was first discovered by John von Neumann, and is known as von Neumann's law [67]. This law states that the coarsening rate of an individual bubble depends only on its number of sides. Its area and shape are irrelevant. While von Neumann's law tells us about the coarsening of bubbles, it does not tell us anything about the existence of a scaling state, or the bubble size and shape distributions of such a state.

Von Neumann's law is mathematically exact, but it assumes an ideal dry two dimensional foam. The subject of this thesis is observing how the coarsening behavior of the foam, and the scaling state resulting from this coarsening behavior, change as we violate the assumptions of von Neumann's law.

Von Neumann's law assumes that foams are perfectly dry. In chapters 2 and 3 we make foams that are not perfectly dry. We are able to create a two dimensional foam with tunable liquid content. We observe how this wetness changes the structure and coarsening of the foam, and develop a model to describe the deviation from von Neumann's law. Chapter 2 is adapted from previously published work [77].

Von Neumann's law assumes that foams exist in flat two dimensional space. In chapter 4 we create a two dimensional foam in curved space. We create a cell of constant positive curvature, characterize the structure of this foam, and compare the coarsening to the deviation from von Neumann's law predicted by Avron and Levine [1]. This chapter is adapted from previously published work [76].

Von Neumann's law assumes that foams transfer gas only between their two dimensional neighbors. In chapter 5 we look at the two dimensional surface of a three dimensional foam. Although this foam obeys Plateau's laws in two dimensions, coarsening can occur not only across the visible films, but also across faces in the third dimension. We characterize the structure and coarsening of this foam.

Von Neumann's law assumes that foams are two dimensional. In chapter 6 we develop a method of optical tomography to look inside three dimensional foams. This may be a useful tool to reconstruct the structure of three dimensional foams and observe their coarsening.

Finally, we conclude with a summary and outlook for the future.

# Chapter 2

# Bubble Statistics and Coarsening Dynamics for Quasi-Two Dimensional Foams with Increasing Liquid Content

## 2.1 Introduction

Coarsening is a process in foams where gas diffuses from one bubble to another, so that some bubbles grow and some bubbles shrink [100]. Coarsening also occurs elsewhere, such as for grains in metal alloys, and can often be treated by similar

approaches [29, 82]. Hence foam systems can be studied to understand coarsening behavior more generally. This is simpler to accomplish in two dimensions, where bubble areas are readily measured by conventional digital imaging. For ideal dry foams, which have zero liquid content and obey Plateau's rules, John von Neumann [67] famously showed that the coarsening rate of a given bubble is exactly

$$\frac{\mathrm{d}A_i}{dt} = K_0(n_i - 6), \tag{2.1.1}$$

where $A_i$ and $n_i$ are respectively the area and number of sides of bubble $i$ (see Section 2.4.2 for a generalized derivation). The constant of proportionality, $K_0$, is proportional to the film tension, the solubility and diffusivity of the gas in the liquid, and inversely proportional to the film thickness. It is remarkable that neither the size nor shape of a bubble matters, only its number of sides.

There have been numerous experiments with dry two-dimensional foams to measure coarsening rates and other properties, such as area and side number distribution functions. This includes direct measurements on dry soap froths [27, 28, 84, 81, 83, 39], soap froths with different boundary conditions [45, 75, 74], and measurements on lipid monolayers [87, 3]. Simulations have also been performed [43, 26, 34, 80, 66, 78]. This body of work shows good general agreement with von Neumann's law.

While von Neumann's law describes the rate of change of area for individual bubbles in dry two-dimensional foam, it also bears on how the average bubble area,

$\langle A \rangle = \sum_i A_i / N_{total} = A_{total}/N_{total}$, changes with time. Following the argument of Ref. [82], first note that the average square bubble area, $\langle A^2 \rangle = \sum_i {A_i}^2 / N_{total}$, depends on the width of the area distribution and hence would seem to depend on foam production method and coarsening history. But in fact coarsening foams tend to evolve into a self-similar growth regime, where distribution shapes are stationary and do not depend on time except for an overall scale factor. Once this scaling regime is reached, the quantity $\langle A \rangle^2 / \langle A^2 \rangle$ is constant. Therefore the identity

$$\frac{\langle A^2 \rangle}{\langle A \rangle^2} \langle A \rangle = \frac{1}{A_{total}} \sum_{i=1}^{N_{total}} {A_i}^2 \tag{2.1.2}$$

may be differentiated with respect to time, from $\mathrm{d}\langle A \rangle / \mathrm{d}t$ on the left and from $\mathrm{d}A_i^2/\mathrm{d}t = 2A_i \mathrm{d}A_i/\mathrm{d}t = 2A_i K_0 (n_i - 6)$ on the right. The result can be rearranged and expressed as follows,

$$\frac{d\langle A \rangle}{dt} = 2K_0 \frac{\langle A \rangle^2}{\langle A^2 \rangle} \sum_n F(n)(n-6), \tag{2.1.3}$$

$$= 2K_0 \frac{\langle A \rangle^2}{\langle A^2 \rangle} [\langle \langle n \rangle \rangle - 6], \tag{2.1.4}$$

by introducing a new quantity, the area-weighted side-number distribution

$$F(n) = \sum_{i \ s.t. \ n_i = n} A_i / A_{total}. \tag{2.1.5}$$

By this definition $F(n)$ represents the probability that a randomly chosen point in space lies inside an $n$-sided bubble, which is distinct from the widely-studied

probability $p(n)$ that a randomly chosen bubble is $n$-sided. In the scaling regime, according to Eq. (2.1.4), the rate of change of average bubble area depends on the shape of the area distribution via $\langle A\rangle^2/\langle A^2\rangle$ and the area-weighted average number of sides per bubble, defined in Eq. (2.1.4) by $\langle\langle n\rangle\rangle = \sum_n nF(n)$. The distribution $F(n)$, and in particular the difference of $\langle\langle n\rangle\rangle$ from 6, thus play an important role in the evolution of the foam. However, we are unaware of previous experimental or theoretical investigation of area-weighted statistical quantities, by contrast with numerous studies of $p(n)$.

Coarsening in three dimensional foams has also been extensively studied, and the generalization of von Neumann's law is now known [54]. In terms of experiment, most studies of coarsening in three dimensions have been on wet foams. Various techniques include multiple light scattering [15, 16, 17, 38], magnetic resonance imaging [32], optical tomography [63], x-ray tomography [47, 49], and observation of surface bubbles [25, 35, 93, 24, 18]. However it is much easier to work experimentally with two dimensional foams, where individual bubbles are readily imaged.

One aspect of coarsening that has not been fully elucidated is the effect of non-zero liquid fraction, $\varepsilon$. Experiments on this effect have primarily focused on coarsening rates of three dimensional foams. One study suggested a mechanism for the reduced coarsening rate of three dimensional wet foams as the reduced film area due to liquid in the Plateau borders covering regions of the films and measured under forced drainage that the coarsening rate was reduced by a factor of $(1 - \sqrt{\varepsilon/0.36})$

[38]. Another study measured coarsening rates for a freely draining three dimensional foam and using this model of Plateau border blocking film area measured that the coarsening rate was reduced by a factor of $(1 - \sqrt{\varepsilon/0.44})^2$ [35]. Other studies on coarsening in three dimensional wet foams have found empirically that the coarsening rate is reduced by a factor of $1/\sqrt{\varepsilon}$ [93, 18]. In two dimensions, there has been theoretical [4, 99, 89, 57] and simulation [4, 5] work on the effects of liquid fraction on coarsening. And while this chapter was in preparation, a new theoretical approach was proposed, and tested by Potts model simulations, based on an effective number of sides that depends on the fraction of the perimeter occupied by wet versus dry interfaces [23]. Ref. [58] describes coarsening experiments on bubbles in a microfluidic geometry, where there is a non-zero liquid content that affects the growth rate of average bubble area and that is modeled by an average effective film permeability. Despite all this activity, we are unaware of any work that systematically measures or models the bubble-level topology-dependent effects of liquid content on coarsening.

To make progress on these issues, we present a series of experiments in which the liquid content is systematically varied and the size, shape, and topology of individual bubbles are measured as a function of time. We begin with a description of the foaming system, the sample cell, and the imaging techniques. After demonstrating the success of these methods, we report on bubble statistics, which turn out all to be independent of both time and liquid content. Then we consider the coarsening rate, how it varies with liquid content, and how it develops a violation of von Neumann's

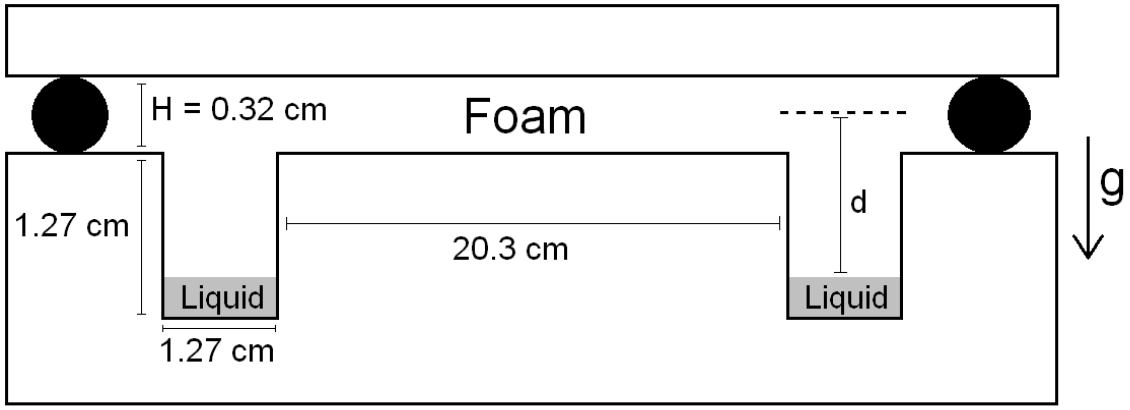


Figure 2.1: A schematic cross section of the circular constant pressure cell; not to scale. Measurements are made in a central $11 \times 11$ cm$^2$ region of interest. The foam wetness is controlled by filling depth of liquid in the trough, in terms of Eq. (2.2.1) and the distance $d$ of the top of the liquid reservoir below the center of the foam. The two solid black circles represent a cross section of the inner O-ring. Not shown: outer O-ring, O-ring grooves, two filling ports, bolt circle between the two O-rings, spacers.

law. Finally we present a model to quantitatively explain this behavior.

## 2.2 Materials and Methods

The liquid foaming solution consists of 75% deionized water, 20% glycerin, and 5% Dawn Ultra Concentrated dish detergent, and has liquid-vapor surface tension $\gamma = 25$ dynes/cm. This creates foams that are stable and long lived; film ruptures were never observed. The sample cell consists of a circular chamber made from clear 1.91 cm thick acrylic plates separated by a $H = 3.2$ mm gap and sealed with two concentric rubber O-rings, the inner of which is 23 cm in diameter. The gap thickness and seal are maintained by a bolt circle and metal spacers, all between the two O-rings. A cross section of the cell is schematically in Fig. 2.1. To create

the foam, the chamber is first completely filled with solution. Pure nitrogen is then pumped into the chamber until only the desired amount of liquid remains. This is accomplished via two valved ports attached on opposite sides of the bottom plate. The chamber is then shaken vigorously until it is completely filled by a uniform opaque foam with sub-millimeter size bubbles, smaller than the gap between the plates. The initial foam is thus three dimensional. Immediately after production it is placed 20 cm away from a Vista Point A lightbox, and 2.5 m from a Nikon D80 camera with a Nikkor AF-S 300 mm 1:2.8 D lens. It is then left undisturbed to coarsen into a two-dimensional foam consisting of a single layer of bubbles with an average size greater than the gap, which typically requires two days. The field of view thus encompasses up to a few hundred bubbles. Under computer control, photographs are then taken at two-minute intervals for durations ranging up to two weeks. From all runs, a total of 14663 bubbles were observed. This is enough for statistical purposes, though it is possible to observe many more bubbles at lower resolution using sample cells that are larger or have thinner gaps [71, 13].

The crucial innovative feature of the sample cell is a circular trough, of width and depth 1.27 cm and inner diameter 20.3 cm, which serves as both a liquid reservoir and a means to control the liquid content of the foam. The initial three-dimensional foam is quite wet, but it drains by gravity and the expelled liquid accumulates in the trough. As the foam becomes drier, the radius of curvature $r$ of the Plateau borders decreases and the Laplace pressure $\gamma/r$ increases. Drainage halts when hydrostatic equilibrium is established by balance of capillary and gravity forces. For this, the

Laplace pressure must equal the gravitational pressure $\rho g d$, where $\rho = 1.07$ g/cc is the liquid solution density, $g = 980$ cm/s$^2$, and $d$ is the distance of the Plateau borders above the liquid in the reservoir, as depicted in Fig. 2.1. Accordingly, the radius of curvature of the Plateau borders is given by

$$r = \frac{\gamma}{\rho g d}, \tag{2.2.1}$$

and hence can be controlled through $d$ by the filling depth of liquid in the reservoir. Here $d$ is measured to $\pm 0.2$ mm and the dimensions of the reservoir trough are large enough that this depth remains constant once the foam becomes two dimensional. Thus the coarsening of interest proceeds at constant, controllable, $r$. A further advantage of the trough is that the relatively large volume of liquid solution permits easy foam production by shaking.

Example images are shown in Fig. 2.2 for foams with three different filling depths, $d$, which decrease from left to right. It can be seen that as $d$ decreases, the Plateau borders become noticeably thicker as expected by Eq. (2.2.1). While the foams appear to be dry and two-dimensional, their actual three-dimensional structure is emphasized underneath the main images by schematic drawings of a vertical cut across each foam. There, the Plateau borders running along the top and bottom plates appear as scalloped triangular regions, and the soap films running between plates appear as vertical lines connecting top and bottom Plateau borders. Bubble area is thus appropriately measured by the skeletonization procedure as the area

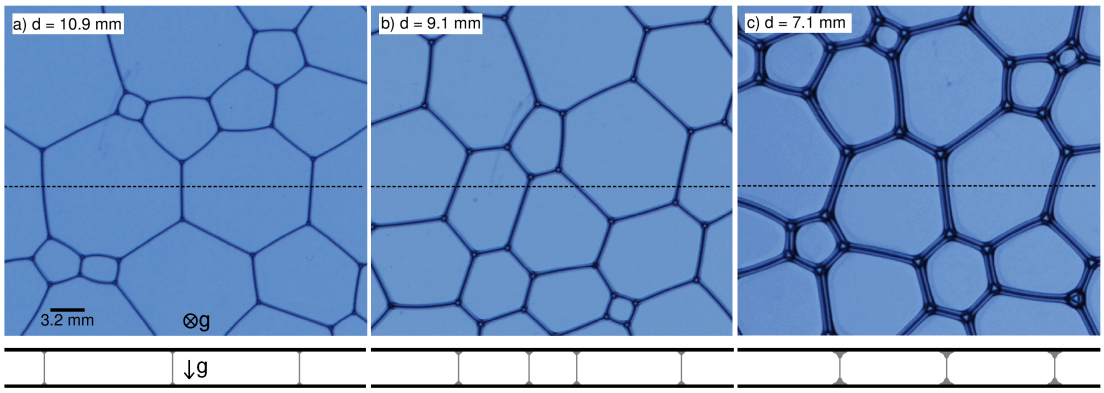


Figure 2.2: Images of a subregion of three foams, with different liquid filling depths $d$ as labelled. For smaller $d$, the Plateau border radius $r$ increases according to Eq. (2.2.1). This is evident in the main images and is shown underneath by schematic drawings of surface Plateau borders and soap films in a vertical cross-section along the dotted lines in the middle of the main images. The scale for all images and schematics is indicated by the bar in (a), which equals the gap $H$ between top and bottom plates and hence the height of the vertical soap films. In (c) note that there are bright spots at the 'vertices' where three surface Plateau borders are seen to meet. This feature arises from light channeled up through the thick vertical Plateau borders that span the gap between the upper and lower plates of the sample cell. Note that these are well separated; therefore, there is no ambiguity in determining the number $n$ of sides of a bubble, even in the wettest foams measured here.

enclosed by the vertical soap films, not as the "free area" seen by eye to be enclosed by thick Plateau borders. Note that variation of $d$ affects only the Plateau borders, not the film thicknesses. Since the Plateau borders are macroscopic, while the film thickness is of order 100 nm, the liquid content of the foam is set entirely by the Plateau border thickness. The volumetric liquid fraction scales as $r^2R/(R^2H) \propto 1/(d^2R)$ where $R$ is the typical bubble radius and $H$ is the gap between the plates. The projected-area liquid fraction scales as $rR/(R^2) \propto 1/(dR)$. Neither of these liquid fractions remains constant as the foam coarsens; rather, more importantly, the Plateau border radii and Laplace pressures remain constant as set by the distance $d$ of the foam above the top of the liquid reservoir. Throughout, we thus refer to $d$ as controlling the liquid *content*, not the liquid fraction.

| $d$ (mm) | $N_{initial}$ | $N_{final}$ |
|---|---|---|
| 11.3 | 114 | 41 |
| 10.9 | 73 | 18 |
| 9.4 | 144 | 44 |
| 9.1 | 298 | 143 |
| 8.5 | 104 | 82 |
| 8.0 | 384 | 49 |
| 7.1 | 290 | 158 |
| 6.7 | 217 | 85 |
| 6.2 | 252 | 100 |

Table 2.1: Initial and final numbers of bubbles in an $11 \times 11$ cm$^2$ square region of interest in the center of the cell for different liquid filling depths. The quantity $d$ is the distance of the foam above the liquid reservoir. The uncertainty in $d$ is 0.2 mm. Only bubbles completely within the region of interest are considered.

Digital images such as shown in Fig. 2.2 are collected for foams with a wide range of different filling depths, as listed in Table 2.1 along with the number of bubbles entirely in the central $11 \times 11$ cm$^2$ region of interest at the beginning and end of the collection period. Using standard procedures, it is relatively straightforward to threshold and skeletonize each image and then measure the area and number of sides of each bubble that lies entirely within the region of interest. However, when a small bubble shrinks toward zero its diameter inevitably becomes smaller than the distance between the plates. Then it may 'pinch in' and form a film horizontally in the middle of the bubble, and thus no longer be two-dimensional. Such bubbles and their neighbors, are excluded from the analysis.

Example results for area versus time are displayed in Fig. 2.3 for individually selected bubbles with different side numbers $n$, for the same three foams depicted above with different liquid filling depths. Note that the areas are constant for $n = 0$, and either increase or decrease linearly with time for $n > 6$ or $n < 6$, respectively.

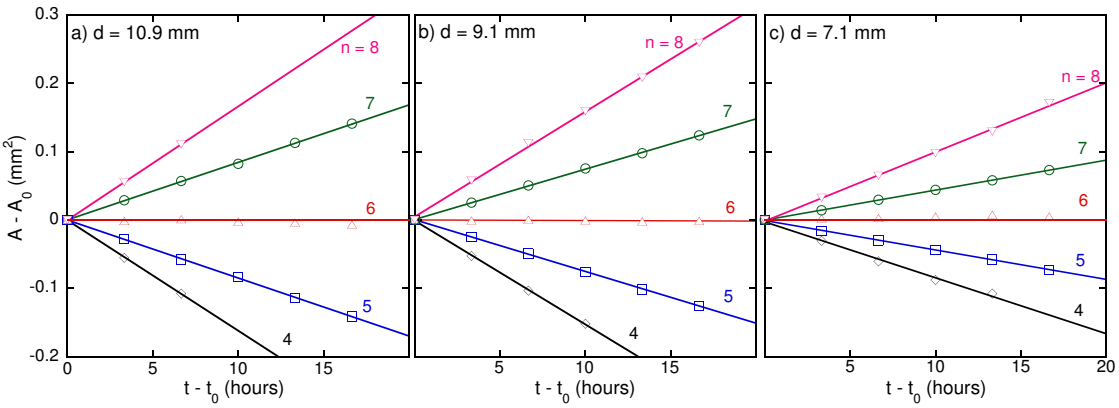


Figure 2.3: Area versus time for selected bubbles with different number $n$ of sides, for three different distances $d$ of the foam above the reservoir, as labelled. The liquid content increases with decreasing $d$, as illustrated in Fig. 2.2. Note that the area change is linear in time and at rate proportional to $(n-6)$. The lines are fits to the von Neumann form, $A - A_0 = K(n-6)t$, with the same $K$ value for all $n$: (a) $K = 0.84 \pm 0.06$ mm$^2$/hr, (b) $K = 0.72 \pm 0.06$ mm$^2$/hr, (c) $K = 0.42 \pm 0.02$ mm$^2$/hr, Increasing the liquid content decreases the rate of change of area, such that wetter foams coarsen more slowly; compare to Fig. 2.14.

Fits are found to the von Neumann prediction, $A(t) = A_0 + K(n-6)$, where $A_0$ is the area at an initial time and a single value of $K$ is adjusted to simultaneously fit all the data in each panel of the figure. While these fits are excellent, the feature of main interest in Fig. 2.3 is that *the coarsening rate decreases with increasing liquid content*, as $d$ decreases from left to right. Indeed the slopes for a given $n$ are equal to $K(n-6)$ and are seen to decrease by a factor of two from (a) to (c). Intuitively, the thicker the Plateau border, the smaller the film area through which gas diffuses, and hence the slower the coarsening. This serves as proof-of-principle: Our custom sample cell design and procedures thus succeed in producing dry two-dimensional foams with controllable Plateau border thicknesses.

As a technical aside, throughout the remainder of this chapter the rate $\mathrm{d}A/\mathrm{d}t$ of a bubble's growth is found by fits of $A(t)$ vs $t$ over a time window over which

the side number $n$ remains constant. And there is no ambiguity in the value of $n$, even for the wettest foams at smallest $d$ values where $r$ becomes as large as $H/4$, since the foams have large enough bubbles to appear two-dimensional when viewed from above, as in Fig. 2.2. In other words, the soap films remain vertical and are easily located by the thresholding/skeletonization procedure for any wetness. Even in the wet foam limit, where horizontal top and bottom Plateau borders merge, the vertical Plateau borders are still well-separated and hence $n$ is well-defined. The only difficulty is for very small three-sided bubbles, which can detach from the top or bottom plate and hence become three-dimensional. Since three-sided bubbles tend to start small and shrink rapidly, they do not remain two-dimensional for very long. Due to this effect, we were able to measure growth rates for only eight of the 195 three-sided bubbles seen in our combined runs.

To further characterize our liquid solution, we now measure coarsening in the very dry limit where the border thickness is made as small as possible. For this, we use the same sample cell but orient it vertically rather than horizontally and fill it with liquid to a depth of 7.5 cm above the bottom of the O-ring. As usual, foam is produced by vigorous shaking and then allowing it to drain and coarsen for about one day into a two-dimensional froth. The rate of area change, $\mathrm{d}A/\mathrm{d}t$ of individual bubbles is then measured along with their number of sides and their height $d$ above the drained liquid. Since the cell is vertical, the value of $d$ can be up to 6 cm, which is much greater than can be attained in the horizontal orientation due to the fixed 1.27 cm depth of the trough. By Eq. (2.2.1), this gives the smallest Plateau border

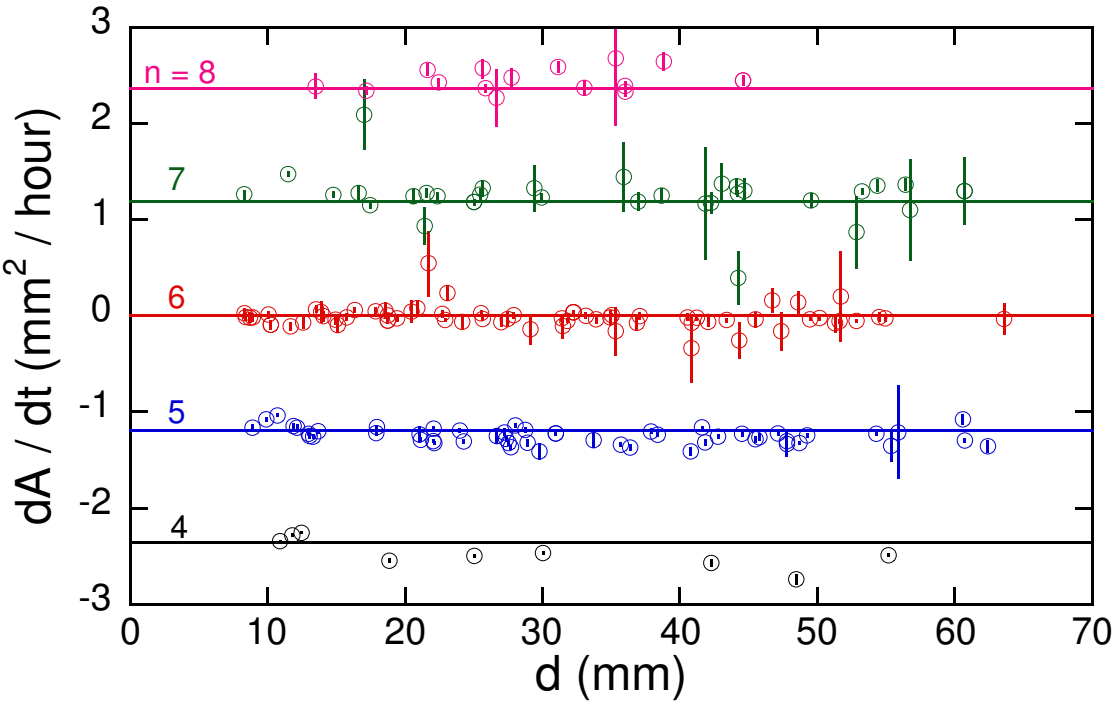


Figure 2.4: Rates of area change for bubbles in a vertical cell vs height $d$ of bubbles above the liquid surface. The cell is the same shown in Fig. 2.1, but re-oriented and filled 7.5 cm from the bottom of the O-ring. Symbol types distinguish bubbles with different number $n$ of sides, as labeled. The lines represent $\mathrm{d}A/\mathrm{d}t = K_0(n-6)$ (Eq. (4.1.1)) with $K_0 = 1.20 \pm 0.06$ mm$^2$/hr . Since the growth rates are independent of $d$, the bubbles are in the dry foam limit where the Plateau border size is negligible compared to bubble size.

radius as 0.005 cm. The resulting coarsening rates are plotted vs $d$ in Fig. 2.4, with each point representing one bubble with side numbers indicated by symbol color and label. Note that $\mathrm{d}A/\mathrm{d}t$ depends on side number but has no apparent dependence on $d$ across the entire range of 1 cm $< d <$ 6 cm. These data are therefore all in the dry foam limit. Furthermore, absence of dependence on $d$ indicates that the film thickness is constant. In principle the thickness must decrease with height due to gravity, but apparently a balancing disjoining pressure can be achieved by very slight thinning away from the minimum in the effective interface potential. The fit to von Neumann's law, $\mathrm{d}A/\mathrm{d}t = K_0(n-6)$, is shown by the solid horizontal lines, and gives $K_0 = 1.20 \pm 0.06$ mm$^2$/hr. This value reflects the physical chemistry of the gas/surfactant-solution/soap-film system, independent of the geometry of the bubbles and the Plateau borders.

This completes the description of materials and methods, and the characterization of the foaming system. In the next sections we now turn to the main tasks of measuring bubble statistics and coarsening rates as a systematic function of liquid content.

## 2.3 Bubble Statistics

In the follow three subsections we present the statistical distributions for the topology, size, and shapes of bubbles.

### 2.3.1 Topology

| $n$ | $N$ | $p(n)$ | $F(n)$ | $m(n)$ |
|---|---|---|---|---|
| 3 | 195 | $0.013 \pm 0.001$ | $0.0009 \pm 0.00006$ | $7.69 \pm 0.05$ |
| 4 | 1217 | $0.083 \pm 0.002$ | $0.034 \pm 0.006$ | $7.04 \pm 0.02$ |
| 5 | 4462 | $0.304 \pm 0.005$ | $0.173 \pm 0.007$ | $6.5 \pm 0.007$ |
| 6 | 4634 | $0.316 \pm 0.005$ | $0.326 \pm 0.009$ | $6.22 \pm 0.006$ |
| 7 | 2611 | $0.178 \pm 0.003$ | $0.259 \pm 0.007$ | $6.06 \pm 0.007$ |
| 8 | 1120 | $0.076 \pm 0.002$ | $0.141 \pm 0.006$ | $5.92 \pm 0.01$ |
| 9 | 327 | $0.022 \pm 0.001$ | $0.049 \pm 0.004$ | $5.82 \pm 0.02$ |
| 10 | 89 | $0.006 \pm 0.0006$ | $0.016 \pm 0.002$ | $5.73 \pm 0.03$ |
| 11 | 8 | $0.0005 \pm 0.0002$ | $0.001 \pm 0.0005$ | $5.91 \pm 0.16$ |

Table 2.2: Topological distributions averaged over all times and liquid contents, and their uncertainties. Here $n$ is the number of sides; $N$ is the total number of bubbles observed with $n$ sides; $p(n)$ is the fraction of bubbles having $n$ sides, and the uncertainty is the value divided by $\sqrt{N}$; $F(n)$ is the fraction of area occupied by $n$ sided bubbles, and the uncertainty is the standard deviation divided by the square root of the number of photographs; and $m(n)$ is the average number of sides of the neighbors of an $n$ sided bubble, and the uncertainty is the standard deviation divided by $\sqrt{N}$. The total number of bubbles observed is $\sum N = 14663$.

The number of sides of a bubble is a key topological quantity, not just for describing the bubble but also for determining its coarsening rate according to von Neumann's law. Thus we begin by analyzing image data for the probability $p(n)$ that a randomly-chosen bubble has $n$ sides and also for the probability $F(n)$ that a randomly-chosen point in space is inside an $n$-sided bubble. As discussed in the introduction, $F(n)$ is an area-weighted side number distribution that sets the average coarsening rate in the scaling regime. Example data for these side number distributions are plotted, separately for each $n$, versus time in Fig. 2.5 for a typical foam sample with $d = 9.1$ mm. To within statistical uncertainty, the individual $p(n)$ and $F(n)$ values are seen to be independent of time. This demonstrates that the foam is in a scaling regime, which is not surprising because the production method gave very small bubbles that coarsened greatly before data collection commenced. This

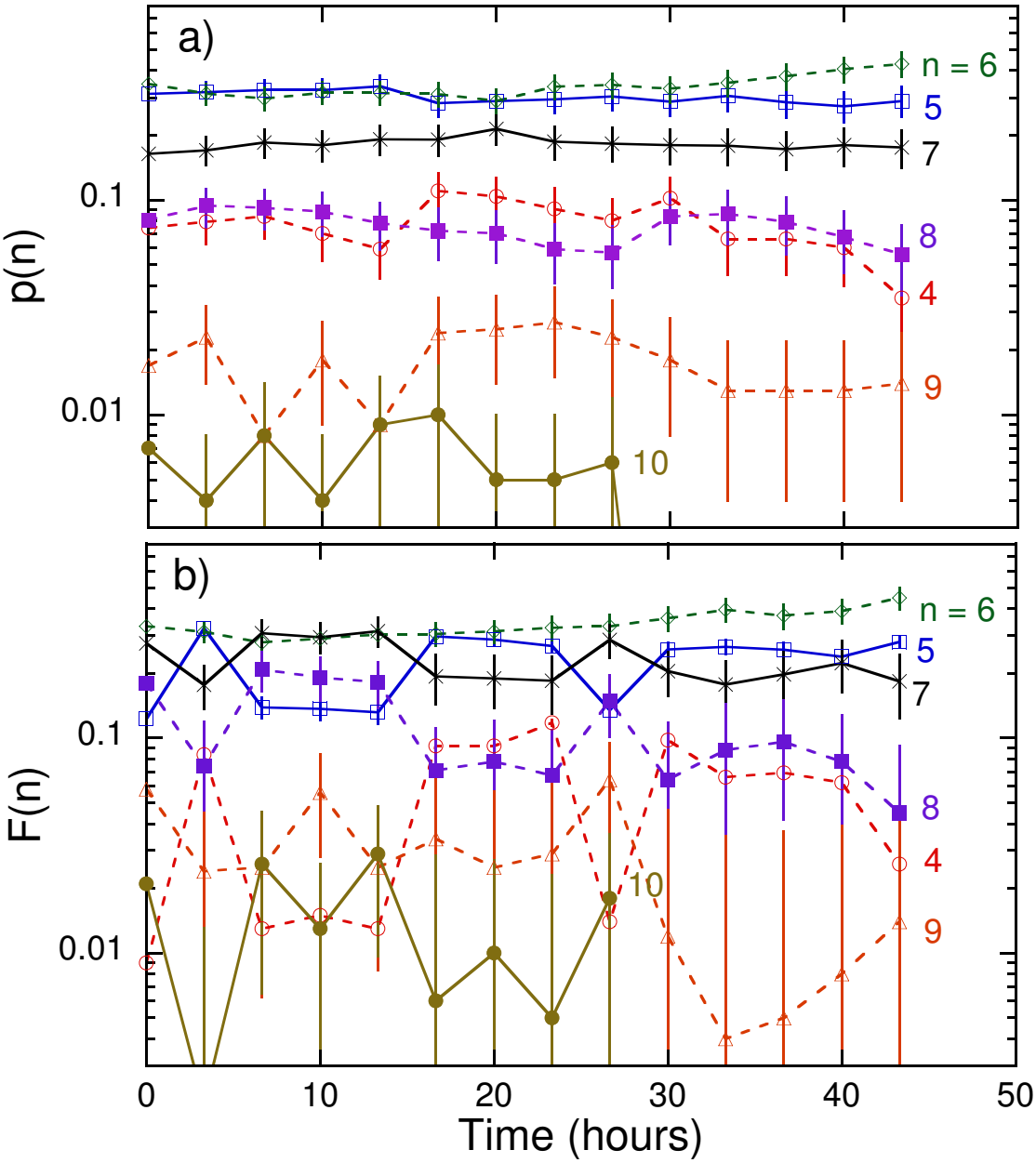


Figure 2.5: (a) Side number distribution, and (b) area-weighted side number distribution, versus time for a typical foam sample with $d = 9.1$ mm.

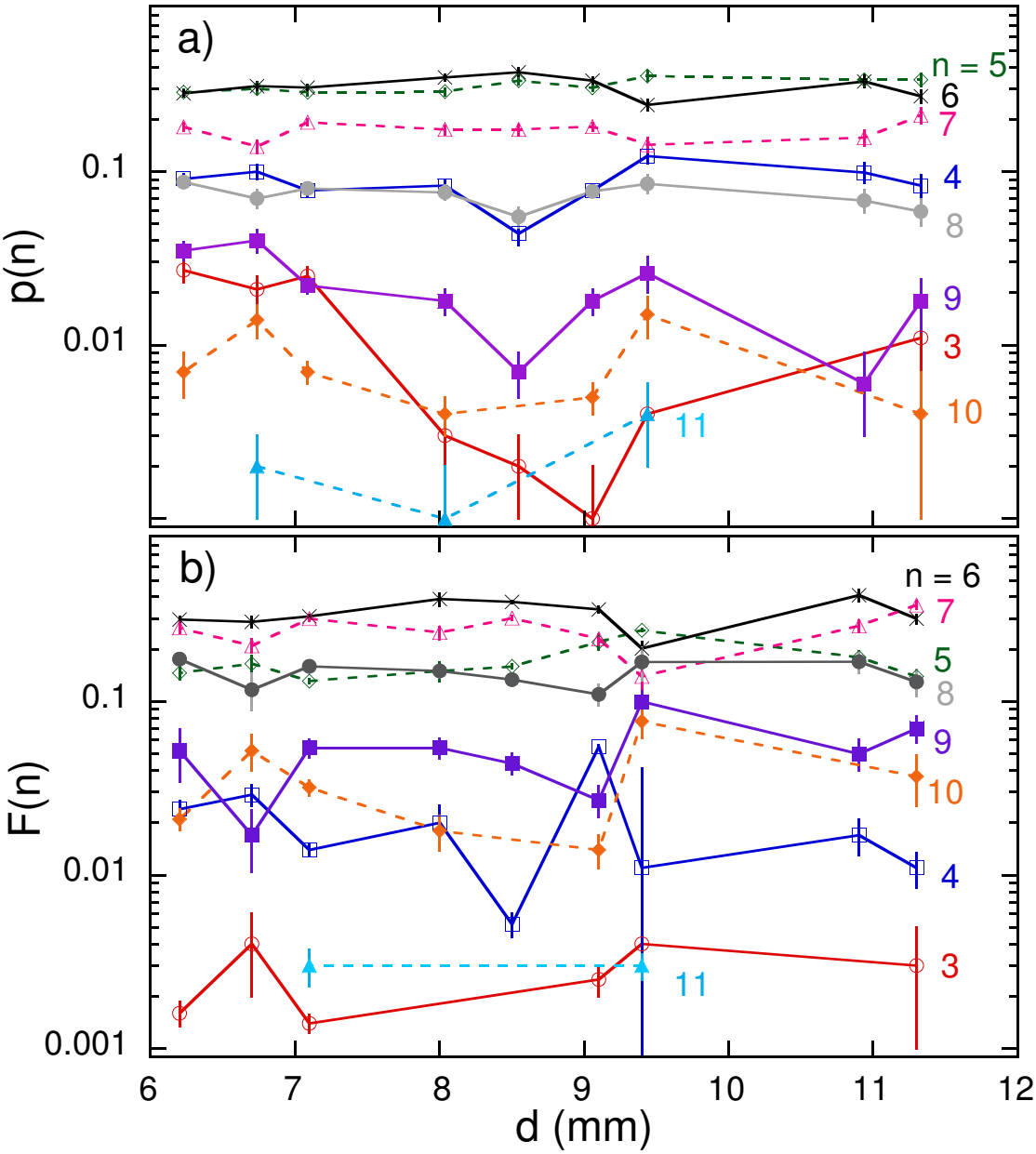


Figure 2.6: Time averages of (a) side number distribution, and (b) area-weighted side number distribution, versus height $d$ of the foam above the liquid reservoir.

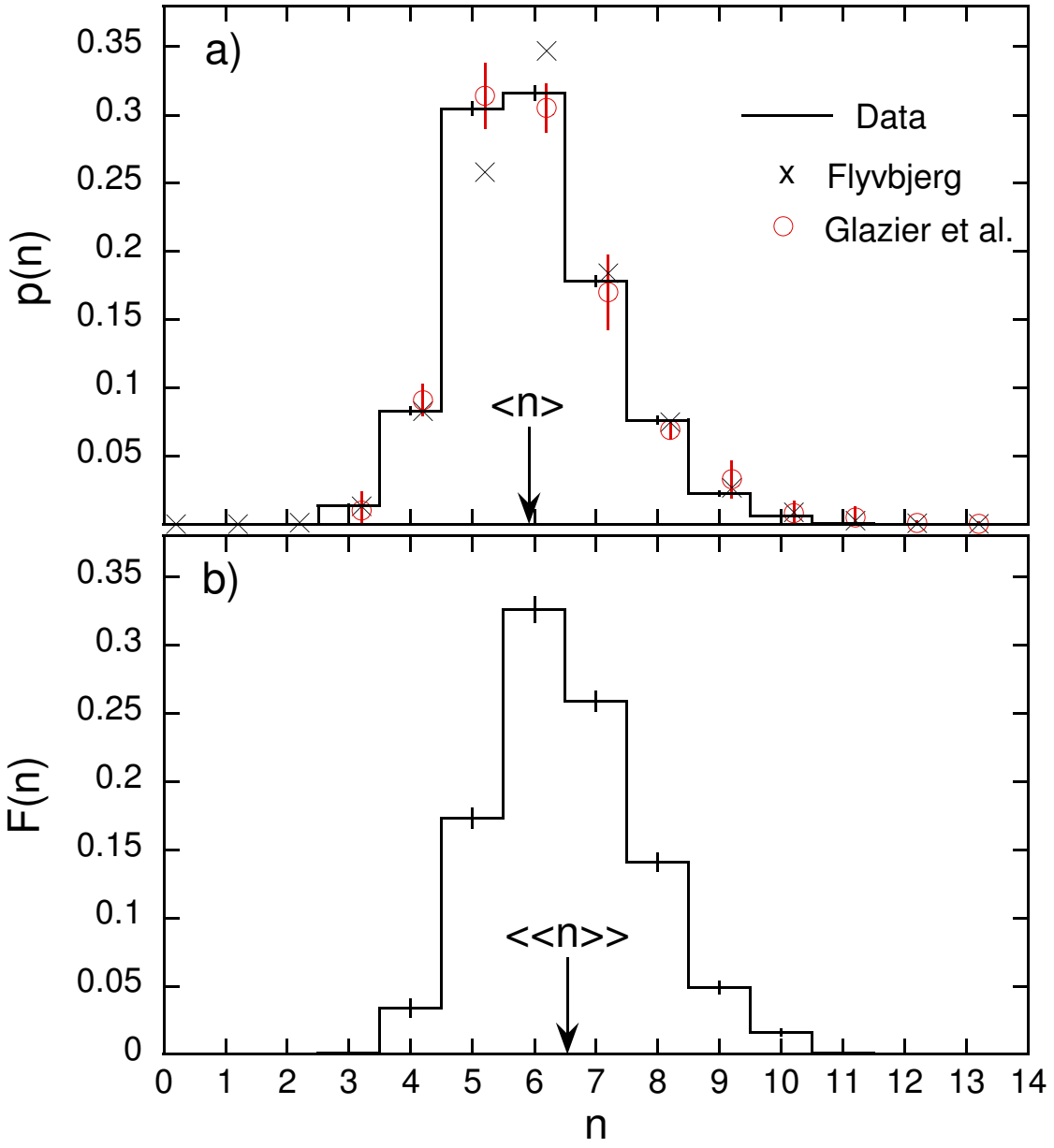


Figure 2.7: (a) Side number distribution, and (b) area-weighted side number distribution, averaged over all times and over all liquid contents. The average number of sides, and the area-weighted number of sides, are indicated by arrows as labeled. For comparison with $p(n)$, data from Ref. [26] are shown by open circles and the predictions from Ref. [21] are shown by crosses. The plotted distribution data are listed in Table 2.2.

holds for the other foams with different liquid content, too, and therefore we may compute the time-averages of the side distributions. The results for $p(n)$ and $F(n)$ are shown in Fig. 2.6 versus the height $d$ of the foam above the liquid reservoir. Now we see that, to within statistical uncertainty, there is no systematic dependence on liquid content. This is consistent with the validity of the decoration theorem, as expected since vertical Plateau borders do not merge [4].

Since the side distribution $p(n)$ and the area-weighted side distribution $F(n)$ do not vary with time or liquid content, we therefore average together all the data and plot the final results versus $n$ in Fig. 2.7. Actual numerical values and uncertainties are given in Table 2.2. Both distributions are peaked at $n = 6$ sides, and have full-width at half-maximum of about three. Out of 14663 total bubbles, we never observed any with fewer than $n = 3$ sides or with more than $n = 11$ sides. The detailed shape of $p(n)$ is consistent with prior observations [82, 83, 29, 26], as shown by comparison with the data from Ref. [26] and the theoretical prediction from Ref. [21]. The shape of $F(n)$ is skewed from $p(n)$ toward higher $n$, which is expected because bubbles with larger $n$ tend to have greater area (as discussed in detail in the next sub-section). To our knowledge, there is no prior data or theory with which to compare our $F(n)$ data.

Definitions and values of various moments of the scaling regime distributions $p(n)$ and $F(n)$ are listed in Table 2.3. The average side number is $\langle n \rangle = 5.92 \pm 0.01$, which is slightly less than the value of 6 required by topological reasons for

| Quantity | Definition | Value |
|---|---|---|
| $\langle n \rangle$ | $\sum np(n)$ | $5.92 \pm 0.01$ |
| $\mu_2$ | $\sum [n - \langle n \rangle]^2 p(n)$ | $1.56 \pm 0.02$ |
| $\langle\langle n \rangle\rangle$ | $\sum nF(n)$ | $6.53 \pm 0.08$ |
| $\nu_2$ | $\sum [n - \langle\langle n \rangle\rangle]^2 F(n)$ | $1.67 \pm 0.09$ |
| $\langle A^2 \rangle / \langle A \rangle^2$ | $[\sum A_i^2/N_{tot}]/[\sum A_i/N_{tot}]^2$ | $1.72 \pm 0.25$ |
| $\langle P^2 \rangle / \langle P \rangle^2$ | $[\sum P_i^2/N_{tot}]/[\sum P_i/N_{tot}]^2$ | $1.20 \pm 0.06$ |

Table 2.3: Measured values of several statistical quantities, averaged over all times and liquid contents, and their uncertainties. Here $n$ is the number of sides of a bubble; $p(n)$ is the fraction of bubbles with $n$ sides; $F(n)$ is the fraction of area occupied by $n$ sided bubbles; $A$ is bubble area; $P$ is bubble perimeter; and $N_{tot}$ is the total number of bubbles.

an infinite system. The area-weighted average side number is somewhat greater, $\langle\langle n \rangle\rangle = 6.53 \pm 0.08$. This result is important because, from Eq. (2.1.4), the expected average coarsening rate in the scaling regime is proportional to $[\langle\langle n \rangle\rangle - 6]$. The variance of $p(n)$ is $\mu_2 = 1.56 \pm 0.02$, consistent with prior scaling-state measurements [84]. This quantity is often used as a measure of disorder. The variance of $F(n)$ is slightly larger, $\nu_2 = 1.67 \pm 0.09$.

The final purely topological quantity we consider is the average number $m$ of sides of the neighbors of an $n$-sided bubble. As done for the side distributions, we first verify that $m(n)$ data are independent of time and liquid content and hence may be averaged together. The final results are displayed in Fig. 4.7. For comparison, we obtain a satisfactory fit to the empirical Aboav-Weaire form, $m(n) = (6 - a) + (6a + \mu_2)/n$ [100], where $\mu_2 = 1.56$ is the measured variance and the one fitting parameter is found to be $a = 1.1 \pm 0.1$. Similar values of $a$ have been found for many cellular patterns [100], including two-dimensional foams.

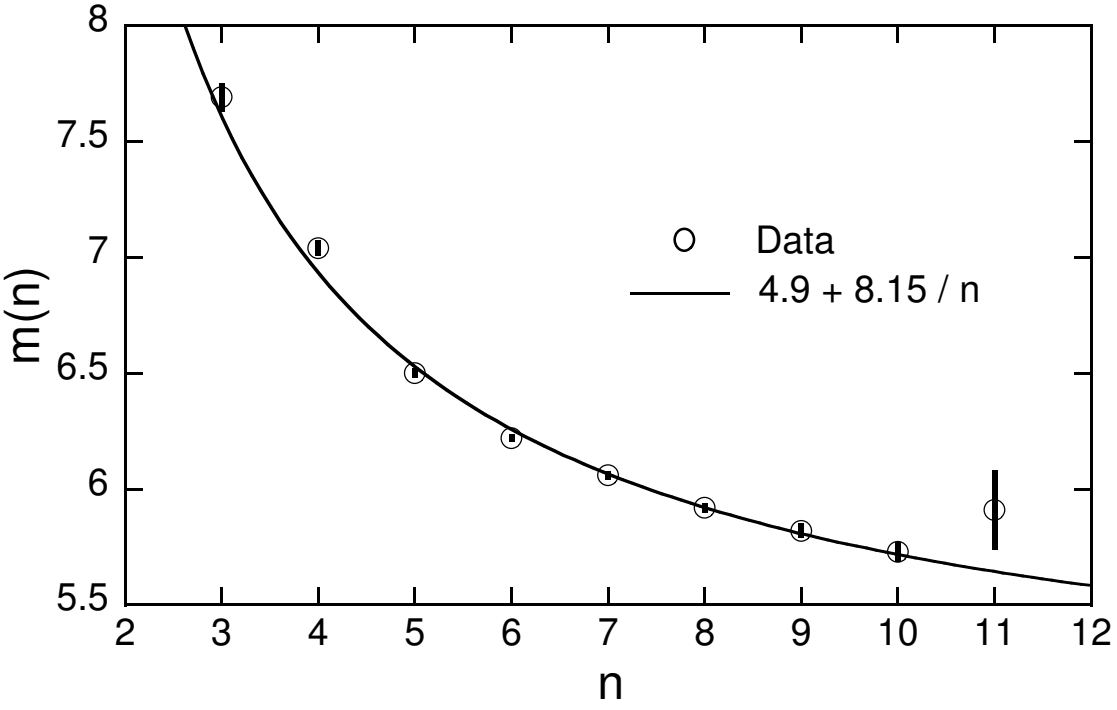


Figure 2.8: The average number $m(n)$ of sides of the neighbors of $n$-sided bubbles. The results here are an average over all times and over all liquid contents. The black line is the empirical Aboav-Weaire law, $m(n) = (6 - a) + (6a + \mu_2)/n$, where $\mu_2$ is the measure the variance and $a$ is the only fitting parameter, which is found to be $a = 1.1 \pm 0.1$. The plotted $m(n)$ values are listed in Table 2.2.

### 2.3.2 Size

In this subsection we consider distributions of bubble sizes, beginning with area since this is the quantity that appears in von Neumann's law. As a prelude we verify that the distributions are independent of both liquid content and time, when the average is scaled out. This reinforces the above conclusion that the foam is in a scaling regime, and allows us to combine the time-averaged scaled distributions for each foam sample into a single curve. The results for one minus the cumulative area distribution are plotted on semi-logarithmic axes in Figs. 2.9a. Error bars are given by the range of values for different liquid contents, divided by the square root of the number of different liquid contents measured. The data exhibit a slight but nonzero downward curvature, and hence are not quite exponential. This is consistent with prior work [21, 82, 83, 29, 26]. A good fit is found to a compressed exponential, given along with the corresponding probability distribution function as

$$\text{CDF} = 1 - e^{-\left[\Gamma\left(1+\frac{1}{\alpha}\right)\frac{A}{\langle A\rangle}\right]^{\alpha}} \tag{2.3.1}$$

$$\text{PDF} = \alpha\Gamma\left(1+\frac{1}{\alpha}\right)^{\alpha}\left(\frac{A}{\langle A\rangle}\right)^{\alpha-1} e^{-\left[\Gamma\left(1+\frac{1}{\alpha}\right)\frac{A}{\langle A\rangle}\right]^{\alpha}} \tag{2.3.2}$$

with fitting parameter $\alpha = 1.21 \pm 0.05$; this, and a simple exponential (case $a = 1$), are both shown in Fig. 2.9.

Recall from Eq. (2.1.4) that the value of $\langle A\rangle^2/\langle A^2\rangle$ helps set the rate of change of the average bubble area in the scaling regime. Averaging over all times and

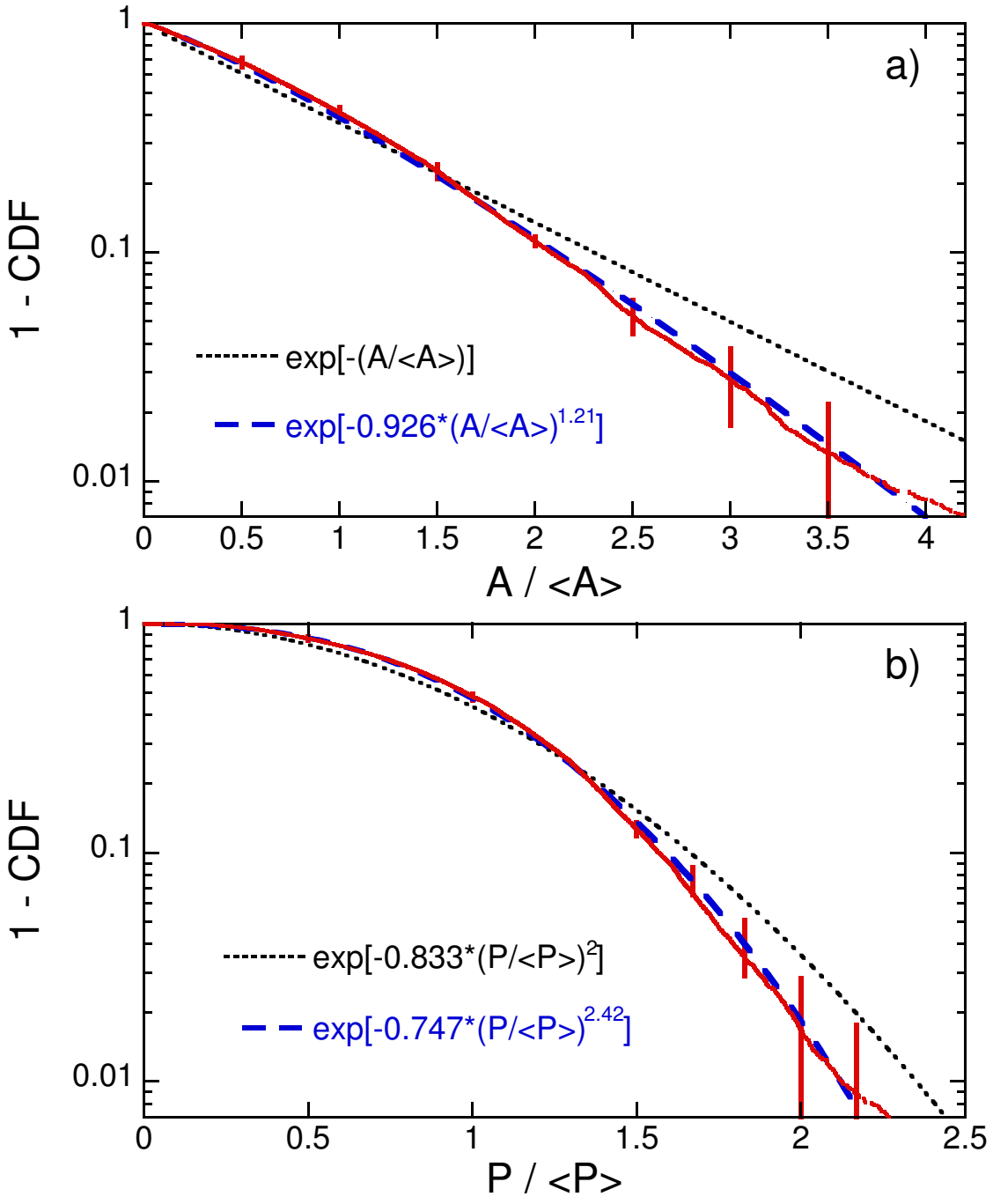


Figure 2.9: Cumulative distribution function data for (a) bubble area $A$ and (b) bubble perimeter $P$, averaged over all times and liquid contents. The error bars represent the uncertainty in the mean, as estimated from the range in values for different liquid contents. In (a) the black dotted line represents an exponential area distribution and the blue dashed curve represents a compressed exponential. The corresponding forms for the cumulative perimeter distributions are shown in (b) using the same line codes, further assuming $A \propto P^2$ with the same proportionality constant for all bubbles.

liquid fractions we find $\langle A\rangle^2/\langle A^2\rangle = 0.58 \pm 0.09$, which is close to the value of 1/2 for a perfectly exponential distribution. Combining this with the result $\langle\langle n\rangle\rangle = 6.53 \pm 0.08$, Eq. (2.1.4) thus gives the average rate of coarsening for a 2d foam in the self-similar scaling regime as $\mathrm{d}\langle A\rangle/\mathrm{d}t = (0.61 \pm 0.13)K$ where $K$ is the constant in von Neumann's law for individual bubbles, $\mathrm{d}A/\mathrm{d}t = K(n-6)$. For the vertical cell, the value of $K_0$ then gives the expectation $\mathrm{d}\langle A\rangle/\mathrm{d}t = (0.74 \pm 0.15)$ mm$^2$/hr, which is consistent with the direct measurement of $\mathrm{d}\langle A\rangle/\mathrm{d}t = (0.83 \pm 0.03)$ mm$^2$/hr.

Since bubbles are not all identical in shape, bubble size is not uniquely specified by area. So next we consider bubble perimeter, which is also important since in two-dimensions coarsening is ultimately driven by a reduction of the total sum of bubble perimeters. The cumulative distribution for perimeter, averaged over all times and liquid contents, is plotted in Fig. 2.9b. For comparison, we also plot the expectation corresponding to the fitted cumulative area distribution. For this we must make the further assumption that bubble shape is constant, which implies $A = cP^2$ and $\langle A\rangle = c\langle P^2\rangle$ where $c$ is some constant. Thus the trial perimeter cumulative distribution function is given by Eq. (2.3.1) with $A/\langle A\rangle$ replaced by $P^2/\langle P^2\rangle = [\langle P\rangle^2/\langle P^2\rangle][P/\langle P\rangle]^2$. From the list of bubble perimeters, we directly compute the second moment to be $\langle P^2\rangle/\langle P\rangle^2 = 1.20 \pm 0.06$. The resulting compressed exponential cumulative perimeter distribution is plotted in Fig. 2.9b, and found to agree extremely well with the data. This foreshadows a point to made directly in a later section: the average bubble shape is remarkably constant.

### 2.3.3 Size-topology

| $n$ | $N$ | $\langle A_n\rangle/\langle A\rangle \pm \sigma \pm \sigma/\sqrt{N}$ | $\langle P_n\rangle/\langle P\rangle$ | $E(n)$ | $C(n)$ |
|---|---|---|---|---|---|
| 3 | 195 | $0.32 \pm 0.59 \pm 0.04$ | $0.46 \pm 0.42 \pm 0.03$ | 1.065±0.02±0.001 | $0.19 \pm 0.13 \pm 0.01$ |
| 4 | 1217 | $0.62 \pm 0.84 \pm 0.02$ | $0.73 \pm 0.46 \pm 0.01$ | 1.071±0.02±0.002 | 0.299±0.14±0.004 |
| 5 | 4462 | $0.72 \pm 0.70 \pm 0.01$ | 0.843±0.38±0.006 | 1.070±0.03±0.001 | 0.137±0.10±0.002 |
| 6 | 4634 | $1.01 \pm 0.66 \pm 0.01$ | 1.037±0.35±0.005 | 1.069±0.03±0.001 | $-0.042 \pm 0.18 \pm 0.003$ |
| 7 | 2611 | $1.32 \pm 0.77 \pm 0.02$ | 1.183±0.40±0.008 | 1.070±0.02±0.001 | $-0.215 \pm 0.28 \pm 0.005$ |
| 8 | 1120 | $1.55 \pm 0.96 \pm 0.03$ | $1.26 \pm 0.47 \pm 0.01$ | 1.070±0.03±0.002 | $-0.409 \pm 0.16 \pm 0.005$ |
| 9 | 327 | $1.95 \pm 1.3 \pm 0.07$ | $1.41 \pm 0.54 \pm 0.03$ | 1.067±0.04±0.002 | −0.59±0.25±0.01 |
| 10 | 89 | $2.9 \pm 2.0 \pm 0.2$ | $1.72 \pm 0.70 \pm 0.08$ | 1.065±0.01±0.001 | −0.73±0.44±0.05 |
| 11 | 8 | $3.2 \pm 3.7 \pm 1.3$ | $1.7 \pm 1.2 \pm 0.4$ | 1.066±0.01±0.005 | $-0.9 \pm 0.37 \pm 0.1$ |

Table 2.4: Shape quantities, averaged over all times and liquid contents, for each side number $n$. The standard deviation of the distribution ($\sigma$) and the uncertainty in the mean ($\sigma/\sqrt{N}$ where $N$ is the number of bubbles) are also given. The first two quantities are the area and perimeter, normalized by the average over the whole sample. The second two quantities are the elongation and circularity, defined by Eqs. (2.3.7-2.3.8).

With topology and size statistics now in hand, we turn to the relationship between these measures. For many cellular systems, a linear correlation has been observed between either area or perimeter and side number [8]:

$$\langle A_n\rangle/\langle A\rangle = 1 + \lambda(n-6), \quad \text{(Lewis)} \tag{2.3.3}$$

$$\langle P_n\rangle/\langle P\rangle = 1 + \nu(n-6), \quad \text{(Desch)} \tag{2.3.4}$$

where $\lambda$ and $\nu$ are parameters characteristic to a particular system. The first of these empirical laws was found by Lewis for epithelial cucumber cells, and is known as Lewis' law [51, 52]. If $\langle A_n\rangle/\langle A\rangle$ is linear in $n$, then it must have this form, but to prove linearity requires additional constraints [73]. The analogous relationship for perimeter is called Desch's law or Feltham's law. If the energy area of a cell

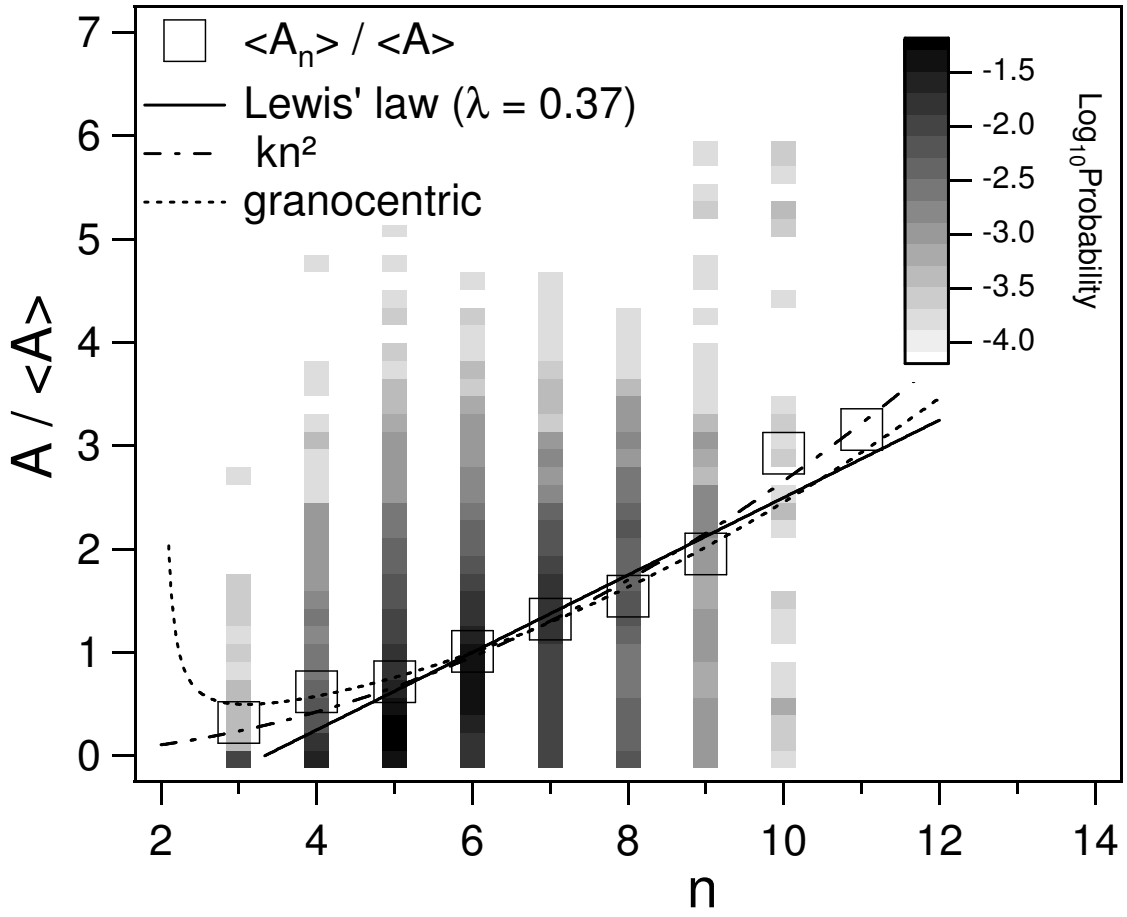


Figure 2.10: Normalized area versus side number for all bubbles; the distribution is given in grayscale and the average is indicated by open squares. Note that the distributions are quite skewed, as expected since the area distribution averaged over all $n$ is nearly exponential. The fit to Lewis' law, Eq. (2.3.3) with fitting value $\lambda = 0.37 \pm 0.03$, is shown by a solid line. The fit to the Ref. [14] form, $kn^2$ with fitting value $k = 0.027$, is shown by the dash-dot curve. The simplified granocentric model prediction, Eq. (2.3.5) with no fitting parameters, is shown by the dotted curve.

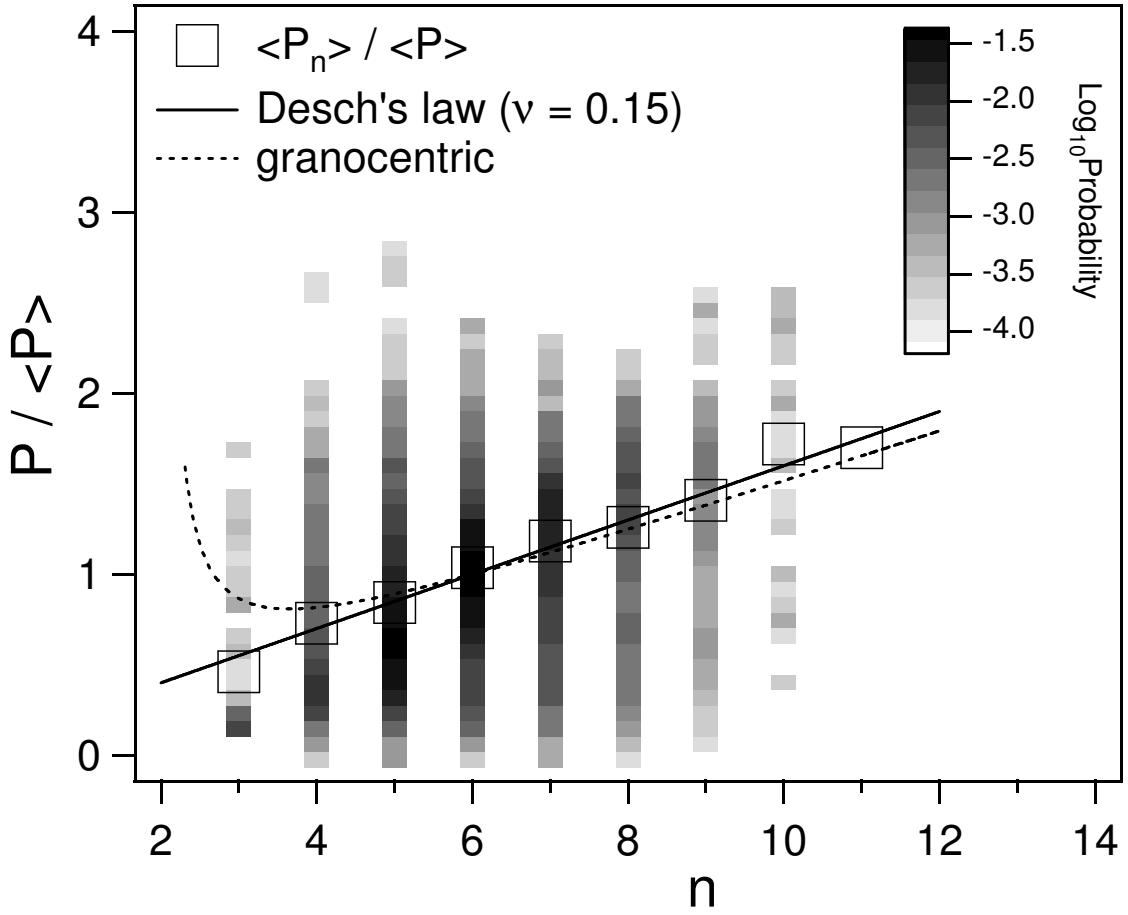


Figure 2.11: Normalized perimeter versus side number for all bubbles; the distribution is given in grayscale and the average is indicated by open squares. Note that the distributions is quite symmetric around the average. The fit to Desch's law, Eq. (2.3.4) with fitting value $\nu = 0.15 \pm 0.01$, is shown by a solid line. The simplified granocentric model prediction, Eq. (2.3.6) with no fitting parameters, is shown by the dotted curve.

is proportional to its perimeter, then entropy is maximized when Desch's law is satisfied [72]. Such size-topology relations continue to be a subject of active research [88, 79, 14, 48, 68].

To compare the Lewis and Desch laws with our scaling-state foams, we accumulate time-average statistics for areas and perimeters separately for each side number. The averages are given in Table 2.4 and are plotted versus $n$ as open squares in Figs. 5.3.1-5.3.2, respectively. The scaled average area and perimeter are both indistinguishable from 1 for $n = 6$, and both grow with $n$ since larger bubbles tend to have more sides. For area, the dependence is noticeably faster than linear; for perimeter, the dependence is indistinguishable from linear. Thus the Desch law provides a better description of scaling regime foams than the Lewis law, as seen by displayed fits. Indeed the average area data are better fit to $\langle A_n \rangle / \langle A \rangle = (0.027 \pm 0.001) n^2$, in accordance with some simulations and experiments [88, 14]. The perimeter data are well fit to the Desch law with $\nu = 0.15 \pm 0.01$. This is somewhat smaller than previous experimental measurements of $\nu = 0.29$ [88], and $\nu = 0.19$ [14].

Apart from the behavior of the averages, the correlation of side number with perimeter has an advantage over area because of the shapes of the distributions, which are also displayed in Figs. 5.3.1-5.3.2 in grayscale. For area, these are skewed so that the mode is significantly smaller than the average, especially for small $n$ where the peak is near zero as for an exponential distribution. For perimeter, by

contrast, the individual distributions are more symmetrically peaked so that the mode coincides closely with the average.

Regarding the deviation from Lewis' law, it is predicted that this is associated with deviation of the area distribution from exponential [48]. Indeed the area distribution data in Fig. 2.9a are not quite exponential. Further insight into the deviation from the Lewis law has been gained from the granocentric model [10]. In a simplified version [68], a Voronoi-type construction is made for a central particle uniformly surrounded by $n$ equidistant neighbors of the same same size. This gives the following size-topology relations, without any parameters:

$$A_n/\langle A\rangle = n/[4\sqrt{3}\sin(2\pi/n)], \tag{2.3.5}$$

$$P_n/\langle P\rangle = n/[4\sqrt{3}\cos(\pi/n)]. \tag{2.3.6}$$

The first of these is Eq. (7) from Ref. [68] and the second we derived in analogy. The angle brackets have been removed from $A_n$ and $P_n$ because for a given $n$ there is no distribution in this version of the granocentric model. These forms are included in Figs. 5.3.1-5.3.2, and agree quite well with the data.

### 2.3.4 Shape

The bubbles in a foam have a wide variety of shapes, even for a given number of sides. Two shape descriptors that we find in the next section to be relevant for

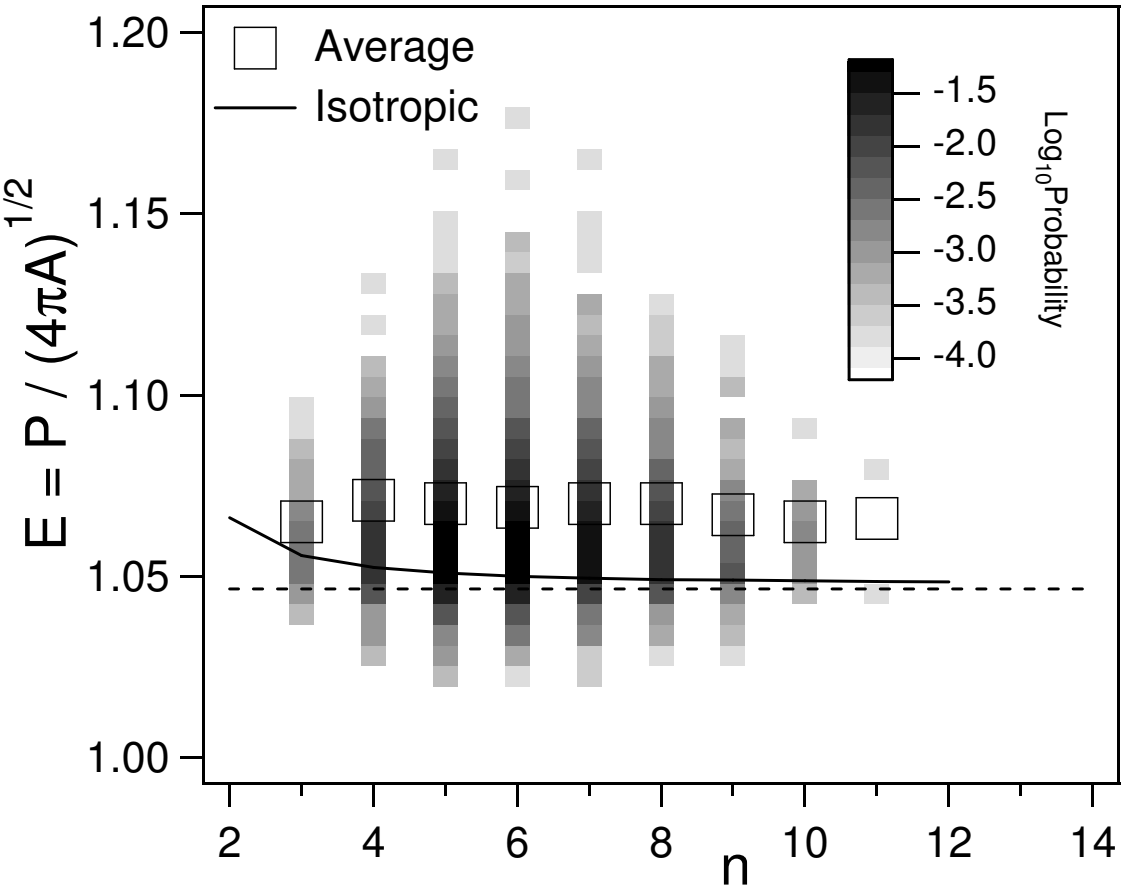


Figure 2.12: Elongation versus side number $n$, averaged over all times and liquid contents, where $P$ is bubble perimeter and $A$ is bubble area. The probability distribution is shown in grayscale, and the average is shown by open squares. The solid line represents the elongation for isotropic bubbles, given by Eq. (2.3.10); the horizontal dashed line represents $\pi/3 = 1.047$, the limit as $n \to \infty$.

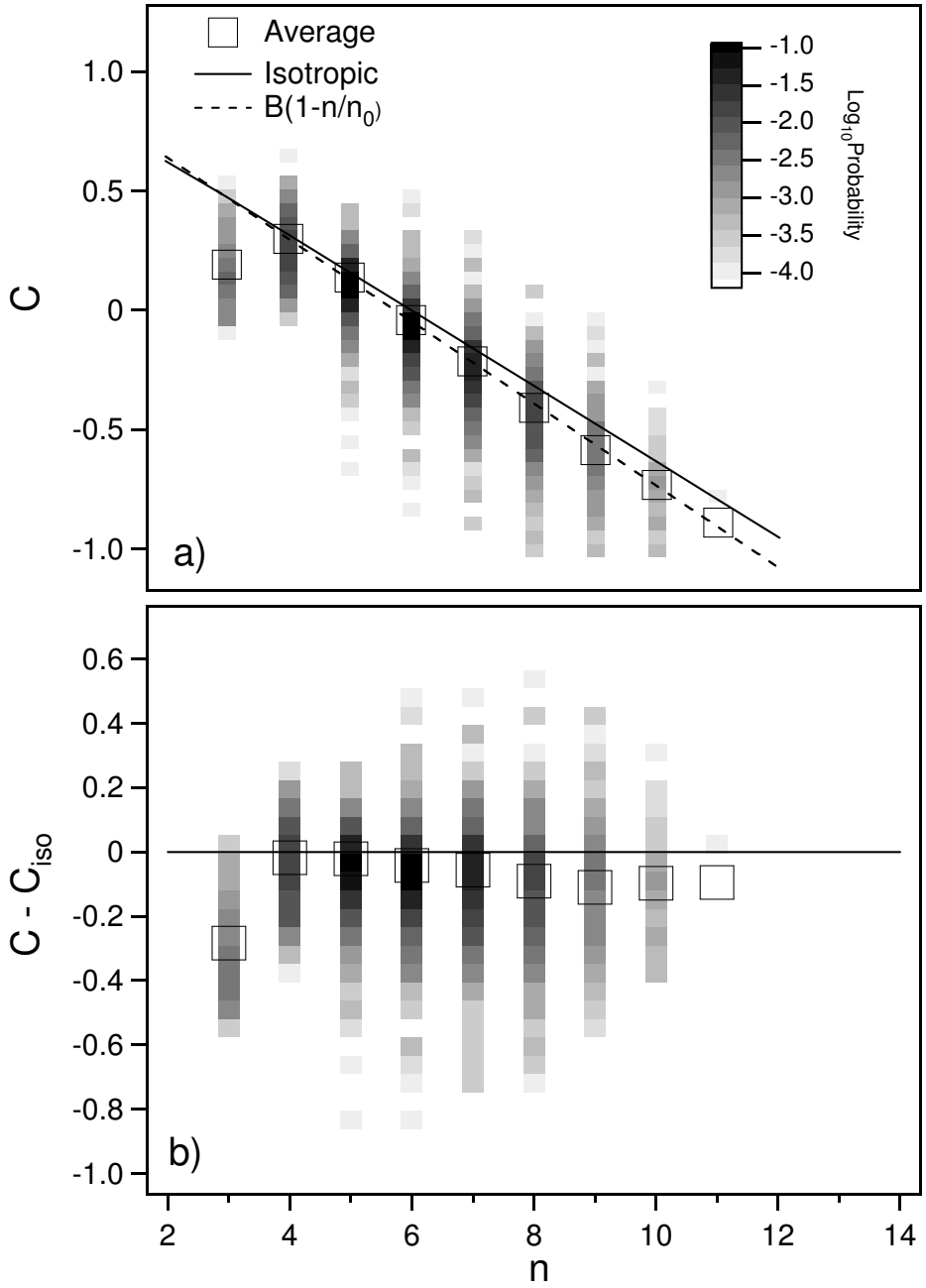


Figure 2.13: (a) Circularity $C$, defined by Eq. (2.3.8), versus side number $n$, averaged over all times and liquid contents. The probability distribution is shown in grayscale, and the average is shown by open squares. The solid curve represents the circularity for isotropic bubbles, given by Eq. (2.3.11). The dashed line is a fit to $B(1 - n/n_0)$, which gives $B = 0.99 \pm 0.02$ and $n_0 = 5.73 \pm 0.04$ when the $n = 3$ data are excluded. (b) The difference in circularity between actual and isotropic bubbles.

coarsening dynamics are the elongation and circularity, which we define respectively as

$$E = P/\sqrt{4\pi A}, \tag{2.3.7}$$

$$C = \left(\frac{1}{n}\sum_{i}^{n} 1/R_i\right)\sqrt{A/\pi}, \tag{2.3.8}$$

where $P$ is perimeter, $A$ is area, and $R_i$ is the radius of curvature for the $i^{\text{th}}$ side of an $n$-sided bubble. The sign convention is such that $R_i$ is positive for the bubble on the high-pressure side of the film. While the quantity $1/E^2$ is commonly known as "compactness", we follow Ref. [33] in referring to $E$ as "elongation". The term in brackets in Eq. (2.3.8) is an average curvature, with equal weights independent of side length; it is particular to shapes made from circular arc segments, and does not equal $2\pi/P$. For a circle, these definitions give a minimum elongation of $E = 1$ and a maximum circularity of $C = 1$. Note that $C = 0$ holds for any shape made of straight line segments. The simplified granocentric model treats cells as regular $n$-sided polygons, for which the shape descriptors are $E = \sqrt{(n/\pi)\tan(\pi/n)}$ and $C = 0$.

For comparison with data, we compute the shape descriptors for "isotropic" or "regular" bubbles consisting of equal arc segments. These are like regular polygons but with edges replaced by circular arcs, all of radius $R$, that meet at 120° as required by Plateau's laws. Isotropic bubbles have been used to model both two-

[33] and three-dimensional [36, 37, 30, 31] foams. We find:

$$P = (\pi/3)\,|n-6|\,R, \tag{2.3.9}$$

$$E = \sqrt{\frac{(\pi/3)(n-6)^2}{3n\left[\cot(\pi/n)-\sqrt{3}\right]-2\pi(n-6)}}, \tag{2.3.10}$$

$$C = \pm\sqrt{\frac{n}{4\pi}\left[\cot(\pi/n)-\sqrt{3}\right]-\frac{1}{6}(n-6)}. \tag{2.3.11}$$

The positive root $C > 0$ is taken for $n < 6$, and the negative root $C < 0$ is taken for $n > 6$. Our expression for the elongation is consistent with Eq. (A3) of Ref. [33], except that our definition includes a factor of $\sqrt{4\pi}$; it approaches $E = \pi/3 = 1.047$ in the limit $n \to \infty$. For $n \geq 3$ our expression for the circularity is within 0.5% of $C = (\pi^2/12)^{1/4}(1-n/6) = 0.95(1-n/6)$, the linear expansion around $n = 6$. Both Eqs. (2.3.10-2.3.11) behave badly for $n \leq 1$, but approach $E = 1$ and $C = 1$ in the limit $n \to 0$, as expected for a circular bubble with $n = 0$ vertices.

We now compute the shape parameters for all the bubbles in all the collected images. For both, area is taken from the number of enclosed pixels. For elongation, perimeter is taken from a LabVIEW routine that interpolates the pixellated boundary of the image. For circularity, the curvature of each segment is taken from the circle defined by the two endpoints and the average of the three middle-most points. No systematic deviation was ever observed between such arc segments and the pixellated bubble boundaries. Collecting all results, we find that both $E$ and $C$ are independent of age and liquid content and hence may be combined for better statistics. The average elongation and the average circularity are plotted versus

side number in Figs. 2.12-2.13, respectively. The probability distributions are also shown in grayscale, and appear to be peaked fairly symmetrically around the average values. Remarkably, the average elongation appears to be nearly constant and independent of $n$. Averaging over at all times and all liquid contents and all side numbers gives an average bubble elongation of $\langle E \rangle = 1.0692 \pm 0.0005$ and a variance of $e_2 = 0.004 \pm 0.001$. This is about 50% more elongated from a circle than for isotropic bubbles, Eq. (2.3.10). The data for circularity is nearly linear in $n$ and agrees fairly well with the expectation for isotropic bubbles, Eq. (2.3.11), except for three-sided bubbles. The difference between actual and isotropic bubble circularities is shown for comparison in Fig. 2.13b. The circularity data are well fit to $C(n) = B(1 - n/n_0)$, which gives $B = 0.99 \pm 0.02$ and $n_0 = 5.73 \pm 0.04$ when $n = 3$ data are excluded. The average variance of the circularity distributions is $c_2 = 0.08 \pm 0.01$.

## 2.4 Coarsening Dynamics

### 2.4.1 Data

All measurements discussed so far have been for individual static photographs and have not involved how individual bubbles change over time. It is also possible to track individual bubbles over time and observe how various quantities change. This was shown earlier, in Fig. 2.3, for selected bubbles of various $n$ for three liquid

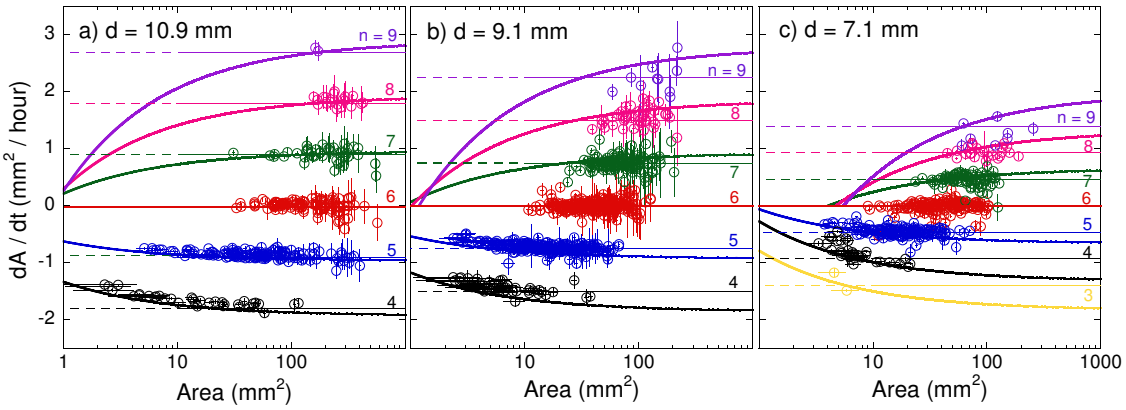


Figure 2.14: Rate of area change versus area, for individual bubbles in three foams with increasing liquid content, from left to right, as controlled by the distance $d$ of the foam above the liquid reservoir. The number $n$ of sides of each bubble is indicated by symbol color, as labeled. The thin horizontal lines represent a fit to von Neumann's law, $\mathrm{d}A/\mathrm{d}t = K(n-6)$ where $K$ is adjusted fit to the data for $A > 10$ mm$^2$. The fitted values of $K$ are plotted versus liquid content Fig. 2.16. The thick curves represent the border-blocking model, Eq. (2.4.5), where $K_0 = 1.2$ mm$^2$/hr is fixed by the data in Fig. 2.4, $E$ and $C$ are taken from the averages represented by the open squares in Figs. 2.12-2.13, and $r$ is the only fitting parameter. The fitted values of $r$ are plotted versus liquid content Fig. 2.17.

contents. In this plot it can be seen that the rate of change of an $n$-sided bubble's area is slower for wetter foams.

It is possible to measure the area at each time for each bubble in a sequence of images and fit these curves to a line for each bubble. The slope is $\mathrm{d}A/\mathrm{d}t$ for that bubble. In this way it is possible to measure $\mathrm{d}A/\mathrm{d}t$ for a large number of bubbles. We can then plot $\mathrm{d}A/\mathrm{d}t$ against area for a given liquid content. Examples of this for three different liquid contents are shown in Fig. 2.14. In these graphs each point is one bubble and the color indicates the number of sides. The horizontal lines are $\mathrm{d}A_n/\mathrm{d}t = K(n-6)$ for various $n$ where $K$ is the slope of the proportionality when the data on the plot is plotted as $\mathrm{d}A/\mathrm{d}t$ against $n-6$. On these plots, $K$, the coarsening rate, is the spacing between these horizontal lines. The values of $K$

are shown against liquid content in Fig. 2.16. The first thing to note is that the coarsening rate decreases as the liquid content increases. This makes sense as more liquid in the foam should prevent diffusion. Note also that there is a deviation from von Neumann's law for small bubbles. Von Neumann's law predicts that all bubbles with a given number of sides should coarsen at the same rate; therefore all points of a particular color should fall on the horizontal line of the same color. Instead, we see that small 4 and 5 sided bubbles fall above the appropriate line, which is to say they are shrinking more slowly than predicted. Very small bubbles with $n > 5$ are not observed because by the time the foam has become two dimensional, there are no very small bubbles with $n > 5$ and these bubbles do not shrink, so no examples ever become small enough to observe this effect. Note also that this deviation appears to be greater for higher liquid contents. This behavior is explained in the next section.

### 2.4.2 Border-blocking Model

In this section we model the effects of increasing liquid content, both on slowing the coarsening rate and in causing deviation of small bubbles from von Neumann's law. To this end we construct a 'border blocking' model, with the same assumptions used in the models of Refs. [4, 38, 35]. Namely, the Plateau borders swell with liquid and totally block gas diffusion, reducing the film area and hence slowing the rate of coarsening. And, as usual, we take the film thickness to be a constant independent of liquid content. While the prior models dealt only with average growth rates, we

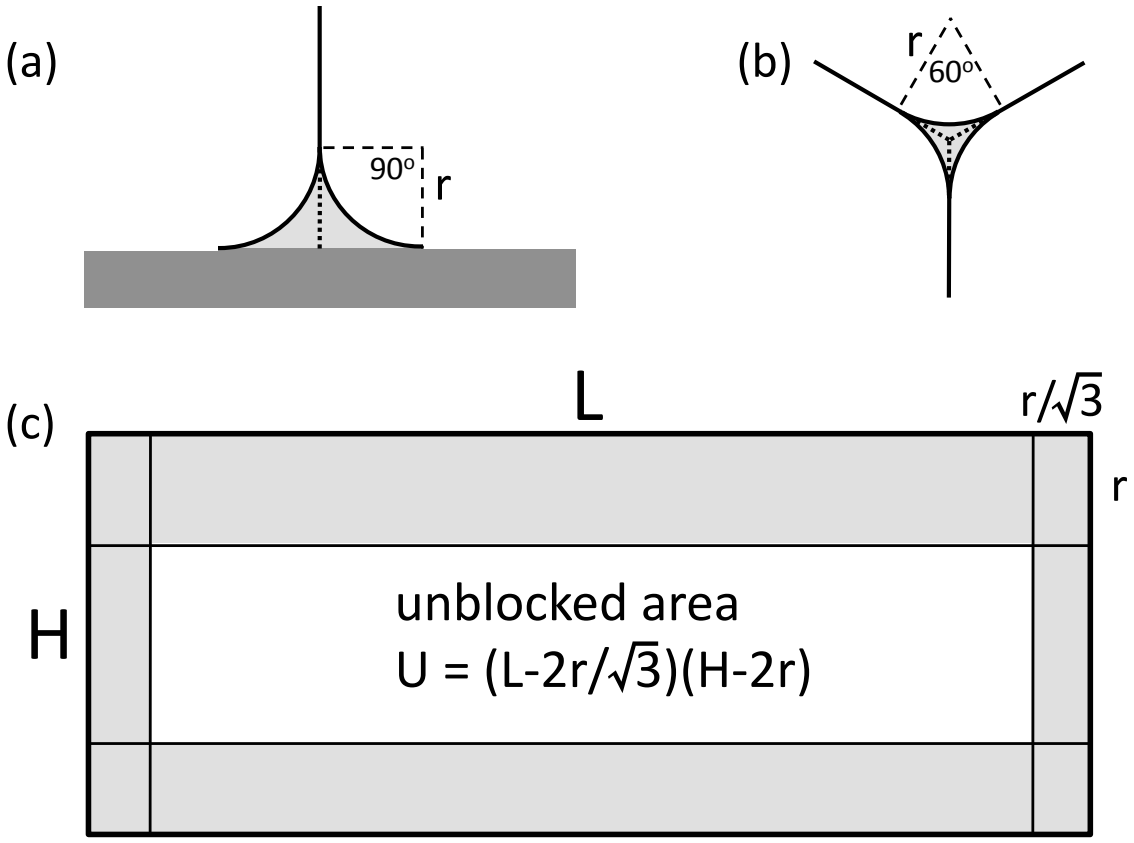


Figure 2.15: Cross section of wet (a) boundary, and (b) vertical, Plateau borders, and also (c) schematic of a vertical soap film. The Plateau borders have radii of curvature $r$, and are shaded light gray in (a-c). The blocked portions of the films, though which gas is assumed not to diffuse, are represented by dotted lines, and are seen to have respective length of (a) $r$ and (b) $r\tan(30°) = r/\sqrt{3}$. As shown in (c), this give the central unblocked area of the film as $U = (L-2r/\sqrt{3})(H-2r)$, where $L$ and $H$ are respectively the length and height of the film in the dry limit $r \to 0$.

now consider the effect of border blocking on individual bubbles through explicit modification of von Neumann's law.

The rate $\mathrm{d}V/\mathrm{d}t$ at which a bubble's volume changes with time is proportional to the sum of the gas diffusion rates across all its films. And the gas diffusion rate across each film is proportional to the Laplace pressure difference and the film area. For the quasi-2d experiments here, vertical soap films span the gap $H$ between

plates and have constant radius of curvature $R$ along the plates. As the starting point, we therefore take

$$\mathrm{d}V/\mathrm{d}t \propto -\sum_i (\gamma/R_i)U_i, \tag{2.4.1}$$

where the Laplace pressure $\gamma/R_i$ is positive for concave films and $U_i$ is the unblocked area through which gas is free to diffuse. To aid in computing the left and right-hand sides of this expression, we show the salient geometrical features of the Plateau borders and films in Fig. 2.15. As before, $H$ is the gap between the plates. And we define $L_i$ as the arclength of the films in the dry limit. For simplicity we take the radius of curvature of the Plateau borders as $r = \gamma/(\rho g d)$, Eq. (2.2.1), to be the same everywhere – for the boundary borders at the top and bottom plates and along the vertical borders where three films meet. We also assume that the vertical Plateau borders are symmetric. By the decoration theorem, the swelling of Plateau borders with liquid does not affect the soap films – liquid is merely painted onto the Plateau borders. Hence $R_i$ and $L_i$ are independent of liquid content.

The first task is to compute the left-hand side of Eq. (2.4.1), $\mathrm{d}V/\mathrm{d}t$, in terms of the observable skeletonized bubble area $A$. From the schematic diagram in Fig. 2.15a, it may be seen that the boundary Plateau borders have cross sectional area $(1 - \pi/4)r^2$ inside each bubble. Thus the bubble volume is $V = AH - (1 - \pi/4)r^2 \cdot (2P)$, minus smaller terms due to vertical Plateau borders and vertices. And the bubble perimeter may be expressed from the definition of

elongation as $P = \sqrt{4\pi A}E$. All this gives

$$\frac{\mathrm{d}V}{\mathrm{d}t} = H\frac{\mathrm{d}A}{\mathrm{d}t}\left[1 - \left(1 - \frac{\pi}{4}\right)\frac{\sqrt{4\pi}Er^2}{H\sqrt{A}}\right]. \tag{2.4.2}$$

For wet foams, bubble volume is not quite proportional to bubble area; the correction depends on shape and is more important for wetter foams and smaller bubbles.

To compute the unblocked film area $U$ as a function of liquid content, note from from Fig. 2.15a that the length of film blocked by a boundary border is simply $r$. And from Fig. 2.15b the length of film blocked by vertical border is $r\tan(30°) = r/\sqrt{3}$. Each film is thus blocked by $r$ along top and bottom and by $r/\sqrt{3}$ along the sides, as shown in Fig. 2.15c. Thus the unblocked area is $U = (H-2r)(L-2r/\sqrt{3})$, where $L$ is the arc length of the curved film measured along the plates between centers of the swollen vertical borders (i.e. the films length as measured in the dry limit). The right-hand side of Eq. (2.4.1) is thus

$$\sum_i \frac{\gamma}{R_i}U_i \propto -\sum_i \frac{\gamma}{R_i}(H-2r)(L_i - 2r/\sqrt{3}), \tag{2.4.3}$$

$$\propto -\left(1 - \frac{2r}{H}\right)\sum_i \left(\frac{L_i}{R_i} - \frac{2r}{\sqrt{3}R_i}\right). \tag{2.4.4}$$

As in the usual derivation of von Neumann's law, the sum of turning angles around a bubble is $2\pi = \sum_i[(L_i/R_i) + \pi/3]$, since films in the dry limit are circular arcs that subtend angle $L_i/R_i$ and meet at angles of $2\pi/3$ at the center of the inflated vertical Plateau borders. The latter follows from the decoration theorem, which

holds since vertical Plateau borders do not merge [4]. Therefore the first quantity being summed in Eq. (2.4.4) is $\sum_i (L_i/R_i) = (\pi/3)(6-n)$. The other quantity being summed may be expressed as $\sum(1/R_i) = nC/\sqrt{A/\pi}$ by the definition of circularity.

Combining all the above ingredients we arrive at the final prediction for the rate of area change:

$$\frac{\mathrm{d}A}{\mathrm{d}t} = K_0 \frac{\left(1-\frac{2r}{H}\right)\left[(n-6)+\frac{6Cnr}{\sqrt{3\pi A}}\right]}{1-\left(1-\frac{\pi}{4}\right)\frac{\sqrt{4\pi}Er^2}{H\sqrt{A}}} \tag{2.4.5}$$

where $K_0$ is the proportionality constant in von Neumann's law for a perfectly dry foam with $r = 0$ (see Eq. (4.1.1)). Note that the overall coarsening rate is reduced with liquid content by a factor $(1-2r/H)$ that is the same for all bubbles. However there are also two terms that depend on the *shape* of the bubble, via circularity $C$ and elongation $E$, and that cause deviation from the usual $(n-6)$ von Neumann behavior. Both of these terms become more important for wetter foams and smaller bubbles.

Before comparing Eq. (2.4.5) with data, we first emphasize the assumptions on which it is based. First, it incorrectly assumes that the liquid in the Plateau borders totally blocks the diffusion of gas; rather, gas can diffuse through borders too, but at a slower rate. Second, it assumes that the liquid in the vertical Plateau borders does not cause deviation in the angles from Plateau's laws, i.e. that the decoration theorem holds. This should be valid, as discussed above. Third, for simplicity, it incorrectly assumes that radius $r$ of the borders is constant; rather, it decreases continuously as a function of the height above the liquid reservoir. Despite these

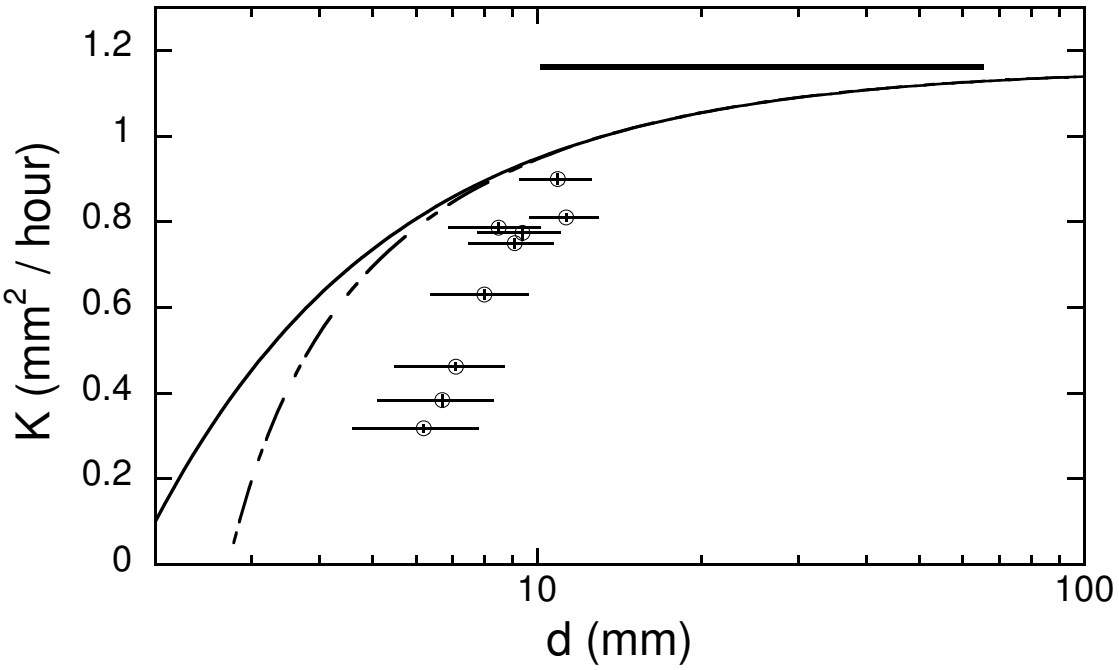


Figure 2.16: Coarsening rate $K = (\mathrm{d}A_n/\mathrm{d}t)/(n-6)$, versus height $d$ of the foam above the liquid reservoir. Values correspond to the thin-line fits in Fig. 2.14. The solid curve is the predicted relationship $K = K_0(1-2r/H)$. $K_0$ is the observed coarsening rate for very dry bubbles, $1 < d < 6$ cm, shown as a horizontal line. This value corresponds to the fit in Fig. 2.4. The dashed curve is the expected average $K$ if the top and bottom plates have different $r$, owing to the gap $H$ of the sample cell.

issues, we show next that the model fits the data well and explains the deviation from von Neumann's law for small wet bubbles.

### 2.4.3 Comparison

We analyze our coarsening rate data in two ways. The first is a standard von Neumann-type analysis for bubbles large enough that Eq. (2.4.5) reduces to $\mathrm{d}A/\mathrm{d}t = K_0(1-2r/H)(n-6)$, i.e. that $\mathrm{d}A/\mathrm{d}t = K(n-6)$ holds and is independent of $A$. For this we plot $\mathrm{d}A/\mathrm{d}t$ versus $(n-6)$ for each bubble for a given liquid content, and fit for an overall coarsening rate, $K$. These fits correspond to the horizontal lines in Fig. 2.14,

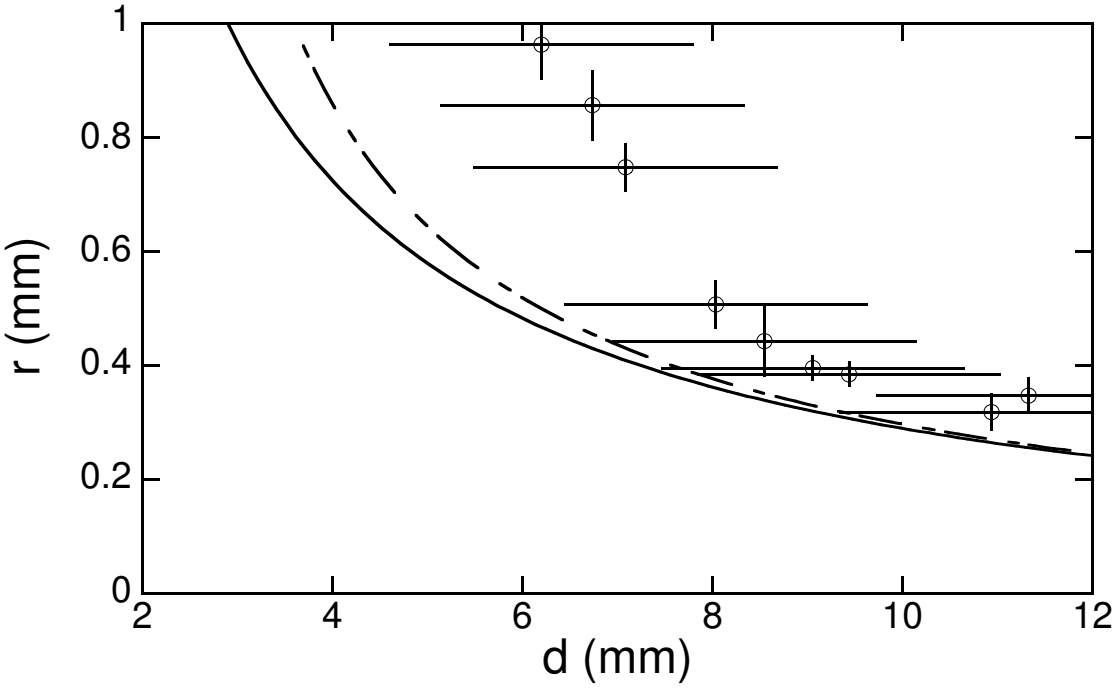


Figure 2.17: Fitted value $r$ versus height of the foam above the reservoir. Values correspond to the heavy-curve fits in Fig. 2.14. Solid line is the expected relationship $r = \gamma/\rho g d$. The dashed line is the expected average $r$ if the top and bottom plates have different $r$, owing to the gap $H$ of the sample cell.

which show satisfactory von Neumann behavior for bubbles with area $A > 10$ mm$^2$. The fitting results for $K$ are plotted in Fig. 2.16 versus the height $d$ of the foam above the liquid reservoir. The expectation, $K = K_0(1 - 2r/H)$ with $r = \gamma/\rho g d$ and $\gamma = 25$ dynes/cm, is also shown for comparison. The trend is correct, but not quantitatively so. Allowing for $r$ to be different at the top and bottom plates due to their difference in height improves the agreement, which is shown as a dotted line on the graph.

The second analysis is to fit the $\mathrm{d}A/\mathrm{d}t$ vs $A$ data shown in Fig. 2.14 to the border-blocking prediction, Eq. (2.4.5), by adjusting only the value of $r$. The value of $K_0$ is fixed to 1.2 mm$^2$/hr, as found from Fig. 2.4 for the dry foam limit. For each $n$, the values of $E$ and $C$ are taken from average elongation and circularity given by the open squares observed in Figs. 2.12-2.13, respectively. The gap $H$ between the plates is large enough, however, that the term involving $E$ ranges from 0.01 to 0.15 and hence is relatively minor. Only data for bubbles with $n \leq 5$ was used to calculate a fit for $r$ because only these bubbles included small bubbles that deviated from von Neumann's law. This gives fits such as shown by the heavy curves in Fig. 2.14. We see that the model fits the coarsening rate data quite well, accurately capturing the deviation from von Neumann's law with a single fitting parameter, $r$. The fitted values of this parameter are plotted in Fig. 2.17 versus liquid content and compared with the expectation $r = \gamma/\rho g d$. The trend and order of magnitude is correct, but the agreement is not very good. Considering the variation in $r$ due to the height of the cell improves the comparison, but does not seem to account for

the full discrepancy.

## 2.5 Conclusion

In this chapter we have presented several advances. First we devised a novel sample cell that allows the liquid content of Plateau borders to be controlled while maintaining a two-dimensional structure consistent with the decoration theorem. With this apparatus and digital video imaging, we collected extensive data for bubble statistics and coarsening rates. Besides the usual side-number and area distributions, we also analyzed for correlations between size and topology and compared with several predictions. In addition we introduced several new quantities and demonstrated how they are important for the theory of coarsening. This includes the area-weighted side-number distribution, $F(n)$, and the area-weighted average side number, $\langle\langle n\rangle\rangle$, which have general importance via Eq. (2.1.4) for the rate of change of average bubble area in the scaling regime. This also includes two dimensionless parameters for specifying the shapes of bubbles – the elongation $E$ and the circularity $C$. We acquired extensive data on all four of these quantities, of which we are aware of no precedent. We also acquired extensive data for the rate of coarsening of bubbles, as a function of both side number and – more novelly – of liquid content. We find that increasing wetness causes a deviation from von Neumann's law, which becomes more important for smaller bubbles. This behavior we were able to model successfully in terms of an explicit modification of von Neumann's

law to include the blockage of gas diffusion by Plateau border. An interesting feature of this model is that the bubble shape parameters $E$ and $C$ both appear. Of the endless ways to quantify shape, these two actually have physical significance for the behavior of the bubbles in foam. Altogether our work significantly extends the description of the scaling regime of two-dimensional foams, and of the influence of wetness on coarsening. We hope this might help point the way for future studies of bubble-scale behavior in the coarsening of wet three-dimensional foams.

## 2.6 Appendix: Details of Image Analysis

To do the image analysis, we begin by running an edge finding algorithm. This uses a Sobel kernel to identify the edges in the image. We then due an automatic threshold using the metric method. We then filter out small particles. The cutoff is much smaller than the smallest bubble. This gets rid of particles resulting from smudges or dust on the apparatus or lens. We then run a separate particles algorithm. We then reject any particles with an aspect ratio greater than 8. This primarily gets rid of particles that make up the interior of the Plateau borders. We then skeletonize the image. This results in an image where all the particles are the bubbles of the foam, separated by single pixel width lines. We then label each bubble so that the interior pixels of each bubble all have a unique pixel value. Because of the skeletonization, all border pixels touch exactly two other border pixels, except for the vertices, which touch three. In this way we identify all the vertices. For each

vertex we identify the three bubbles that touch it. In this way we can then identify how many vertices correspond to each bubble, which is the same as $n$, the number of sides. We also record other particle statistics, such as centroid position, area (just the number of pixels in the bubble) and perimeter (the perimeter value is not just the number of edge pixels, but is smoothed on the pixel level by an internal LabVIEW routine).

For very wet foams (the two wettest liquid fractions in this experiment), light is channeled through the vertical Plateau borders to create spots of light in the image. This can be observed in Fig. 2.2c. It is necessary to ensure that these spots are not identified as bubbles. These spots when going through the initial image analysis, come out as triangle with very jagged edges. This is due to the fact that the channelization of the light results in the intensity of the spots going down smoothly from the center. These shapes are often elongated and very far from rectangles. To get rid of these spots, we filter the particles and reject any particle with a compactness less than 0.6. Compactness is defined as the area of the particle divided by the area of its bounding rectangle. This does a good job of getting rid of the channelized light spots without rejecting valid bubbles.

We also fit the edges of the bubbles to circles in order to calculate the circularity. All the skeletonized boundary pixels other than the vertices touch exactly two bubbles. For each pair of bubbles we identify all the pixels of the edge that separates those two bubbles. We then take the two vertices that correspond to this edge, as

well as the average of the three middle points of the edge. These three points define a circle. We then have the radius of curvature of the edge for use in calculating the circularity.

# Chapter 3

# New Measurements of Foam Structure and Hyperuniformity

## 3.1 Introduction

The structure of a two dimensional foam is set by Plateau's laws. These state that all vertices are threefold at 120° and films form arcs of circles [100]. These laws are determined by force balance, and any initial configuration will quickly relax to a state that satisfies these laws. The foam structure then evolves over time through a process called coarsening. This process is driven by gas diffusion across films, so that some bubbles grow and other bubbles shrink, and the average length scale increases over time. This process is very slow compared to the relaxation to satisfy

Plateau's laws.

It is believed that for any initial configuration of a two dimensional foam, evolution through the coarsening process will eventually result in a foam that is in a self similar scaling state. This state is one in which, other than an increase in an overall scale factor, the statistical properties of the foam will not change. Additionally, all initial configurations will reach the same scaling state, with the same overall statistical properties.

There have been experiments [27, 28, 84, 81, 83, 39, 77] and simulations [43, 26, 34, 80, 66, 78] that have characterized the properties of this scaling state. They have measured statistical distributions of bubble size, shape, and topology. They have found good agreement with each other, regardless of the initial method of foam preparation.

These measurements have focused on statistics that involve measurements of individual bubbles, such as the number of sides distribution and the area distribution. We are not aware of any attempt to use the types of measurements used to describe point patterns to describe foams. These types of measurements are based on the positional relationships of the points in the pattern. This can give information about the geometric structure of the foam.

One subset of point patterns that has received considerable interest is hyperuniform patterns [91, 104, 101, 102, 103]. These patterns are characterized by growth

in the number density slower than $R^d$, and an absence of infinite wavelength fluctuations. One reason for the interest in this type of pattern is that it is conjectured that all saturated, strictly jammed systems are hyperuniform [101]. Foams, as a highly polydisperse jammed system, provide an interesting case. Because they are so polydisperse, some typical tests for hyperuniformity, such as the structure factor and the two point correlation function - though they can give insight into the structure of the foam - do not conclusively indicate whether the structure is hyperuniform. Instead, measurement of the spectral density is necessary [101].

In this chapter we convert images of foam into point patterns two ways, the centroids and the vertices. Using measurements based on the positional relationships of these points, we gain insight into the structure of the scaling state of a two dimensional foam. By measuring the spectral density, we attempt to determine whether this system can be classified as hyperuniform.

## 3.2 Materials and Methods

The liquid foaming solution consists of 75% deionized water, 20% glycerin, and 5% Dawn Ultra Concentrated dish detergent, and has liquid-vapor surface tension $\gamma = 25$ dynes/cm. This creates foams that are stable and long lived; film ruptures were never observed. The sample cell consists of a circular chamber made from clear 1.91 cm thick acrylic plates separated by a $H = 3.2$ mm gap and sealed with

two concentric rubber O-rings, the inner of which is 23 cm in diameter. The gap thickness and seal are maintained by a bolt circle and metal spacers, all between the two O-rings. To create the foam, the chamber is first completely filled with solution. Pure nitrogen is then pumped into the chamber until only the desired amount of liquid remains. This is accomplished via two valved ports attached on opposite sides of the bottom plate. The chamber is then shaken vigorously until it is completely filled by a uniform opaque foam with sub-millimeter size bubbles, smaller than the gap between the plates. The initial foam is thus three dimensional. Immediately after production it is placed 20 cm away from a Vista Point A lightbox, and 2.5 m from a Nikon D80 camera with a Nikkor AF-S 300 mm 1:2.8 D lens. It is then left undisturbed to coarsen into a two-dimensional foam consisting of a single layer of bubbles with an average size greater than the gap, which typically requires two days. The field of view thus encompasses up to a few hundred bubbles. Photographs are taken at regular intervals for a few days up to two weeks. This process is repeated for foams of different liquid content, although we find that the scaling state does not depend on liquid content [77] so results are averaged over all photographs.

The images are cropped to a $12.7 \times 12.7\text{cm}^2$ region of interest. These images are thresholded and skeletonized, and the bubble centroids and the positions of the vertices are recorded. The centroids and the vertices represent two point patterns for each image. The sample point patterns for a single image can be seen in Fig. 3.1. For comparison a Poisson point process with density equal to the density of the vertices is also shown.

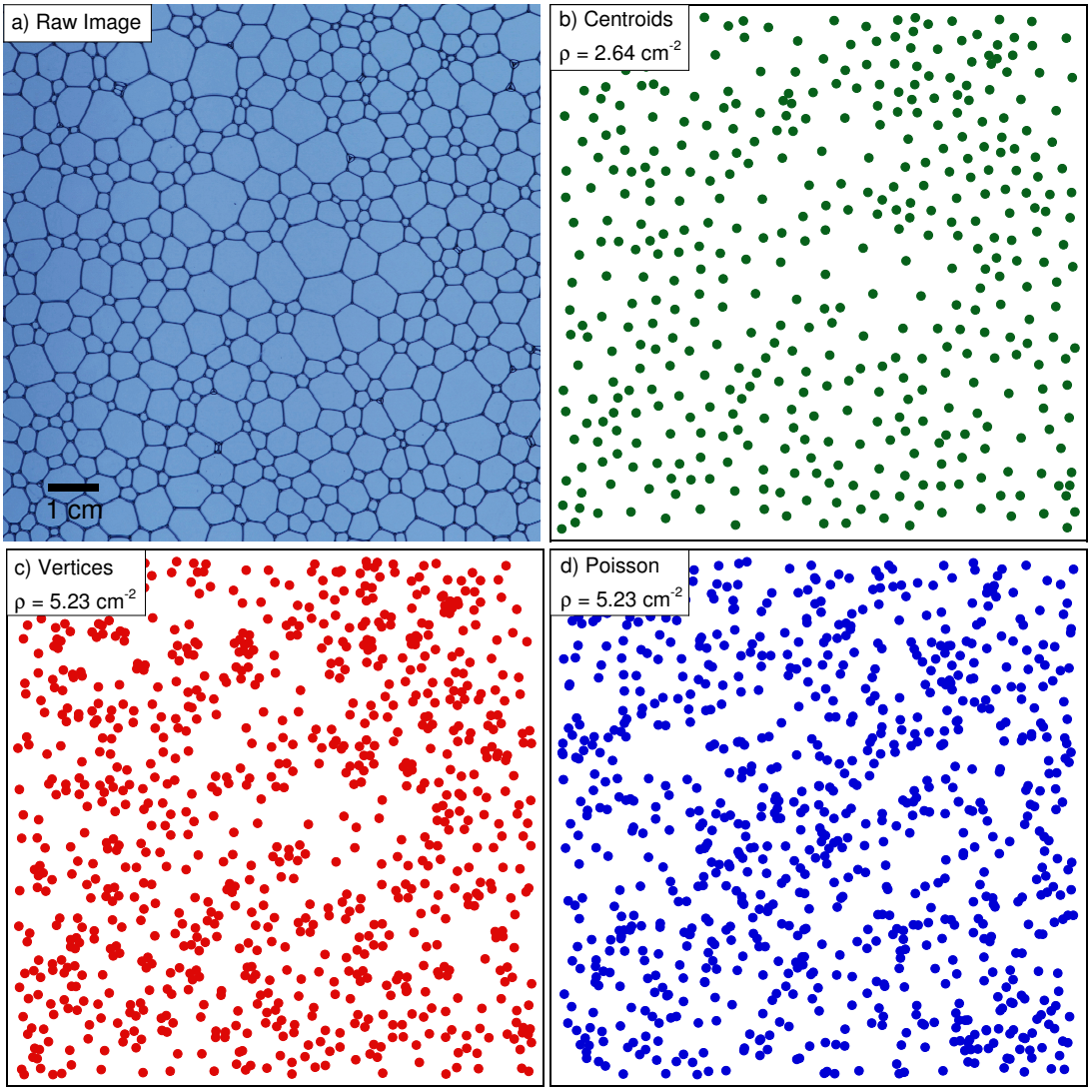


Figure 3.1: Part a) shows a sample raw image. Part b) shows the pattern of centroids for the sample image. Part c) shows the pattern of the vertices from the same image. Part d) shows a Poisson point pattern with density equal to the density of the vertices.

All measurements are averaged over 59 configurations. The number of bubbles in the configurations ranges from 450 to 50.

## 3.3 Structure Measurements

Measurements of foam structure in the past have focused on measurement of individual bubble statistics. Another means of describing the scaling state of the foam is to investigate quantities that are based on the positional relationships of the bubbles in the foam. There are many quantities that are used to describe point patterns, and we can use these same quantities to describe our foam.

The first step is to reduce our photograph of foam to a point pattern. We do this in two ways. The first is to isolate the centroids of the bubbles, and the other is to consider the vertices of the bubbles. These patterns can be seen for a sample image in Fig. 3.1. The first thing we want to do for our foam point patterns is to define a length scale for each photograph so that we can compare foams at different times and liquid contents. For each particle in our pattern, we calculate the distance to its nearest neighbor, $r$. We then can calculate the mean for all points in our pattern, and this is the length scale, $\lambda$. There is a different $\lambda$ for each photograph, and for a given photograph there are separate $\lambda$s for the centroids and the vertices. We can also look at the the distribution of this quantity for our patterns. Fig. 3.2a shows the distribution of nearest neighbor distributions for the centroids, combined over all

times and liquid contents, Fig. 3.2b shows the vertices, also combined for all times and liquid contents, and Fig. 3.2c shows an average of 10 Poisson distributions. The $r$s for the centroids and vertices are normalized by a length scale, $\langle A^{1/2}4/\pi\rangle$, where A is the bubble area, for each photograph, so that the patterns at different times, which have different densities, can be combined.

In the case of the Poisson distribution, there is an expected form for this curve. The probability density of the nearest neighbor distribution for a Poisson distribution is

$$H(r) = 2\rho\pi r e^{-\rho\pi r^2} \tag{3.3.1}$$

where $\rho$ is the number density of the point pattern, $r$ is the nearest neighbor distance, and $\lambda = \langle r\rangle$. We see that our Poisson distribution in Fig. 3.2c fits this form. The vertex distribution, while skewed, is not as skewed as the Poisson distribution. The expected Poisson form is too high for small $r$, and is peaked lower than the data. The vertex distribution seems better fit by the form $(\pi^{1/2}/4)a^{3/2}r^2e^{-r^2/a}$ where $a$ is a fitting parameter we measure to be 0.08. The centroid distribution, unlike both the vertices and the Poisson distribution, is highly symmetric. It is well fit to a Gaussian form.

Another quantity we can look at is the structure factor. We calculate the struc-

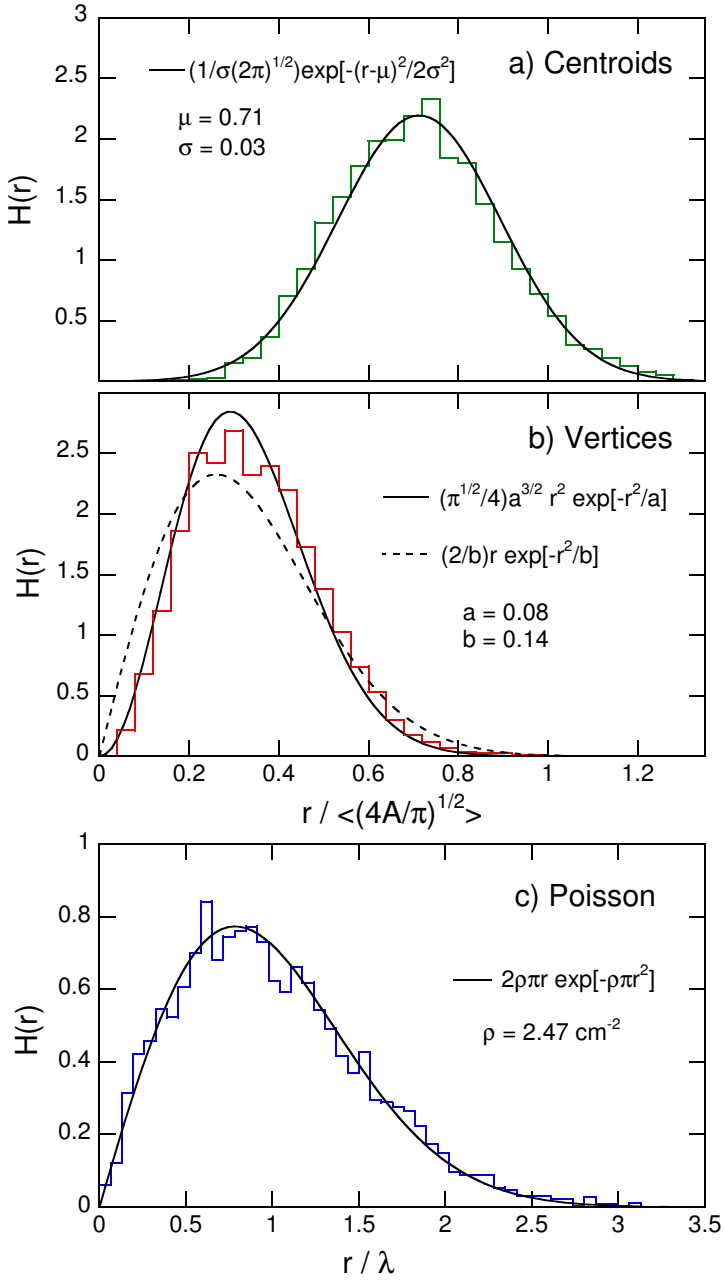


Figure 3.2: Distribution of the distance of the nearest neighbor of a point. Part a) shows the distribution for the centroids combined for all times and liquid contents, normalized by $\langle A^{1/2}4/\pi\rangle$ where $A$ is the bubble area. The black line is a Gaussian fit to the data, and describes the data reasonably well. Part b) is the distribution for the vertices combined for all times and liquid contents, normalized by the same factor as part a). We see that the distribution for the vertices is much more skewed than for the centroids. We fit the distribution to the form $(\pi^{1/2}/4)a^{3/2}r^2e^{-r^2/a}$ where $a$ is a fitting parameter we measure to be 0.08. The bottom plot is the distribution for the average of 10 Poisson distributions. Here we normalize $r$ by the average value, $\lambda$. We see that the data is fit well by the expected form of Eq. (3.3.1).

ture factor directly from the point pattern using the equation

$$S(\mathbf{k}) = \frac{1}{N}|\sum_{j=1}^{N} e^{i\mathbf{k}\cdot\mathbf{r}_j}| \tag{3.3.2}$$

where $N$ is the total number of points. For our plots we average over all $|\mathbf{k}| = k$. The structure factor does not depend on time or liquid content after we normalize by $\lambda$, so we average over all times and liquid contents. We see in Fig. 3.3 that the curves for the vertices and the Poisson distribution have the same form and are constant. We expect the infinite system Poisson distribution to have a constant value of $S(k) = 1$. That indicates that they are both essentially random and without structure. However, the curve for the centroids has a noticeable dip for small $k$. This is consistent with what we see in the distributions. While the Poisson distribution has no minimum neighbor distance, and the vertex distribution also has very close points, the distribution for centroids is much more symmetrical, and has no values very close to zero. This could be due to an effective minimum bubble size set by the area at which bubbles become 3D.

Additionally, there are additional topological and size-topology correlations that are obeyed by foams. There is a relationship, known as the Aboav-Weaire law, that says that bubbles with many sides are likely to have neighbors with few sides and vice versa [100]. Also, on average, bubbles with more sides have a larger area [77]. Combining these two properties of the scaling state of two dimensional foams means that large bubbles are more likely to be next to small bubbles and vice versa. This

may also be a source of structure in the centroid pattern.

Another measurement is the pair correlation function, $g(r)$. This quantity measures the likelihood of two randomly chosen points having the given separation. As with the structure factor, we see that the curves for the vertices and for the Poisson distribution are very similar and display no structure. We expect the infinite system Poisson distribution to have a constant value $g(r) = 1$. Again the curve for the centroids is different, with a clear peak and a decrease for small $r$. This is again consistent with a minimum bubble size and a preference for large bubbles and small bubbles to be near each other.

A third measurement that we looked at is the number variance, $\sigma^2$. We take 10000 circles of radius $R$ and place them randomly on our image, and find the variance in the number of points that fall inside each circle. In the case of a random distribution, this quantity will just grow with the area of the circle. To make this more visible, we normalize by $R^2$. The curve for the Poisson distribution is normalized by its number density, so that it should have a constant value of 1. The curves for the centroids and the vertices are combined from photographs with very different densities, so they are not normalized in this way. We see that as before, the curves for the vertices and the Poisson distribution are similar. They are also flat, indicating that in both cases the variance grows as $R^2$, as we expect for a random distribution. In contrast, the curve for the centroids has a minimum. This is consistent with the results for $S(k)$ and $g(r)$.

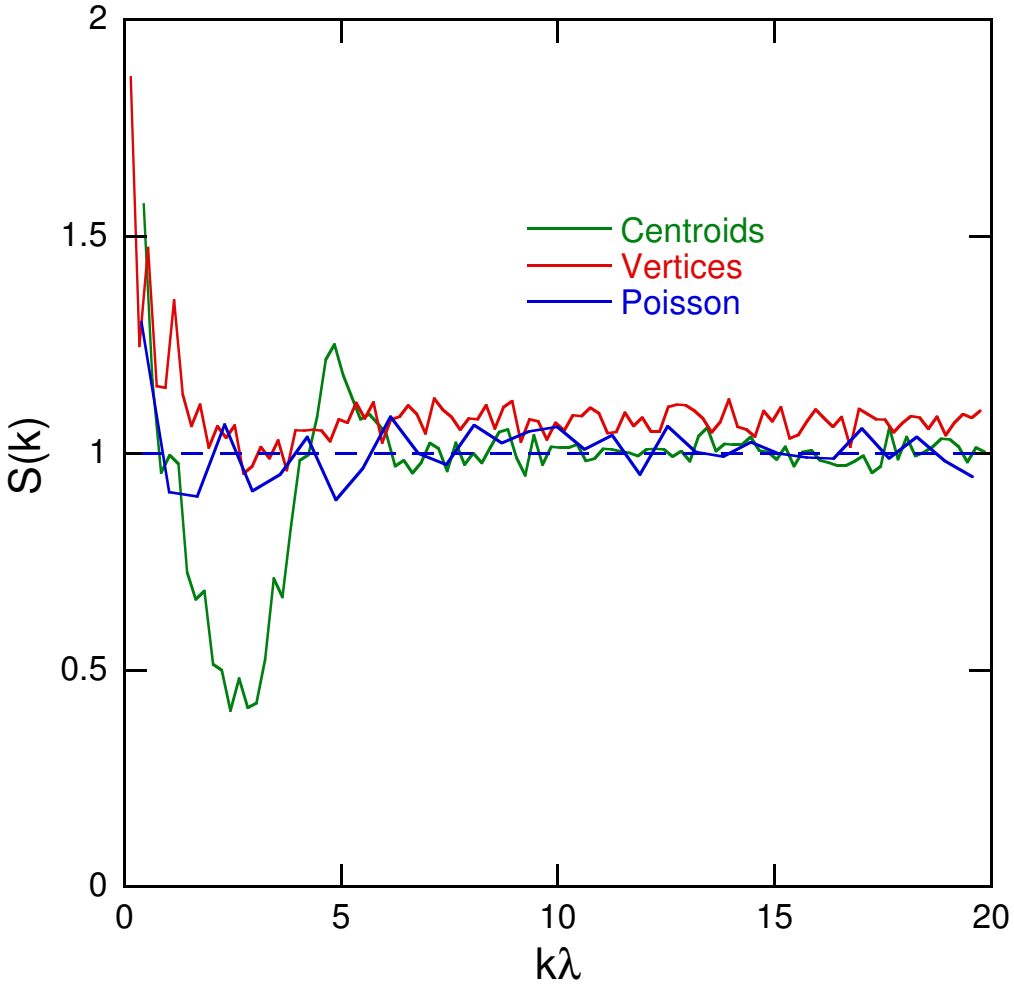


Figure 3.3: Structure factor for the centroids, vertices, and Poisson distribution plotted against the dimensionless wavenumber, $k\lambda$. The data for the centroids and vertices are averaged over all times and liquid contents. The Poisson curve is averaged over 10 Poisson distributions. The infinite system Poisson distribution should have a constant value of $S(k) = 1$. $\lambda$ is the mean of the nearest neighbor distance distribution. The equation for the calculation of the structure factor is shown in Eq. (3.3.2).

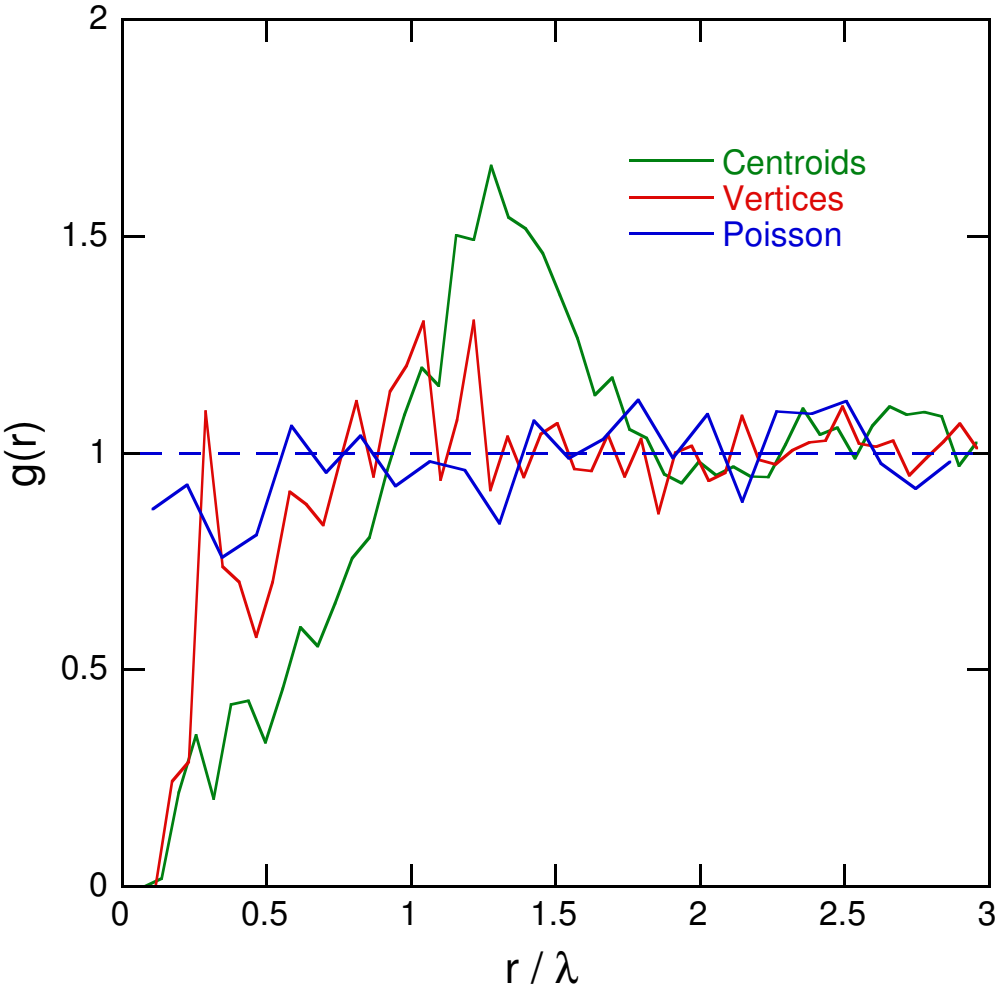


Figure 3.4: Pair correlation function for the centroids, vertices, and Poisson distribution plotted against the dimensionless radial distance, $r/\lambda$. The data for the centroids and vertices are averaged over all times and liquid contents. The Poisson curve is averaged over 10 Poisson distributions. The infinite system Poisson distribution should have a constant value of $g(r) = 1$ $\lambda$ is the mean of the nearest neighbor distance distribution.

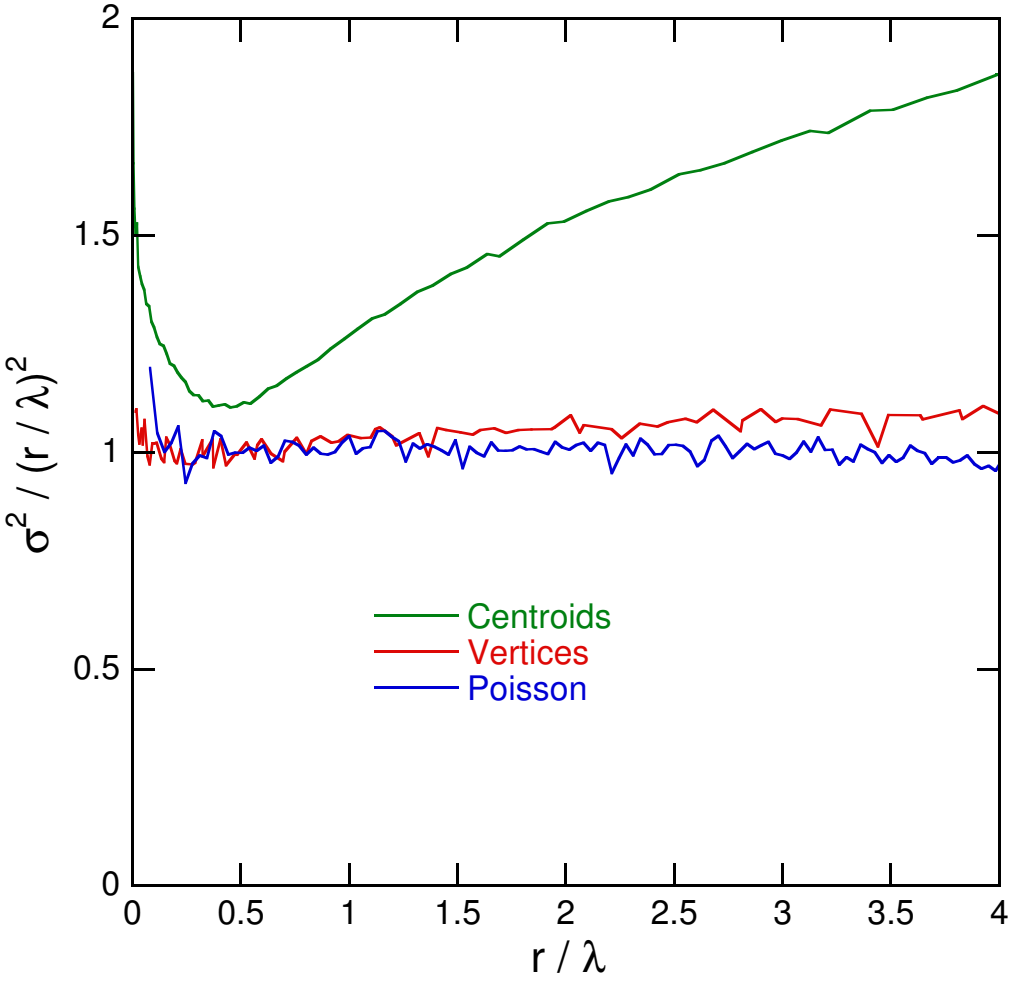


Figure 3.5: Normalized variance for the centroids, vertices, and Poisson distribution plotted against the dimensionless radius $R/\lambda$. The data for the centroids and vertices are averaged over all times and liquid contents To calculate the variance, a circle of radius $R$ is randomly placed on a photograph and the number of points falling within the circle are counted. This process is repeated 10000 times for each $R$ and the variance, $\sigma^2$ is calculated. $\lambda$ is the mean of the nearest neighbor distance distribution. The curve for the Poisson distribution is normalized by its number density, so that it should have a constant value of 1. The curves for the centroids and vertices are combined from many photographs of varying density, so they are not normalized in this way.

## 3.4 Hyperuniformity

There is a class of point patterns, known as hyperuniform patterns, that are characterized by an absence of infinite-wavelength fluctuations [91]. To our knowledge, there has been no study of whether the scaling state of a two-dimensional foam is hyperuniform. To determine whether a given point pattern is hyperuniform, the kinds of measurements we made in the previous section can all be useful. However, for highly polydisperse systems such as our foam, these measurements are inconclusive. To determine whether the pattern is hyperuniform, it is necessary to look at the spectral density [101].

To begin, we convert our centroid point pattern into a pattern of circles. To do this, we begin with our point pattern, and grow the circles until each one just touches the boundary of its bubble. This pattern, along with the bubble boundaries, can be seen for a sample configuration in Fig. 3.6. To calculate the spectral density, we subtract off the average value of the image, then take the absolute value of the Fourier transform and average over $k$. In order to average over all configurations, we normalize by the mean nearest neighbor distance, $\lambda$. The results for all centroid configurations are shown in Fig. 3.7.

The signature of hyperuniformity is for the spectral density to go to zero as $k$ goes to zero. The small $k$ limit corresponds to the large wavelength fluctuations in the system, so the measurements in this regime are limited by the system size. Because

the average bubble size increases with time, the smallest $k$ points on the curve correspond to only a small number of configurations. They are therefore quite noisy, and it is not possible to determine whether the curve is going to zero. Therefore, we cannot conclude whether the pattern of foam centroids is hyperuniform.

## 3.5 Conclusion

We converted our images of foam into point patterns in two ways, the centroids and the vertices. Using measurements of $g(r)$, $S(k)$, and $\sigma^2(R)$, we were able to get structural information about these point patterns. We found that the results for the point pattern of vertices was largely indistinguishable from a random Poisson process. However, the results for the centroids had clear structure, visible in our measurements of the structure factor, the pair correlation function, and the normalized number variance. These results were consistent with each other. We believe this structure is due to an effective minimum bubble size set by the area at which bubbles become 3D, and by a preference for large bubbles to be next to small bubbles and vice versa. It is conjectured that all saturated, strictly jammed particle packings are hyperuniform [101]. Foams are a case of a highly polydisperse jammed system. We measured the spectral density of the centroid pattern, but the results were not conclusive to determine whether the pattern is hyperuniform. Measurements of systems with more bubbles is needed to accurately determine the small $k$ behavior of the spectral density.

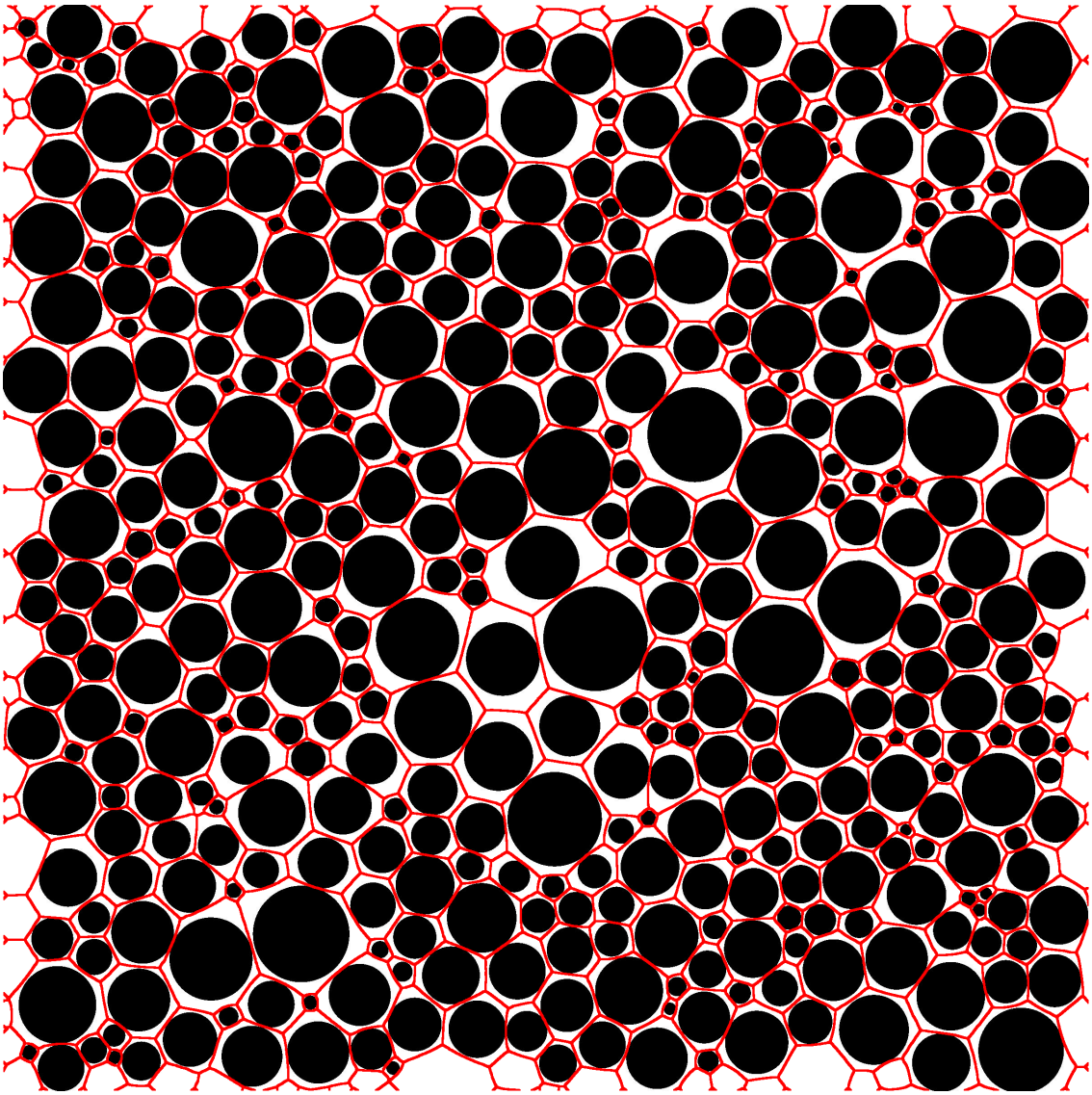

Figure 3.6: Circle pattern for centroids of a sample pattern used in the calculation of spectral density. The raw image corresponding to this pattern can be seen in Fig. 3.1. The boundaries of the bubbles are also shown.

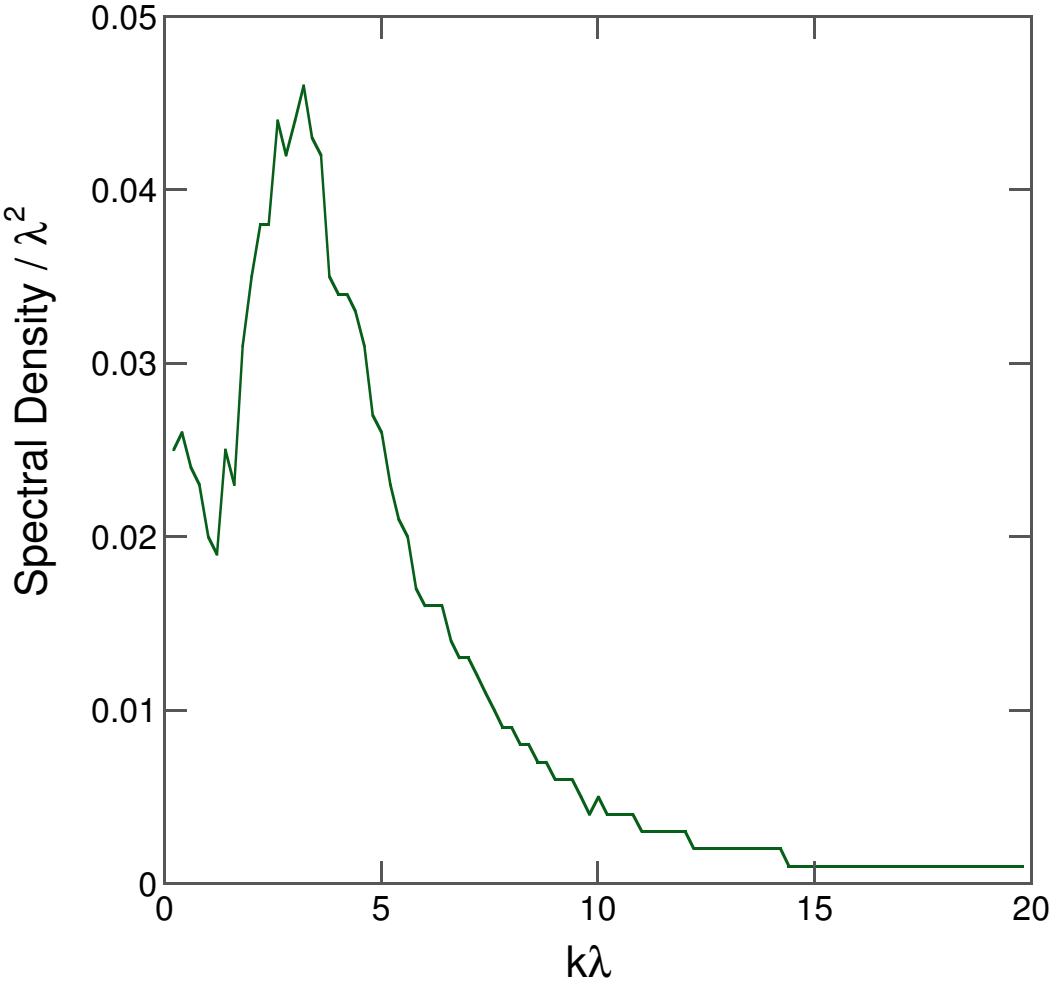


Figure 3.7: Spectral density averaged over all centroid configurations plotted against the dimensionless wavenumber, $k\lambda$.

# Chapter 4

# Coarsening of Two Dimensional Foam on a Dome

## 4.1 Introduction

Coarsening is a process in foams by which there is diffusion of gas across films such that some bubbles grow and other bubbles shrink. This progresses in such a way that the average bubble area increases over time [100]. Coarsening is not limited to foams, and is also relevant in other systems involving domain growth [29, 82]. For an ideal dry two dimensional foam, John von Neumann showed that the rate of

change of area of a bubble in a two dimensional foam is [67]:

$$\frac{\mathrm{d}A}{\mathrm{d}t} = K_0(n-6), \tag{4.1.1}$$

where $n$ is the number of sides of a bubble, and $K_0$ is a constant of proportionality. Remarkably, the shape of the bubble, its edge lengths, and its set of neighbors, all do not matter.

In 1992 Avron and Levine [1] generalized von Neumann's law to predict the rate of area change for bubbles coarsening on a curved surface. The essential ingredient is that the sum of turning angles around each bubble is no longer $2\pi$, as in flat space, but rather depends on the integral of Gaussian curvature, $\kappa_G$, over the bubble area. This modifies the von Neumann law to:

$$\frac{\mathrm{d}A}{\mathrm{d}t} = K_0 \left[ (n-6) + \frac{3}{\pi} \int \kappa_G \mathrm{d}A \right]. \tag{4.1.2}$$

In the case of a surface of constant positive curvature, such as a dome of radius $R$, this reduces to

$$\frac{\mathrm{d}A}{\mathrm{d}t} = K_0 \left[ (n-6) + \frac{3A}{\pi R^2} \right] \tag{4.1.3}$$

The rate of change of bubble area thus depends on the number of sides *and the area* of the bubble.

There have been numerous theoretical and simulation studies of coarsening for foams in two dimensional flat space [2, 43, 26, 34, 80, 21, 83, 66, 78], but to date

we are aware of only one simulation that includes the effect of substrate curvature [70]. There, the authors used a modified Potts model for a two dimensional foam coarsening on spheres, toroids, and pseudospheres. For spheres, they focus on how the area distribution and average area change over time, and find that at late times the dynamics are dominated by the appearance of 'singular bubbles' much larger than the average that quickly grow to cover the sphere. There is minimal discussion of the coarsening of individual bubbles, and no discussion of side number or other distributions of the system.

While the coarsening of foams in two dimensional flat space has been well-measured [27, 84, 81, 65, 3, 45, 75, 74, 77, 83, 39], we are unaware of any experiments to test the modified law of Avron and Levine for foam in two dimensional curved space. However metallurgical grain growth on curved substrates has been reported. In Ref. [50], the results are said to be preliminary and no growth rate data are shown. In Ref. [69], the deviation from the coarsening rate for flat space is masked by noise, but statistical analysis is reported to demonstrate consistency with Eq. (4.1.2). In this chapter we use a hemispheric cell to create a curved two dimensional foam. We use image analysis to track individual bubbles and measure bubble dynamics such as coarsening rate. We also measure bubble statistics, such as the distribution of number of sides and compare this to results from a flat cell. Our image quality and analysis methods are sufficient to demonstrate directly, for six sided bubbles, that the growth rates are different from flat space and are consistent with Avron and Levine [1].

## 4.2 Materials and Methods

To measure coarsening rates of two dimensional foams on a curved surface, we constructed a cell from two hemispherical polycarbonate domes. The smaller dome has an outer diameter of 12.5 cm, and the larger dome has an inner diameter of 13.3 cm, creating a 4 mm gap. The smaller dome was glued to a flat acrylic plate. The larger dome was placed over the smaller dome and separated from the plate by an O-ring of diameter 0.25 inches. We were careful to ensure that the two domes were aligned concentrically. The upper dome was then screwed to the plate to create a sealed chamber of constant curvature.

The solution we used to create our foam was a liquid consisting of 75% deionized water, 20% glycerin, and 5% Dawn Ultra Concentrated dishwashing liquid. This created a foam that was stable and generally lasted many days. The foam was prepared by putting 35 mL of solution into the chamber (this fills the dome to about 2 cm above the O-ring) and shaking it until a uniform opaque foam was created, with an average bubble size much less than the separation of the domes. The chamber was then left to coarsen until a single layer of bubbles remained between the two domes. This took about 24 hours. Two dimensional coarsening could then be observed for the next 2-4 days. Film ruptures were sometimes observed at the end of this period. Bubble statistics were not taken after any ruptures, though single bubble dynamics were still considered.

To photograph the foam, the chamber was placed 65 cm above a Vista Point A lightbox, which provided a spatially and temporally uniform light source. A Nikon D80 camera with a Nikkor AF-S 300 mm 1:2.8 D lens was mounted 2.5 m above the chamber. The camera was controlled by a computer to take pictures every two minutes. The apparatus was left to collect pictures, for a period ranging from a few days up to a week. This process was repeated three times to build up statistics. A sample photograph can be seen in Fig. 4.1. Note in this photograph that, especially towards the edge, it is possible to see both the Plateau borders on the top dome, as well as the Plateau borders on the bottom dome. This makes it difficult to identify the correct boundaries of the cells. We address this issue as part of our image analysis.

After we have taken a series of images of the dome, we perform analysis to get out the true areas of the bubbles on the dome. Note that the images constitute an orthographic projection of a sphere (or hemisphere) onto a plane, where the point of projection is infinity. This projection converts the positions according to the following equations [42]:

$$\begin{aligned} x &= R\cos\varphi\sin\lambda \\ y &= R\sin\varphi \end{aligned} \tag{4.2.1}$$

where $R$ is the radius of the sphere, $\lambda$ is the longitude, $\varphi$ is the latitude, and the center of the domes is defined as $\lambda = 0, \varphi = 0$. The first problem is that in a given image, both the Plateau borders on the top and bottom domes are visible. In order to isolate a set of Plateau borders so that the cells' edges are defined correctly, we

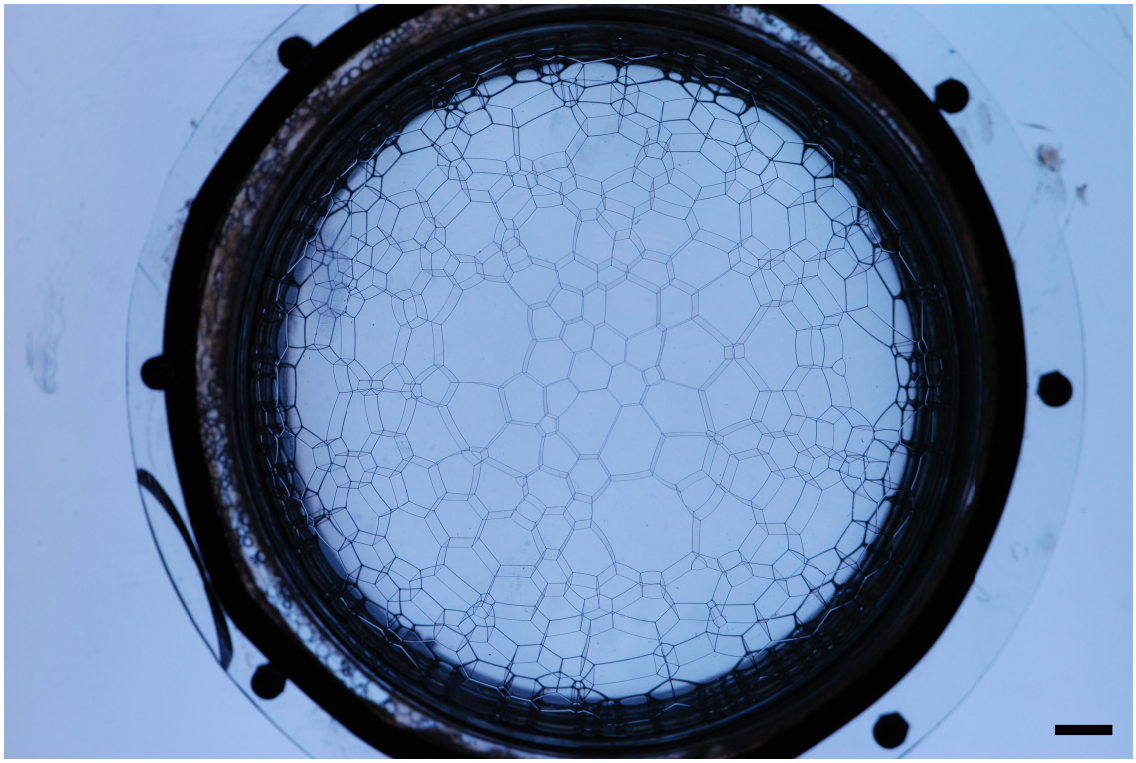

Figure 4.1: Sample photograph of a two dimensional foam, coarsening between nested polycarbonate hemispheres with a 4 mm gap. The scale bar is 1 cm.

recognize that the image is projected in two ways. The Plateau borders on the top dome are an orthographic projection of the foam using the radius of the top dome to do the transformation, and the Plateau borders on the bottom dome are an orthographic projection of the foam using the radius of the bottom dome; both are combined into the same image. To undo this transformation, we take the inverse of the transformation twice, once using the radius for the top dome and once using the radius for the bottom dome. The resulting two images are thresholded and dilated. The images are then multiplied. This kills the Plateau borders that do not correspond to the transformation. That is, the Plateau borders from the bottom dome that were transformed using the radius of the top dome are killed and vice versa. The result is a binary image with the correct latitudes and longitudes of the Plateau borders on the dome.

After we have accounted for the fact that the Plateau borders on both the inner and outer domes are visible, we can then consider the areas of the individual bubbles. The binary image with the correct latitudes and longitudes of the Plateau borders has errors, but does well for a region of interest in the center. This resulting image, however, does not preserve the areas of the cells. A simple projection that will preserve areas is the Lambert cylindrical equal area projection. This projection is defined by [42]:

$$\begin{aligned} x &= R\lambda \\ y &= R\sin\varphi \end{aligned} \tag{4.2.2}$$

where as before $\lambda$ is the longitude and $\varphi$ is the latitude. The $R$ used here is

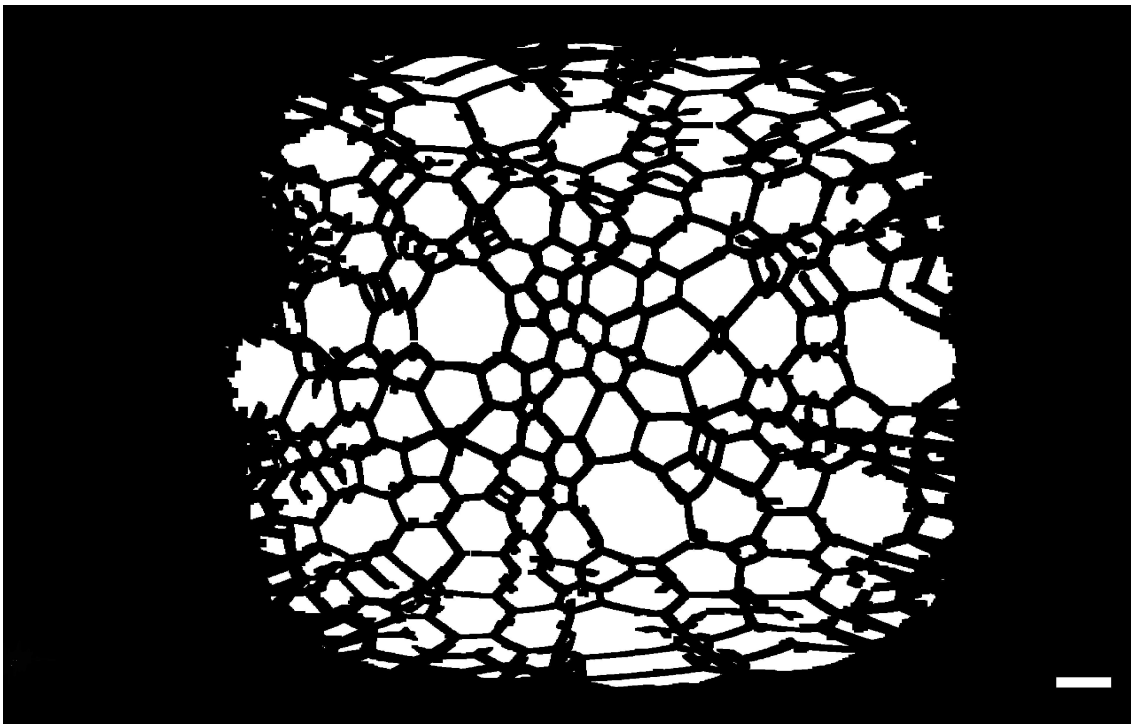

Figure 4.2: Transformation of the photograph in Fig. 4.1 by the Lambert equal area projection to get the true areas of the cells. There are errors in this result, but for a region in the center typically about $4.5 \times 4.5$ cm$^2$ it works well and the areas of these cells can be tracked. This image is skeletonized before any actual areas are measured. The scale bar is 1 cm.

the average of the two domes used. This produces an image with cells that have distorted shapes, but have the same areas as the actual cells on the curved surface. This allows us to track individual bubble areas over time. The result of this image analysis can be seen in Fig. 4.2.

## 4.3 Bubble Dynamics

Using the method of finding the correct areas of individual bubbles described above, it is possible to track the areas of individual bubbles over time. The method of identifying the correct Plateau borders and finding the correct areas sometimes has errors of failing to identify a Plateau border or adding an extra one, especially farther from the center, where distortion is greater. It was possible to find bubbles, especially near the center, that would be correctly identified for a significant length of time. The viewing region where bubbles can be tracked is typically about $4.5 \times 4.5$ cm$^2$. It will not necessarily be possible to track all bubbles in this region, but it is very rare for a bubble outside this region to be trackable. The projections were compared to the original images, to ensure that the areas of the tracked bubbles were correct. Images were taken at 200 minute intervals and analyzed to get the correct bubble areas. Correctly identified bubbles were labeled and tracked over this period. From this it was possible to get area versus time graphs for many bubbles.

We can now consider the form that the area versus time traces for the bubbles

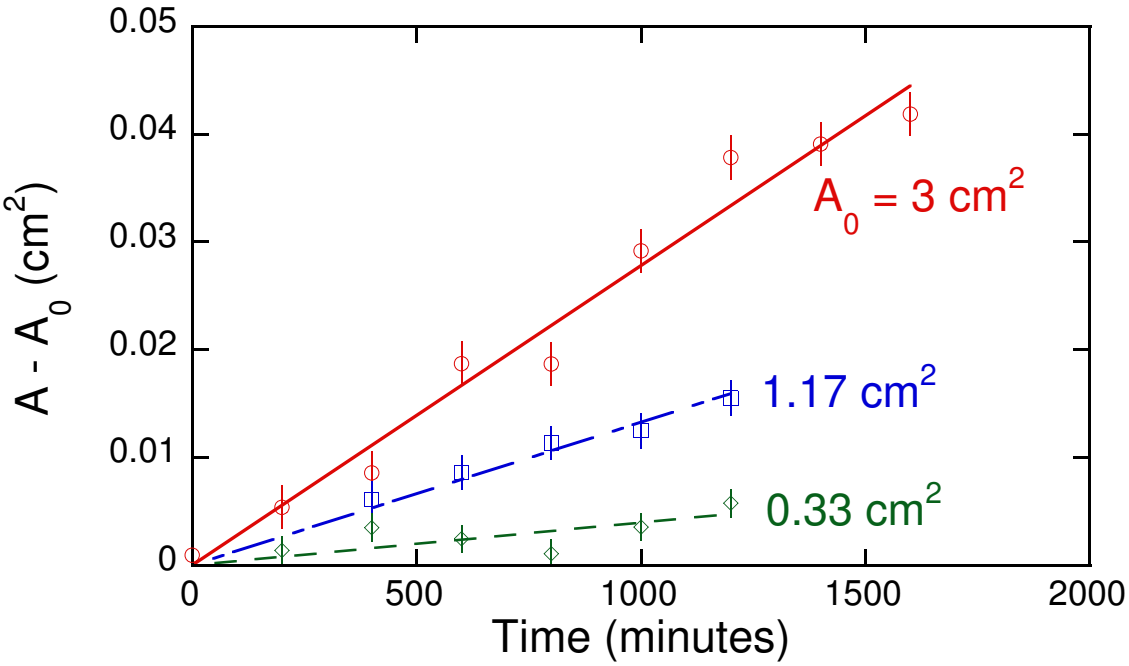


Figure 4.3: Area versus time for three different six-sided bubbles, with initial area, $A_0$, as labeled. Lines are a linear fit to the data, from which $A_0$ was found and subtracted from the data. Vertical error bars represent the perimeter times the pixel size divided by the square root of the number of points in the perimeter; this statistical uncertainty matches the scatter in the data points.

should take. Based on Avron and Levine's correction to von Neumann's law as seen in Eq. (4.1.3), we expect these traces to be exponential. This differential equation can be solved exactly and the result is shown below. Although we can get the exact exponential form of the area versus time curve, the argument of the exponential, $3K_0t/\pi R^2$, is much less than one. This means that the traces are well described using the linear term in the Taylor expansion, resulting in:

$$A = \left[A_o + \frac{\pi R^2}{3}(n-6)\left(1 - e^{-\frac{3K_o t}{\pi R^2}}\right)\right] e^{\frac{3K_o t}{\pi R^2}} \tag{4.3.1}$$

$$= A_o + K_o t\left(n - 6 + \frac{3A_o}{\pi R^2}\right)\left(1 + \frac{3K_o t}{2\pi R^2} + \ldots\right) \tag{4.3.2}$$

Here $A_0$ is the area of a bubble at time 0, and Eq. (4.3.2) is the Taylor expansion in $(K_0t/R^2)$. Note that the standard von Neumann result, $A = A_0 + K_0(n-6)t$, is obtained in the limit $R \to \infty$.

Example data for the area versus time of three six-sided bubbles with different initial areas are plotted in Fig. 4.3. In this plot the initial area of the bubble has been subtracted off so that the traces are easily comparable. The lines are a linear fit to the data, giving a constant growth rate $dA/dt$ that is positive. It is possible to fit the data to the full exponential form of Eq. (4.3.1), but the additional terms in the expansion from Eq. (4.3.2) are much, much smaller than the linear term, so it is sufficient to fit to an ordinary line. The key feature in Fig. 4.3 is that the six-sided bubbles grow, and that the larger ones grow faster. This agrees with Avron and Levine and contrast strongly with the case of a flat-sided cell, where six-sided

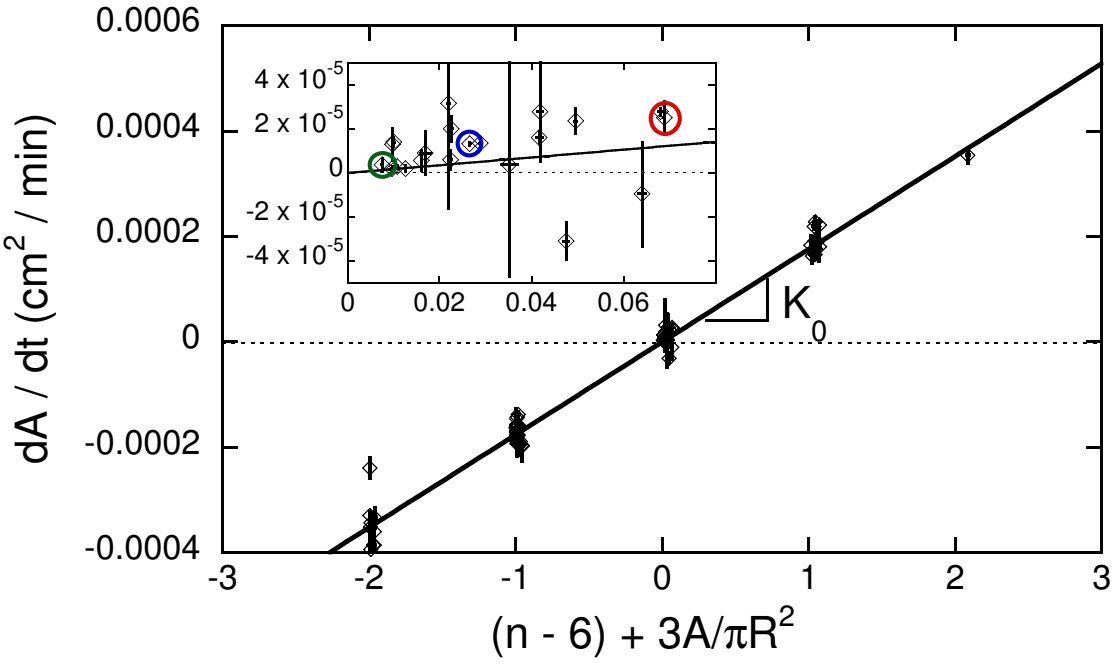


Figure 4.4: Growth rate of the bubble are versus the expected factor from Avron and Levine, Eq.(4.1.3), where $A$ is the bubble area and $R$ is the radius of the dome. Error bars represent the uncertainty in slopes of linear fits to bubble area versus time. The solid line is a proportionality fit to all data, with slope $K_0 = 0.000176 \pm 0.000003$ cm$^2$/min. Inset: Blowup of the data for the $n = 6$-sided bubbles; growth rates for the three representative bubbles in Fig. 4.3 are circled.

bubbles neither grow nor shrink according to the usual von Neumann equation. In particular, in our recent experiments on the coarsening of bubbles in a flat cell [77], where the liquid fraction was varied, the six-sided bubbles all had growth rates scattered around 0 to within statistical uncertainty.

We now measure the growth rate for *all* bubbles, as illustrated in Fig. 4.3, and we compare it to the expected relationship from Avron and Levine's modification to von Neumann's law. This is plotted in Fig. 4.4, where the y-axis is the coarsening rate, and the x-axis is the expected proportionality for a dome of constant curvature, given by Eq. (4.1.3). Each point represents a single bubble. The line

is a proportionality, with slope $K_0$, which is the only fitting parameter. The inset is a blowup showing all the six-sided bubbles and highlighting the three bubbles featured in Fig. 4.3. For six-sided bubbles the growth rates are all positive, except for one or two outliers. There is notable scatter, but the evident trend is that $dA/dt$ increases with bubble size.

Another way to compare growth rate data to Avron and Levine is to plot the coarsening rate against the area, as shown in Fig. 4.5. There each point represents a single bubble, color coded by the number of sides. The horizontal lines are the expected relationship from the unmodified von Neumann's law, as seen in Eq. (4.1.1), using the constant of proportionality $K_0$ as found in Fig. 4.4. The solid lines are the expected relationship from the modified von Neumann's law, as shown in Eq. (4.1.3), again using the same value of $K_0$. We see that the data are generally consistent with the predicted modification. This is most notable in the six sided bubbles, which are virtually all growing. The rate of area change also appears to increase with area for $n = 7$, but is masked by noise for other values of $n$.

## 4.4 Bubble Distributions

With our system it was also possible to measure distributions such as $p(n)$, the probability that a bubble has $n$ sides, and $m(n)$, the average number of sides of the neighbors of an $n$ sided bubble. Unlike the case of the flat cell, we do not expect to

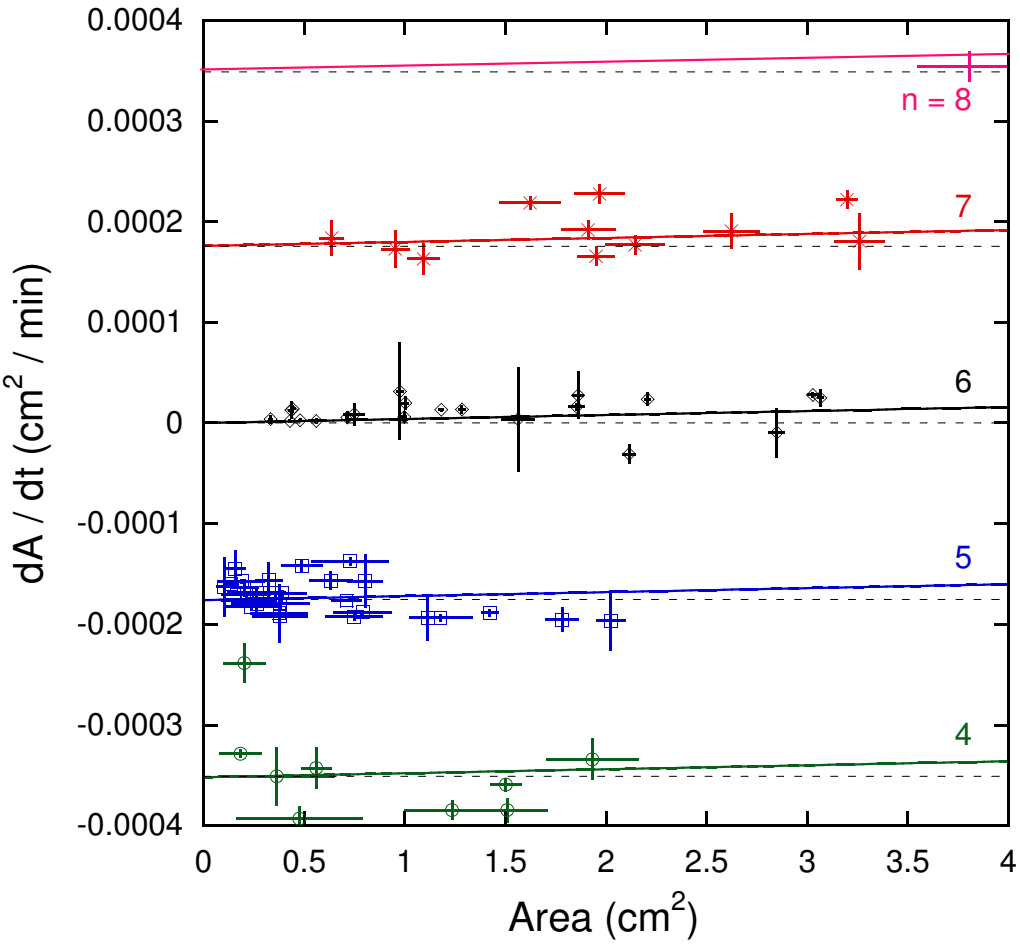


Figure 4.5: Growth rate of bubbles versus area. Symbol types distinguish bubbles with different numbers $n$ of sides, as labeled. Horizontal lines are the expected relationship from the uncorrected von Neumann law, shown in Eq. (4.1.1), using $K_0$ from Fig. 4.4. Solid lines are the expected relationship using the corrected von Neumann law from Avron and Levine, shown in Eq. (4.1.3), using $K_0$ from Fig. 4.4. Data and vertical error bars are the same as shown in Fig. 4.4. Horizontal error bars represent the range of area over which each bubble grew with the specified rate and number of sides.

reach a scaling state where these statistical quantities remain constant over time. Because the growth rate of a bubble grows with its area, we expect at long times to have large bubbles grow rapidly to dominate the system, and this will cause bubble statistics and distributions to change with time. Our system is at much earlier times, where the modification to a bubble's growth rate due to its area is small. This modification still should have some impact and we do indeed find that our statistics deviate from the ordinary scaling state observed in the flat cell.

To measure our statistics, an 8 cm $\times$ 8 cm region of interest was defined in the center of the dome, and the number of sides of all bubbles completely or partially within this region was recorded by hand. This was done for photographs at 400 minute intervals from the earliest photograph of a two dimensional foam to the first occurrence of a rupture, for a total period of typically 48 hours. This was repeated for three runs. These data were used to produce a distribution of the number of sides, which can be seen in Fig. 4.6. Also shown for comparison is the distribution found for a flat two dimensional foam in Ref. [77]. We see that as compared to the flat cell, the dome has a surplus of six sided bubbles, and a deficit of 3, 4, and 5 sided bubbles.

It is also possible to describe these distributions by their average, $\langle n \rangle = 6.06 \pm 0.1$, and by their variance, $\mu_2 = \sum p(n)(n-6)^2$. We measure that $\mu_2 = 1.30 \pm 0.05$. This value is lower than was measured for the flat cell, $\mu_2 = 1.56 \pm 0.02$ [77], indicating that the width of the distribution is narrower.

From this same data we can measure $m(n)$, the average number of sides of the neighbors of an $n$ sided bubble. We expect $m(n)$ to be related to $n$ by the Aboav-Weaire law, which predicts $m(n) = 6 - a + [(6a - \mu_2)/n]$. In this equation $a$ is a fitting parameter which is usually found to be around 1. Our measurements for $m(n)$ can be seen in Fig. 4.7 along with the measurements of $m(n)$ for a flat cell. Fits to the Aboav-Weaire law are also shown, using the relevant value for $\mu_2$ in each case. We find $a = 1.1 \pm 0.08$ for the flat cell and $a = 0.96 \pm 0.09$ for the dome. We see that in both cases there appears to be more curvature in the data than predicted. The data for the flat cell also seems to fit the form better than for the dome.

## 4.5 Conclusion

In this experiment we were able to measure both bubble statistics and bubble dynamics of a foam on a curved two dimensional surface of radius $R$. For bubble statistics we find that bubbles with few sides are under-represented as compared to a two dimensional foam in flat space. We also find that the Aboav-Weaire law generally holds, though not quite as well for the dome as for the flat cell. For bubble growth rates, in general, it is difficult to observe the effect of the term added to von Neumann's law by Avron and Levine to account for substrate curvature. Our maximum bubble size is around $A_{max} = 3.5$ cm$^2$, as compared to $R^2 = 41.6$ cm$^2$, so for all our bubbles $3A/(\pi R^2) \ll |n - 6|$ holds except for $n = 6$. This is why

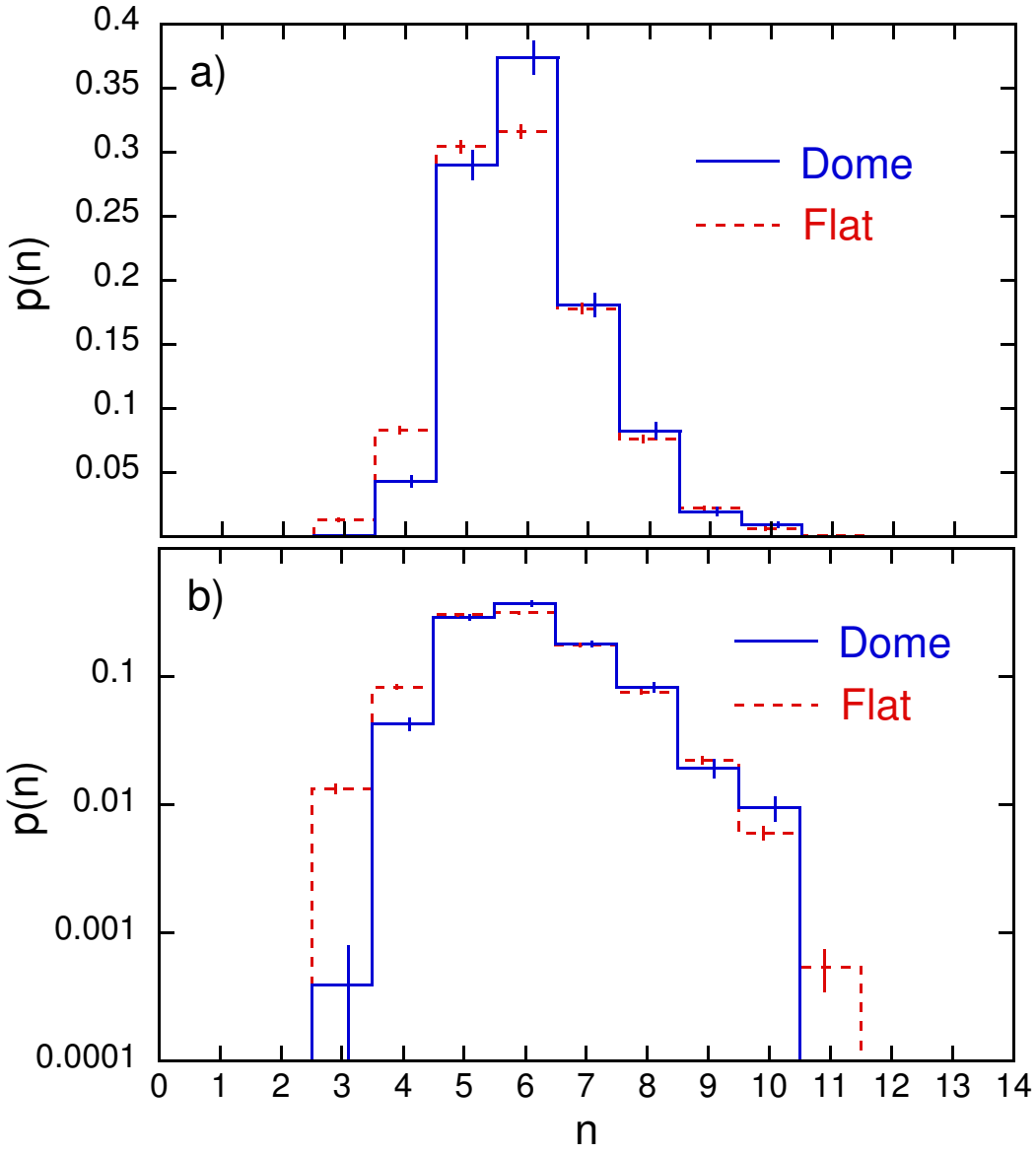


Figure 4.6: Side number distribution for a flat cell and for the dome. For the flat cell, the average number of sides is $\langle n \rangle = 5.92 \pm 0.01$ and the variance $\mu_2 = 1.56 \pm 0.02$. For the dome $\langle n \rangle = 6.06 \pm 0.1$ and $\mu_2 = 1.30 \pm 0.05$. Data for the flat cell are taken from Ref. [77]. Vertical error bars are from a fractional area of 1 over the square root of the number of bubbles with the specified side number.

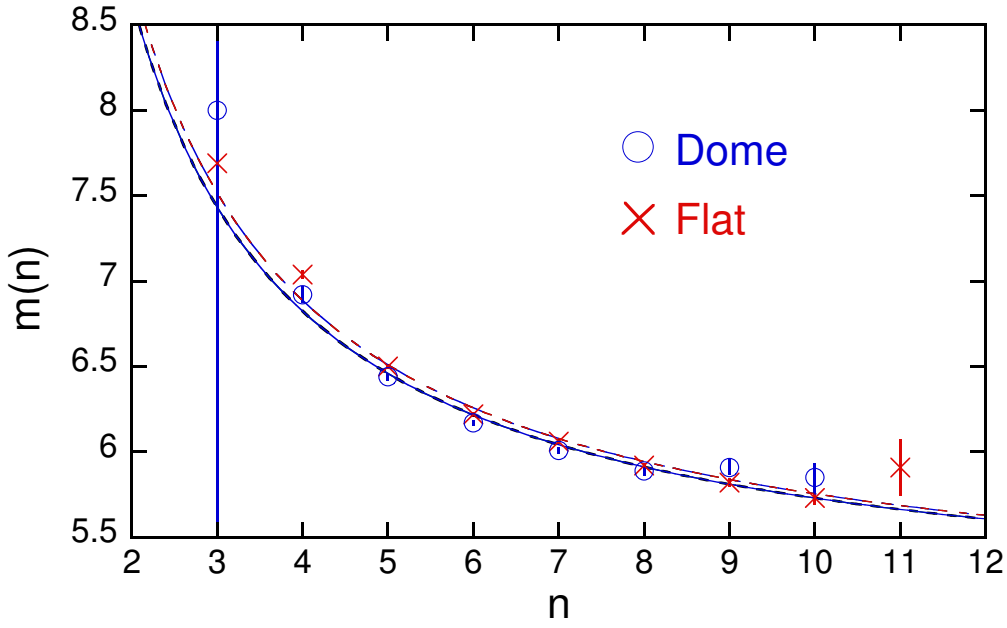


Figure 4.7: Aboav-Weaire relationship for a flat cell and for a dome. The y-axis is $m(n)$, the average number of sides of an $n$ sided bubble. Lines are fits to the Aboav-Weaire law, $m(n) = 6 - a + [(6a - \mu_2)/n]$, where $a$ is the only fitting parameter. We find $a = 1.1 \pm 0.08$ for the flat cell and $a = 0.96 \pm 0.09$ for the dome [77]. The variances, $\mu_2$, for these systems can be found in the caption to Fig. 4.6.

all the data in Fig. 4.4 lie at $x$ values near $(n-6)$. Even if we managed to get a single bubble of 20 cm$^2$ to completely fill our viewing area, the rate of area change would be $\mathrm{d}A/\mathrm{d}t = K_0[(n-6)+0.46]$, so that a seven sided bubble would have less than a 50% increase in growth rate. For this reason the clearest signal we see of this effect is that six sided bubbles grow systematically and do so more rapidly for larger bubbles. The coarsening data as a whole are consistent with Avron and Levine's modification to von Neumann's law to account for coarsening on a curved surface.

## 4.6 Appendix: Details of Image Analysis

To begin, we do as described in the text and convert the image from an orthographic projection to an equirectangular projection using both the radius of the upper and lower dome. We then threshold both images. The threshold value is chosen manually. The same value is used for all images in a single run, although the value may be different between runs. The thresholded images are dilated and multiplied to isolate the correct Plateau borders. The resulting binary image is filtered to remove small particles. The cutoff is much smaller than the smallest bubble. This helps remove particles caused by smudges or dirt on the apparatus or lens. The image is then dilated again and converted to the Lambert equal area projection. The image is then skeletonized. The area of the bubbles are recorded. The number of sides, $n$, of the bubbles are determined by hand.

# Chapter 5

# Structure and Coarsening of the Surface of a 3D Foam

## 5.1 Introduction

The structure and coarsening of three dimensional foams is a topic that has long been of interest [100]. However, characterizing the microstructure in the bulk is difficult task, and generally involves the use of sophisticated techniques beyond direct visual observation [59]. This includes magnetic resonance imaging [32], optical tomography [63, 20], and x-ray tomography [47, 49, 60]. Foam microstructure is further difficult to measure because it changes with time. Even if drainage and film ruptures are prevented, pressure differences between bubbles result in gas dif-

fusion across films, such that some bubbles grow and others shrink. This coarsening process is not limited to foams and is observed in other systems as well [29, 82]. There have been measurements of coarsening in three dimensional foams using light scattering [15, 16, 17], but such measurements involve the average of the system as a whole, and cannot probe the individual bubble level. There have also been measurements using tomography [63, 46] and NMR [32], but these generally involve few bubbles or wet foams. For the case of ideal dry three dimensional foams, there is an exact theoretical solution for the growth rate of an individual bubble with $n$ edges, which takes the form [54]

$$\frac{\mathrm{d}V}{\mathrm{d}t} = K\left(\sum_{i=1}^{n} e_i - 6L\right) \tag{5.1.1}$$

where $K$ is a constant of proportionality, $e_i$ is the length of edge $i$, and $L$ is a quantity called the 'mean length' that depends on the size and shape of the bubble. NMR [32] and tomography [63, 46] have been used to probe coarsening, but contact has not yet been made with Eq (5.1.1).

Much research on coarsening in foams has been done for two dimensional foams, where there is no difficulty in imaging the full microstructure. This includes direct measurements of bubbles compressed between parallel plates [27, 28, 84, 81, 83, 39, 77], soap froths with different boundary conditions [45, 75, 74], and experiments on lipid monolayers [86, 3]. There have also been simulations of two dimensional foams [43, 26, 34, 80, 66, 78, 23]. These foams are simpler not only because of greater ease

of measurement, but also due to simpler geometric considerations. In particular, the coarsening rate of an individual bubble depends only on its number $n$ of sides according to the celebrated von Neumann's law [67]:

$$\frac{\mathrm{d}A}{\mathrm{d}t} = K(n-6) \tag{5.1.2}$$

where $K$ is a constant of proportionality.

The surface of a three dimensional foam is where two and three dimensions meet. When a three dimensional foam is in contact with a flat two dimensional surface, the films meet the surface at an angle of $\pi/2$, and the resulting network of surface Plateau borders meet at 120° at three-fold vertices. [55, 56]. In this way it looks like a two dimensional foam. Here, we are interested in how this 'surface foam' differs from a truly two dimensional foam.

Surface foams have been of previous interest, mostly as a way of connecting to the properties of the larger three dimensional foam. This includes experiments on the radial distribution of very wet foams with nearly spherical bubbles [9, 6, 95], experiments on the surface of continuously bubbled foams [40, 19], work on the effect of liquid fraction [25], and investigation of the optical properties of the surface of a foam [94]. There has also been theoretical work on the conversion of surface measurements to bulk measurements [95, 96, 7], as well as Surface Evolver simulation comparisons of surface and bulk properties for very dry foams [97, 98].

If left to coarsen, both two- and three-dimensional foams are believed to reach a self-similar scaling state where, apart from an overall scale factor, statistical distributions of bubble size, shape, and topology are independent of time. Therefore we expect that surface foams will also reach a scaling state - though with different statistics from a truly two-dimensional foam. In part this is because boundary bubbles coarsen at a different rate than bulk bubbles. In two dimensions, the von Neumann argument can be extended to boundary bubbles by summing the diffusive flux across interior films and using the fact that films terminate at the boundary at right angles [34, 22]. For the case of a flat boundary the result is:

$$\frac{\mathrm{d}A}{\mathrm{d}t} = K(n-5) \tag{5.1.3}$$

Thus, coarsening still only depends on the number of sides, but now 5 sided bubbles instead of shrinking are stationary and 6 sided bubbles grow. We have similarly calculated the growth rate for a three-dimensional bubble in contact with a flat boundary, using the same geometric method of MacPherson and Srolovitz [54]. For a planar boundary we find:

$$\frac{\mathrm{d}V}{\mathrm{d}t} = K\left[\sum_{interior} e_i + \left(\frac{3}{2}\sum_{boundary} e_i\right) - 6L\right] \tag{5.1.4}$$

This is similar to Eq. (5.1.1), but now the contribution from the edge length in contact with the boundary is different from the edge length in the bulk. This describes the growth rate of the entire bubble, and because diffusion can occur in

three dimensions, does not determine the growth rate of the face in contact with the boundary.

Bubble dynamics also include topological changes of the foam. These topological changes come in two types: T1 processes, which do not change the total number of bubbles, and T2 processes, which involve the creation or disappearance of a bubble. In both surface foams and two dimensional foams, T1 processes and the subset of T2 processes that involve the disappearance of a bubble will look the same. However, in two dimensional foams, the creation of a bubble is not possible. In surface foams, the movement of a bulk bubble to the surface will result in the creation of a bubble.

In general it is difficult to examine the surface of a three dimensional dry foam because the Plateau borders in contact with the surface are not the only ones visible. It is also possible to see all the interior Plateau borders, and properly distinguishing the only those at the surface is difficult. We have developed a novel imaging technique based on total internal reflection that allows us to isolate the surface of a three dimensional foam. From these nice images, we use image analysis to measure the properties of individual bubbles. We can also track individual bubbles over time.

Because the surface foam obeys Plateau's laws, we use the techniques developed to describe two dimensional foams to describe these surface foams. We also characterize the scaling state of a surface foam and compare this to the scaling state reached by two dimensional foams. We measure dynamics of the surface foam,

including growth rates of individual bubbles.

## 5.2 Materials and Methods

Our apparatus can be seen in Fig. 5.1. Our foam sample is inside a plastic bottle with a square cross section of 9 cm $\times$ 9 cm and a height of 14 cm. All areas of the bottle were masked with electrical tape except for a single flat surface of interest. This bottle was completely submerged in a tank of water. A Vista Point A lightbox was placed to the side of the square tank and provided steady, uniform illumination. A Nikon D80 camera with an AF-S Nikkor 55-200 mm 1.4-5.6G ED lens was pointed at the face of the tank 90° from the lightbox. The bottle was placed so that the surface of interest was at an angle relative to the lightbox and the camera.

To create our foam, we used a solution consisting of 75% deionized water, 20% glycerin, and 5% Dawn ultra concentrated dish detergent. The resulting foam was stable and long lived. Film ruptures were not observed in the course of our experiment. To create our sample, 275 mL of this solution was put into our bottle, which was then sealed and vigorously shaken until the bottle was filled with a uniform opaque foam of sub-millimeter bubbles. This foam was left for two hours, during which time it drained and coarsened into a dry, three dimensional foam, ready for imaging.

Our setup allows us to utilize a novel imaging method to isolate the surface of

the foam. Because the bottle is completely submerged underwater, light from the lightbox can be totally internally reflected. The angle of the bottle is chosen so that if the light reaches a point on the surface of the bottle that has the interior of an air bubble on the other side, it will be totally internally reflected. If the light reaches a Plateau border, there will not be reflection, and the light will be scattered. This results in an image that has bright cells and dark Plateau borders. A sample raw image can be seen in Fig. 5.2a. Because this method is based on reflection, only the surface of the foam in contact with the boundary is imaged. This technique eliminates the problems of distinguishing internal Plateau borders from surface Plateau borders.

Note that the raw image in Fig. 5.2a is distorted, since the bottle is at an angle, and this must be corrected. Fiducial marks were made at the corners to define a rectangular region with right angle corners. Using the position of these marks, it was possible to transform the image to a direct perspective. A sample image of the surface foam after this transformation can be seen in Fig. 5.2b. After this was done, image analysis and thresholding and skeletonization were performed to identify the cells, separated by skeletonized borders. The results of this image analysis can be seen in Fig. 5.2c. From these images it was possible to extract relevant quantities for the individual bubbles, such as area and number of sides. Only bubbles completely within a region of interest that excluded edge bubbles were considered.

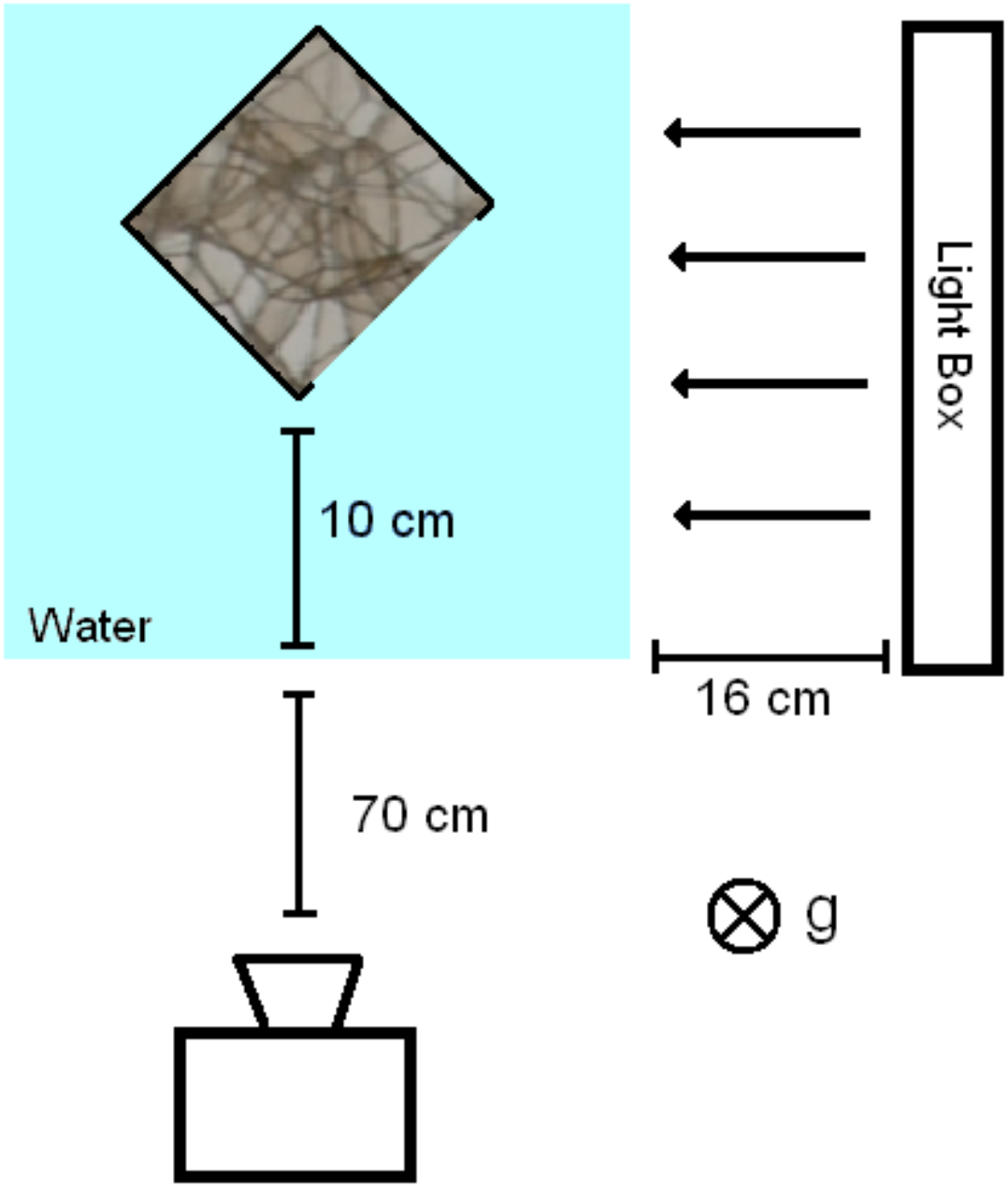


Figure 5.1: A schematic diagram of a top down view of the imaging setup. The square bottle in the center is filled with foam and submerged in a tank of water. On the right of the diagram is a lightbox that provides constant uniform illumination. At the bottom of the diagram is a camera to image the surface of interest. Not to scale.

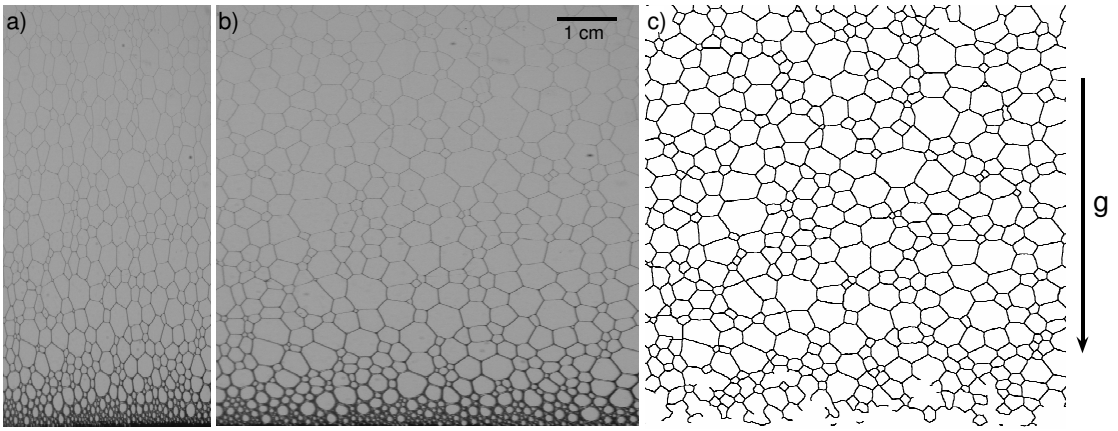


Figure 5.2: Part a) shows a raw image of the region of interest of the surface foam. Part b) shows an image of the surface foam after it has been transformed to correct for distortion from the angle of the bottle and perspective. Part c) shows the reconstructed borders of the foam.

## 5.3 Bubble Distributions

### 5.3.1 Bubble Side Distributions

The first relevant quantity to consider for a foam is the distribution of the number of sides, $p(n)$. This is the probability that a randomly selected bubble from the foam will have $n$ sides. The probabilities for four different $n$, for an individual run, are shown versus time in Fig. 5.3. Here we see that there does not appear to be any systematic change in the probabilities over time. This is consistent with the foam being in a scaling state. Immediately after shaking our foam begins with surface bubbles that are typically about 0.5 mm in diameter. By the time the foam has coarsened for two hours when data taking begins, the average surface bubble diameter has increased by a factor of 10, so it is not surprising that the foam is in a scaling state from the earliest times we consider.

The distribution of number of sides is also the same for the 4 different runs. This allows us to average the distribution, $p(n)$, over all times and for all runs. The overall number of sides distribution is shown in Fig. 5.4a. Also shown for comparison is the number of sides distribution for an ordinary two dimensional foam. We see that there is a difference in the distributions. Even though the surface foam obeys Plateau's laws and looks in that way like a two dimensional foam, the different dynamics lead to a different scaling state. We see that the distribution for the surface foam is broader, with fewer five and six sided bubbles and more four sided bubbles. This means that the surface foam has a higher variance, $\mu_2 = \langle (n - \langle n \rangle)^2 \rangle$, which we measure to be $\mu_2 = 1.99 \pm 0.04$, as compared to the value measured for the two dimensional foam, $\mu_2 = 1.56 \pm 0.02$.

A related distribution that is less common is the area weighted number of sides distribution, $F(n)$. This quantity is defined in Ref. [77] as the probability that a randomly selected point within the foam will fall inside an $n$ sided bubble. When calculating the growth rate of the average area for a two dimensional foam, the rate depends on the quantity $\sum_n nF(n)$. As with $p(n)$, this distribution does not vary with time, and so we can average over all times for all runs, and the results are shown in Fig. 5.4b. Also shown for comparison is the distribution of $F(n)$ for an ordinary two dimensional foam. This distribution is not as clearly distinct from the ordinary two dimensional case as for $p(n)$.

We can also look at another quantity that has been of interest, $m(n)$, the average

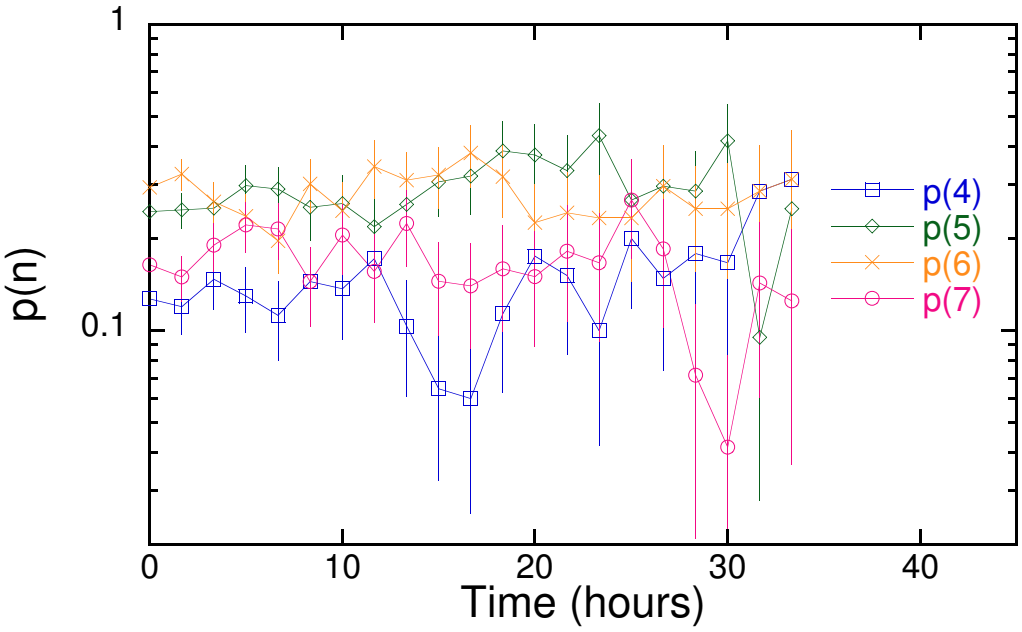


Figure 5.3: Side number distribution, $p(n)$, versus time for 4, 5, 6, and 7 sided bubbles for a single run.

number of sides of an $n$ sided bubble. As with the side number distribution, this quantity does not change over time or for the different runs. This allows us to average over all $n$ sided bubbles for all times and for all runs. The results are shown in Fig. 5.4c. There is a theoretical prediction for the shape of this relationship, known as the Aboav-Weaire law. This law takes the form $m(n) = (6 - a) + (6a + \mu_2)/n$, where $\mu_2$ is the variance, and $a$ is the only fitting parameter. We find $a = 1.16 \pm 0.07$, which is within error of measurements for ordinary two dimensional foams [8, 100, 77].

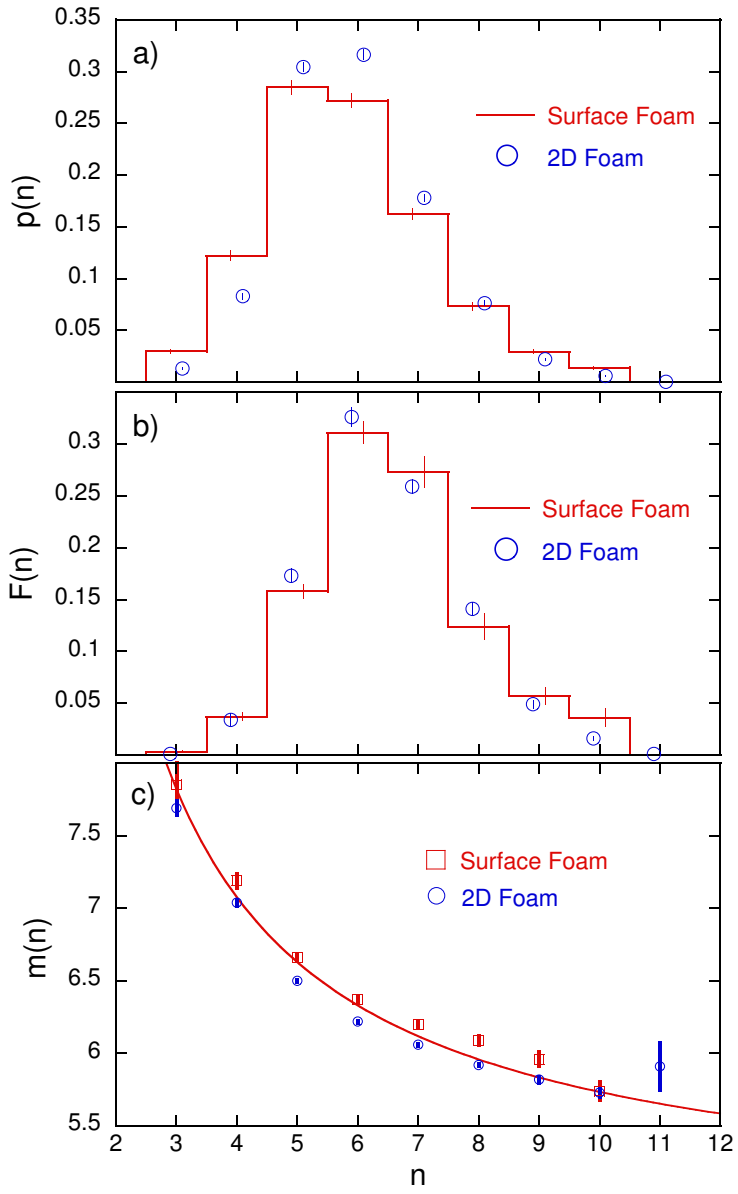


Figure 5.4: a) Side number distribution, $p(n)$, averaged over all times for all runs. Bubbles with $n < 3$ or $n > 10$ were not observed. Total number of bubbles is 5966. Average number of sides is $\langle n \rangle = 5.83 \pm 0.02$. Data for the two dimensional foam is taken from Ref. [77]. b) Area weighted side number distribution, $F(n)$, averaged over all time for all runs. Area weighted average number of sides is $\langle\langle n \rangle\rangle = 6.6 \pm 0.2$ Data for the two dimensional foam is taken from Ref. [77]. c) $m(n)$ is the average number of sides of the neighbors of an n sided bubble. The data is averaged over all times for all runs. The solid curve is the Aboav-Weaire law, $m(n) = (6 - a) + (6a + \mu_2)/n$, where $\mu_2$ is the variance, $\langle (n - \langle n \rangle)^2 \rangle$, of the side distribution (for our system $\mu_2 = 1.99 \pm 0.04$) and $a$ is the only fitting parameter, which we measure to be $a = 1.16 \pm 0.07$. Data for the two dimensional foam is taken from Ref. [77].

### 5.3.2 Bubble Size Distributions

We also measure the area of each bubble, another basic quantity. Especially of interest is the distribution of bubble areas for the foam. Although the average area of the bubbles increases with time, if we divide out the average area, the distribution of the resulting normalized area does not change with time, and is the same for all runs. This is consistent with the foam being in a scaling state. Therefore it is possible to average the normalized area distribution for all times and for all runs. The cumulative distribution of bubble areas is shown in Fig. 5.5a. The curve corresponding to an exponential distribution is shown for comparison as a dotted line. We see that our data falls below the exponential curve for large $A/\langle A\rangle$. Our data is better fit by a compressed exponential, which is shown as a dotted line. We see that the cumulative area distribution for the surface foam is largely similar to the distribution for a two dimensional foam, but falls above the two dimensional data for large $A/\langle A\rangle$, although this deviation is within the error bars.

As with the area, we measure the perimeter of each bubble. We average the normalized perimeter across all times and runs. The cumulative distribution of perimeters can be seen in Fig. 5.5b. The normalized perimeter falls below the exponential curve, and is well fit by a compressed exponential. The compressed exponential shown for the perimeter distribution corresponds to the compressed exponential for the area distribution, assuming that $A \propto P^2$ with the same proportionality constant for all bubbles. This form is the same as equations 7 and 8 in

Ref. [77]. We see that the perimeter distribution for the surface foam falls on top of the distribution for a two dimensional foam and does not show the deviation for large bubbles seen in the area distribution.

### 5.3.3 Size-Topology

We have characterized the distribution of the number of sides and the area distribution, but it is also useful to look at quantities that depend on both these measurements in different ways. One example is the average area of an $n$ sided bubble. This is a relationship that has been of interest in the past [8]. The first empirical measurements were made by Lewis for epithelial cucumber cells, who found a linear relationship of the form

$$\frac{\langle A_n \rangle}{\langle A \rangle} = 1 + \lambda(n-6) \tag{5.3.1}$$

where $\lambda$ is a parameter of the system [51, 52]. It can be shown that if $\langle A_n \rangle / \langle A \rangle$ is linear in $n$ then this relationship must hold, but additional restraints are required to prove that this relationship must be linear [73]. A related measurement that is also of interest is the relationship between the average perimeter of an $n$ sided bubble and $n$. This analogous relationship is called Desch's law or Feltham's law, and is of the same form as Lewis' law with the area replaced by perimeter. Specifically, it has the form

$$\frac{\langle P_n \rangle}{\langle P \rangle} = 1 + \nu(n-6) \tag{5.3.2}$$

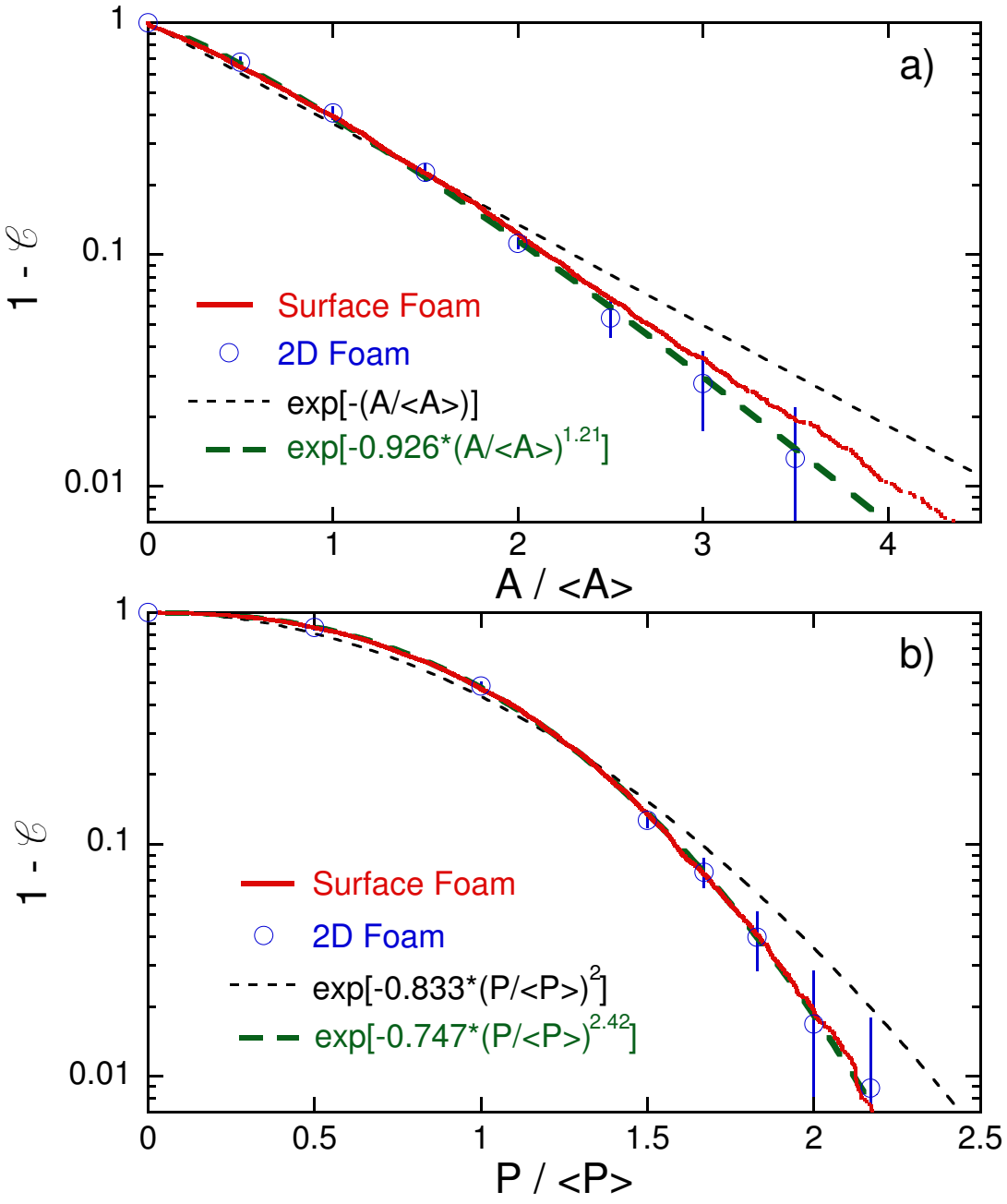


Figure 5.5: a) Area distribution averaged over all times for all runs. b) Perimeter distribution averaged over all times for all runs. The y-axis, $1 - CDF$ (CDF is the cumulative distribution function), is the fraction of bubbles with normalized area greater than the x value. Dotted black line is an exponential shown for comparison. Green dashed curve is fit to a compressed exponential. The compressed exponential in part b) corresponds to the form in part a), assuming that $A \propto P^2$ with the same proportionality constant for all bubbles. Data for the two dimensional foam is taken from Ref. [77].

where $\nu$ is a parameter of the system. It has been shown that if the average energy of a cell is proportional to its perimeter, then the entropy is maximized if Desch's law is satisfied [72]. These laws continue to be of interest [88, 79, 14].

We measured $A/\langle A\rangle$ for all bubbles and the results, for all times and all runs, are shown versus side number in Fig. 5.6a. The grayscale corresponds to the probability of finding a bubble with that number of sides and that normalized area for each point. The average, $\langle A_n\rangle/\langle A\rangle$, is shown as squares. Note that the distribution of normalized areas around the average for a given $n$ is not symmetric and, especially for small $n$, is peaked near zero. A fit to Lewis' law is shown as a solid line, and does not match the data closely. This demonstrates that Lewis' law is not an appropriate fit for our data, which is fit better by a generic quadratic form, shown on the plot as a dotted line. This result is in accordance with some simulations and experiments on ordinary two dimensional foams [88, 14, 77]. We see that the values for the surface foam are not significantly different from the two dimensional foam, although it looks as though the two dimensional data may have slightly more curvature. Both cases clearly deviate from Lewis' law. This deviation from Lewis' law is consistent with our result that the area distribution deviates from an exponential [48].

We similarly measured the normalized perimeters, $P/\langle P\rangle$, for all bubbles, and the results for all times and runs are shown in Fig. 5.6b. As in the plot for Lewis' law, the grayscale corresponds to the probability of finding a bubble with a given number of sides, $n$, and a given normalized perimeter. The average for each $n$,

$\langle P_n \rangle / \langle P \rangle$, is shown as squares on the plot. Note that the distributions about the average are much more symmetrical than in the area case shown in Fig. 5.6a. The fit to Desch's law, shown as a solid line on the plot, is a good fit to the data. Desch's law is a better fit to our data than Lewis's law. We see that the surface foam data, while clearly linear, as is the data for the two dimensional foam. However, the slopes of the lines in the two cases are different. The value of $\nu$ measured for the surface foam in the fit to Eq. (5.3.2) is $\nu = 0.21 \pm 0.01$. This value is in the same general range as measurements made for ordinary two dimensional foams [88, 14, 77].

### 5.3.4 Bubble Shape Distributions

There are many ways to characterize the shape of a bubble. Among the possible shape parameters, there are two that have special physical significance with regards to the coarsening process of wet two dimensional foams [77]. The first is circularity, defined as

$$C = \left( \frac{1}{n} \sum_{i}^{n} 1/R_i \right) \sqrt{A/\pi}, \tag{5.3.3}$$

where $A$ is the area and $R_i$ is the radius of curvature for the $i^{th}$ side of an $n$-sided bubble. The sign convention is such that $R_i$ is positive for the bubble on the high-pressure side of the film. This dimensionless number is 1 for a circle and 0 for any shape made up of straight line segments. Note that the surface Plateau borders must be circular arcs for $C$ to be well defined, which in turn requires the curvature of the films perpendicular to the surface to be constant. While the films must certainly

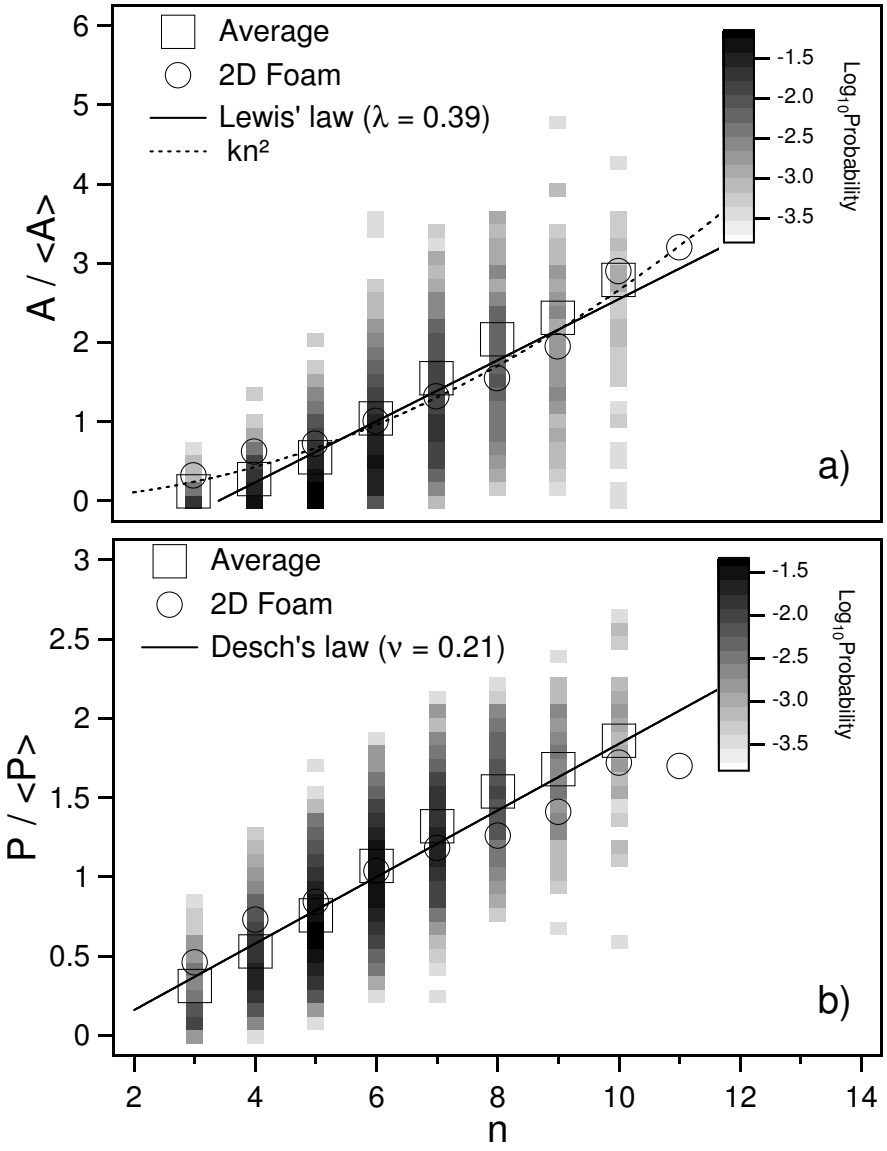


Figure 5.6: a) Normalized area versus side number for all bubbles. Grayscale shows the probability of finding a bubble with that side number and that area. Squares are the average normalized area for a given $n$, $\langle A_n\rangle/\langle A\rangle$. Solid line is a fit to Lewis' law, $\langle A_n\rangle/\langle A\rangle = n\lambda + (1-6\lambda)$. The fitted value is $\lambda = 0.39 \pm 0.03$. Dotted line is a fit to the proportionality $\langle A_n\rangle/\langle A\rangle = kn^2$. Data for the two dimensional foam is taken from Ref. [77]. b) Normalized perimeter versus side number for all bubbles. Grayscale shows the probability of finding a bubble with that side number and that perimeter. Squares are the average normalized perimeter for a given $n$, $\langle P_n\rangle/\langle P\rangle$. Solid line is a fit to Desch's law, $\langle P_n\rangle/\langle P\rangle = n\nu + (1-6\nu)$. The fitted value is $\nu = 0.21 \pm 0.01$. Data for the two dimensional foam is taken from Ref. [77].

meet the boundary at $\pi/2$ it is not obvious that the curvature condition holds. However, as a practical matter we find no obvious deviation of surface Plateau borders from perfect circular arcs. The second is elongation, defined as

$$P/\sqrt{4\pi A} \tag{5.3.4}$$

where $P$ is the perimeter and $A$ is the area. This dimensionless number is 1 for a circle, and a large elongation would correspond to a shape far from a circle.

The distribution of circularities for all times and for all runs is shown in Fig. 5.7. The grayscale corresponds to the probability of finding a bubble with that circularity and that number of sides. The average circularity for each $n$ is shown as squares. For comparison, the circularity of an isotropic bubble is shown as a straight line. An isotropic bubble is an $n$ sided bubble with all sides the same length and having the same curvature. We see that the circularity for two dimensional foams and surface foams is very similar. Both are similar to the isotropic case, except for three sided bubbles, which fall below the line.

The distribution of elongations, for all times and for all runs, is shown in Fig. 5.8. The grayscale corresponds to the probability of finding a bubble with that elongation and that number of sides. The average elongation for each $n$ is shown as squares. This average elongation does not depend on $n$. For comparison, the elongation of an isotropic bubble is shown as a dashed line. We see that, unlike the circularity, the values for isotropic bubbles are not close to the average value. The overall shape

of the distribution is of a large peak, with a long tail and small secondary peak (note that the probabilities are shown on a logarithmic scale). This long tail and secondary peak increases the average elongation, but the mode, shown as circles on the plot, show that the distribution is peaked near the value for an isotropic bubble. Ordinary two dimensional foams have a distribution of elongations that is much less broad. There is no tail of highly elongated bubbles. We see that this tail for surface bubbles causes the average value to be far from the peak of the distribution. Although the average elongation for the surface foam and the two dimensional foam are far apart, the average of the surface foam is close to the peak of the distribution for the surface foam. This suggests that most surface bubbles have an elongation in a range similar to what we see for two dimensional foams, but in surface foams there exists a tail of highly elongated bubbles not present in ordinary two dimensional foams. The fact that the elongation distribution is different for the surface foam and the two dimensional foam is consistent with the fact that the area distribution for the surface foam deviates from the area distribution for the two dimensional foam, but the perimeter distributions are the same in both cases.

## 5.4 Bubble Dynamics

All measurements discussed to this point have involved individual static photographs and have not considered how the bubbles are changing over time. An initial clear signal that the dynamics are different in the case of the surface foam is the creation

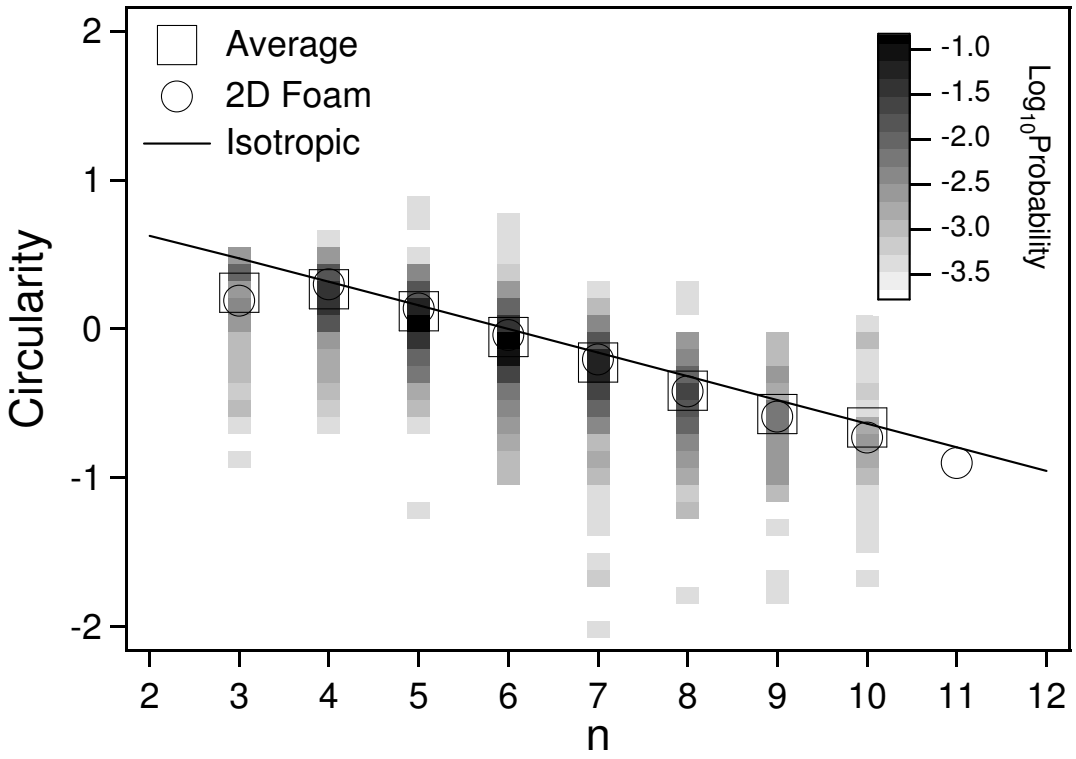


Figure 5.7: Circularity versus side number for all bubbles. Circularity is defined by Eq. (5.3.3). Grayscale shows the probability of finding a bubble with that side number and that circularity. Squares are the average circularity for a given $n$. The solid line shows the circularity for isotropic bubbles. Data for the two dimensional foam is taken from Ref. [77].

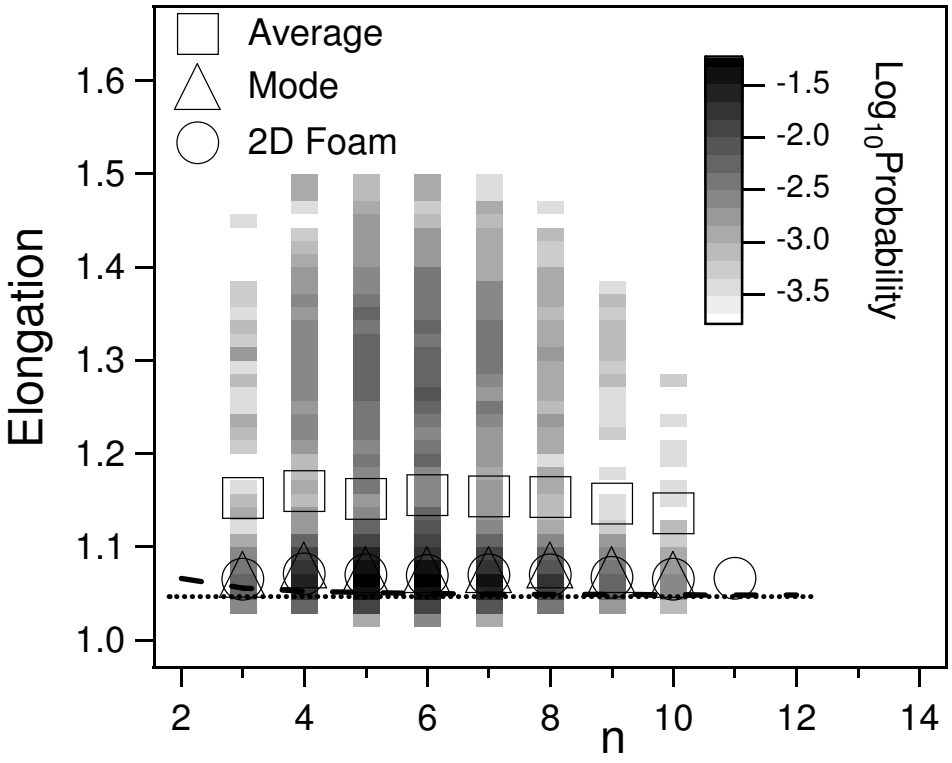


Figure 5.8: Elongation versus side number for all bubbles. Elongation is defined as $P/\sqrt{4\pi A}$, where $P$ is perimeter and $A$ is area, with circularity normalized so that the sum over $n$ and integral over elongation gives 1. Grayscale shows the probability of finding a bubble with that side number and that elongation. Squares are the average elongation for a given $n$. The dashed line shows the elongation for an isotropic bubble with $n$ sides. The dotted line is the limit of the elongation of an isotropic $n$ sided bubble as $n$ goes to infinity. The triangles are the mode of the circularity for a given $n$. Data for the two dimensional foam is taken from Ref. [77].

of bubbles. This type of T2 process is not possible in two dimensional foams, but in our surface foam we do observe the creation of bubbles, which can happen when bulk bubbles move to the surface. The creation of bubbles occurred at a much lower frequency than the disappearance of bubbles.

We are also able to track individual bubbles over time, and can measure how bubble quantities change. In a sequence of 30 images, it is possible for us to measure the area of a bubble at each time, and fit these curves to a line for each bubble. Only bubbles that did not change $n$ during this window were considered, so topological changes were not an issue. The slope of the line is $\mathrm{d}A/\mathrm{d}t$. For area versus time curves that were not linear, each linear region was considered separately. In this way we can measure the coarsening rate of a large number of bubbles. In a two dimensional foam, the coarsening rate of an individual bubble depends only on the number of sides of that bubble, a surprising result known as von Neumann's law, shown in Eq. (5.1.2). In the case of our surface foam, we are only seeing the individual faces of larger three dimensional bubbles, which can exchange gas through diffusion not just with the bubbles we can see, but others in the bulk. The exact equation for the growth rate of a three dimensional boundary bubble is shown in Eq. (5.1.4). Additionally, the growth or shrinkage of bubble volume does not necessarily correspond to the area change of a single film. The von Neumann argument for two dimensional foams thus cannot be applied and the coarsening rate of the two dimensional surface bubbles will not be expected to depend only on the number of sides. We expect that in three dimensions larger bubbles and bubbles

with more faces will be more likely to grow, so we expect some correlation between number of sides and area and coarsening rate.

In Fig. 5.9 we plot area versus time curves for four different six sided bubbles. In two dimensions, all six sided bubbles are stationary and neither grow nor shrink. In the case of surface bubbles we see that six sided bubbles have a wide variety of coarsening rates, including bubbles growing at a rate comparable to the average rate for seven sided bubbles, and bubbles shrinking at a rate comparable to the average growth rate for five sided bubbles. These area versus time curves are also not linear, even though there are no topological changes during this time window.

The coarsening rate, $\mathrm{d}A/\mathrm{d}t$, for individual bubbles is plotted against number of sides in Fig. 5.10a. In this we see that there is a large scatter for coarsening rates of bubbles with the same number of sides, and a large overlap of bubbles with different numbers of sides having the same coarsening rates. This is very different from coarsening in a two dimensional foam, shown in Fig. 5.10b. For a two dimensional foam, growth rates are tightly clustered around the average.

For the case of the surface foam, we expect the coarsening to be very complicated, with gas diffusion possible between surface bubbles and bubbles in the bulk, as well as a limited correlation between the change in bubble volume and the change in area of a single face on the surface. Indeed, we see a wide range of growth rates in the case of the surface foam. However, despite this wide variation for individual bubbles, we see that on average bubbles with more sides grow faster. Remarkably,

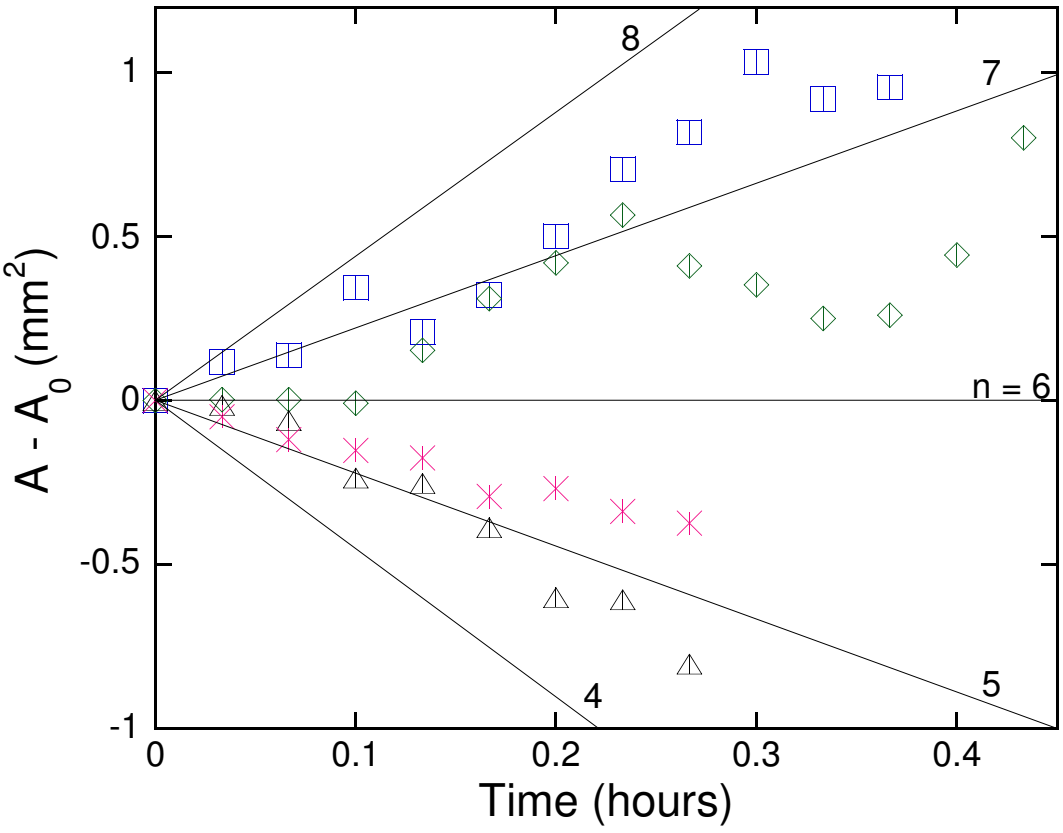


Figure 5.9: Area versus time curves for four different six sided bubbles. Initial area is subtracted off for ease of comparison. Solid lines represent the average growth rates of $n$ sided bubbles.

the average coarsening rate of $n$ sided bubbles follows a proportionality like von Neumann's law. We measure a constant of proportionality of $2.2 \pm 0.1$ mm$^2$/hour.

## 5.5 Conclusion

We measured distributions and dynamics of the two dimensional surface of a three dimensional foam. A technique involving submerging the apparatus in water allowed us to cleanly image the surface, and image analysis allowed us to process a large

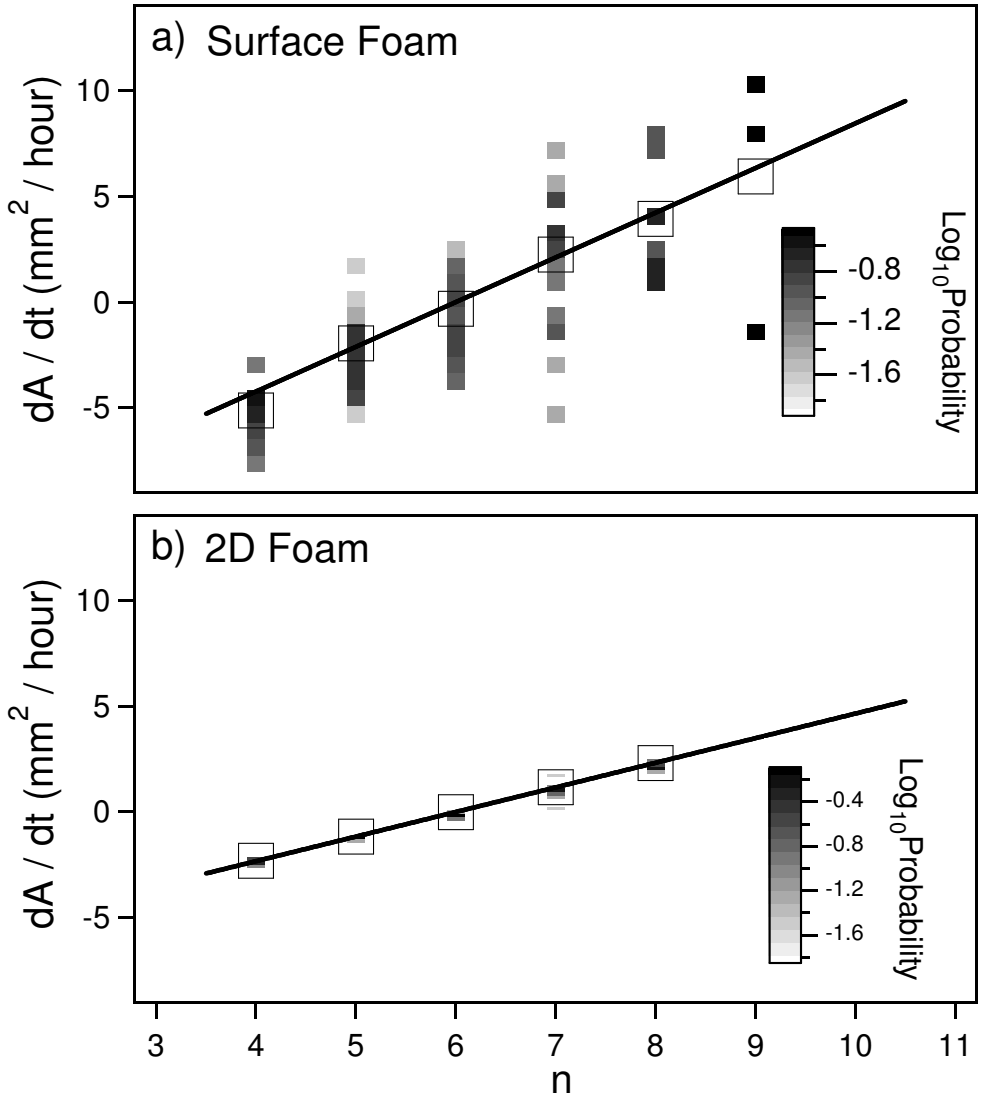


Figure 5.10: Rate of change of area versus side number for all tracked bubbles. Greyscale shows the probability of an $n$ sided bubble having that coarsening rate. Squares are the average rate of change of area for a given $n$. Line is a fit to the proportionality $\langle \mathrm{d}A_n/\mathrm{d}t \rangle = K(n-6)$. Part a) shows the relationship for the surface foam. For the surface foam we measure $K = 2.2 \pm 0.1$ mm$^2$/hour. Part b) shows data for the vertical two dimensional foam from Ref. [77]. For the vertical two dimensional foam we measure $K = 1.20 \pm 0.06$ mm$^2$/hour

quantity of data and build good statistics.

Some measurements were very similar to the case for an ordinary two dimensional foam. The number of sides distribution for the surface foam was slightly broader than for the two dimensional case, but other topological measurements, such as $F(n)$ and $m(n)$, were nearly indistinguishable. Likewise, the size distributions were very close in both cases. There was a slight difference in the area distribution for large $A/\langle A\rangle$, and the perimeter distribution was the same in both cases. The measurement of the shape parameter circularity was also the same for the surface foam and the two dimensional foam.

The distribution of another shape parameter, elongation, was noticeably different in the surface foam. Unlike the two dimensional foam, for the surface foam there was a tail of large elongation bubbles. This resulted in the average elongation being different for the two cases, although the distributions were peaked near the same value.

The greatest difference between the surface foam and the two dimensional foam was in the dynamics. Unlike the two dimensional foam, which obeys von Neumann's law, the surface foam had individual bubbles that coarsened at a wide variety of rates. Additionally, we observed the creation of bubbles, a topological change that is not possible for two dimensional foams. Despite the spread in growth rates for the surface foam, von Neumann's law held on average. This surprising result remains to be explained.

## 5.6 Appendix: Details of Image Analysis

The raw images collected in this experiment, while nicely isolating the surface, are much lower contrast and noisier than for the standard two dimensional case. This requires some initial processing before the images can be plugged into the kind of programs used for the standard two dimensional foams. First we look at the separate red, blue, and green channels. We saw that the red channel was much worse than either the green or blue channels, which were similar in quality. We discard the red channel. We then operate on the green and blue channels in parallel. The noise in these channels is largely uncorrelated, so by operating on these channels separately, then recombining them, we can eliminate most of this noise. We begin with a low pass filter. We then run an edge finding algorithm and threshold the images. The threshold is chosen manually. The threshold is kept the same for all images in a single run, but may vary between runs. We then dilate the thresholded image and correct for the perspective distortion as described in the next appendix. We then skeletonize the image and filter out very small particles. This gets rid of particles caused by smudges or dust on the bottle, tank, or lens. We then skeletonize the image again, dilate and multiply the resulting images for both the blue and green channels. We skeletonize again to get a result that nicely identifies the bubbles. We then label each bubble so that the pixels of each bubble all share a unique pixel value. Due to the skeletonization process, the boundary pixels touch exactly two other boundary pixels, except for the vertices, which touch three. In this way we can

identify the vertices. We then identify the three bubbles that each vertex touches, and can rearrange this to see how many vertices each bubble has. This is the same as $n$, the number of sides. We can get other information about the bubbles, such as centroid position, area (just the number of pixels inside the bubble) and perimeter (not just the number of edge pixels, but includes smoothing at the pixel level by a built in LabVIEW algorithm).

In order to calculate the circularity, we fit the edges of each bubble to circles. To do this, for every pair of bubbles we identify the edge between them by looking at the boundary pixels that touch those two bubbles. We then take the two vertices that correspond to that edge and the average of the three middle pixels. These three points define a circle. The radius of this circle can be calculate for each edge, and the circularity can be calculated in that way.

## 5.7 Appendix: Correction of Perspective

In the raw images we collected, the bottle is turned at an angle to the camera. We must undo this distortion in order to correctly evaluate the areas and other statistics of the bubbles. To aid in this, we made four fiducial marks that defined the corners of a square on the flat face. Knowing that these marks defined the corners of a square allowed us to determine the angle of the bottle and undo the perspective distortion. If we define $x$ and $y$ as the co-ordinates in the plane of the photograph,

and $z$ as pointing into the photograph, our fiducial marks give us four ordered pairs, $(x_i, y_i)$, where $i$ runs from 1 to 4, numbering the points counterclockwise beginning with the upper left point. We will also consider $(x_c, y_c)$, the center point of the photograph. The bottle is arranged so that the left side of the bottle is nearest to the camera.

The first step is to determine $w$, the width of the square. Because it is a square we can just use the length of the (undistorted) left vertical side. This is just

$$w = \left[(x_1 - x_2)^2 + (y_1 - y_2)^2\right]^{1/2} \tag{5.7.1}$$

We know that the apparent distance between the left and right vertical sides in our photograph is $w \cos\theta$, so we can get calculate $\theta$ as

$$\theta = \arccos\left[\frac{1}{w}\left(\frac{(x_3 - x_c)(y_4 - y_1)}{(y_c - y_4)} + (x_4 - x_1)\right)\right] \tag{5.7.2}$$

Now that we have $\theta$ we can just use the perspective equation to correct for the distortion. We make a grid of pixels with the correct dimensions for the flat face, and for each point $(x', y')$ in the grid, we use the equation to find the pixel $(x, y)$ from the original photograph that corresponds to it and put that pixel value into our new grid. After this is done for all points, the new grid is the undistorted image.

The equations to find the corresponding point from the original photograph are

$$x = \frac{zy' + y_c x' \sin\theta}{z + x' \sin\theta} \tag{5.7.3}$$

$$y = x' \cos\theta + \frac{(x_c - x' \sin\theta)x' \sin\theta}{z + x' \sin\theta} \tag{5.7.4}$$

where $z = w \sin\theta$ is the distance in $z$ separating the near and far sides of the square.

# Chapter 6

# Optical Tomography of a Three Dimensional Foam

## 6.1 Introduction

Three dimensional foams are much more common than two dimensional foams in daily life, but the understanding of their structure and coarsening has long lagged behind that of two dimensional foams. This is due in large part to the greater theoretical complexity of the geometry in three dimensions, as well as the additional experimental challenges of imaging these more complex structures.

As far as structure is concerned, one of the earliest experiments was by Matzke [59], who created a monodisperse foam and painstakingly focused on each bubble,

recording the number of faces and edges. In this way he calculated statistics for $O(10^3)$ bubbles. It was only much later that more practical methods of looking at large numbers of bubbles were developed. Modern methods for looking at the structure of three dimensional foams include: optical tomography [63, 20, 62], X-ray tomography [47, 46, 49, 60, 12], magnetic resonance imaging [32], nuclear magnetic resonance [85], and observation of surface bubbles [25, 35, 93, 24, 18]. These techniques all have limitations. To date, optical tomography has only been able to reconstruct small numbers of bubbles, and most other methods deal primarily with wet foams, and are also often limited to small numbers of bubbles. Only in recent X-ray tomography experiments has it been possible to reconstruct large numbers of bubbles in a dry foam [49].

Foams are not static, but evolve over time through a process known as coarsening [100]. There is gas diffusion between bubbles so that some bubbles grow and other bubbles shrink. Over time the average bubble volume increases. This process is also present in two dimensional foams, and in that case coarsening is described by the remarkable result known as von Neumann's law. This law states that for an ideal dry foam the growth rate of an individual bubble depends only on its number of sides. There have been numerous attempts to extend this law to three dimensions, most of them trying to find some analogue that depends only on the number of faces, or some other topological quantity [36, 11, 37, 30]. There have also been simulations of coarsening in three dimensions, including Monte Carlo [53], Potts model [90], and Surface Evolver [64, 61, 44, 41, 12] simulations. All of these

models were approximations. In 2007, MacPherson and Srolovitz [54] found an exact solution for coarsening in three (and higher) dimensions. Their law takes the form

$$\frac{dV}{dt} = K\left(\sum_{i=1}^{n} e_i - L\right) \tag{6.1.1}$$

where $K$ is a constant of proportionality which is proportional to the film tension, the solubility and diffusivity of the gas in the liquid, and inversely proportional to the film thickness, $e_i$ is the length of edge $i$, and $L$ is a quantity they call the 'mean length', which is related to the size of the bubble. In three dimensions, coarsening of an individual bubble depends not only on topology, but also on the size and shape of a bubble. There have been experiments on coarsening in three dimensions [63, 15, 16, 17, 38, 94, 46], but resolution is not good enough to directly apply Eq. (6.1.1).

In this chapter we develop a method of optical tomography that can produce reconstructed slices of dry foams at a wide range of bubble sizes. This may be useful in the characterization of bubble statistics and coarsening in three dimensional foams.

## 6.2 Materials and Methods

Our apparatus consisted of a lightbox to illuminate the sample, a bottle mounted on a rotation stage that was filled with our foam sample, and a camera to image

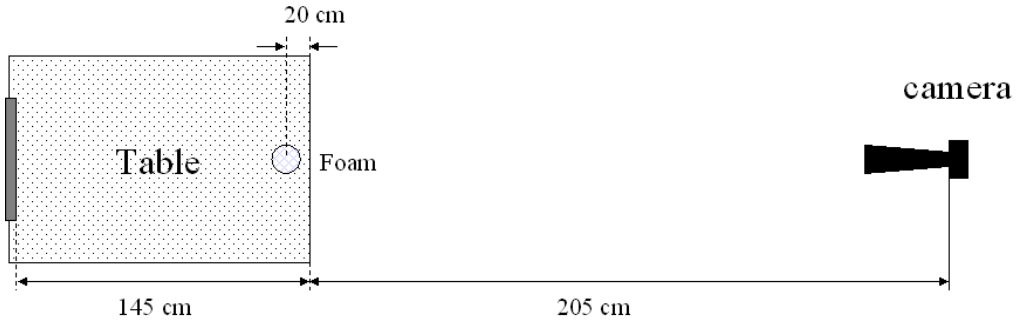


Figure 6.1: Schematic diagram of the tomography setup. Not to scale.

the sample at various angles. The lightbox was placed at one end of an optical table. The Vista Point A lightbox provided a spatially and temporally uniform light source. The rotation stage was mounted 125 cm in front of the lightbox. The ThorLabs CR1-Z6 rotation stage rotated the sample smoothly and with fine angular resolution. The camera was mounted 225 cm in front of the sample. We used a Nikon D70 camera with a Nikkor AF-S 300 mm 1:2.8 D lens. A schematic can be seen in Fig. 6.1

To allow for accurate reconstruction, it was important that all components of the apparatus were accurately aligned. The rotation stage was mounted on posts with lock washers. By carefully adjusting the tightness of the mounting screws, the level of the rotation stage could be carefully set. A metal plate was attached on the top of the rotation stage, and a special mount was connected to this plate, which allowed the bottles containing the foam samples to be rigidly attached to the rotation stage in a level position. In order to align the camera so that the vertical axis of the camera corresponded to the axis of rotation of the rotation stage, an

empty bottle marked with a crosshair was put into the apparatus. The camera was adjusted until the height of the crosshair in the photographs did not change as the bottle was rotated.

To create our foam, we made a solution consisting of 78% deionized water, 19% glycerin, and 3% Ivory ultra concentrated dish detergent. This solution creates a foam that is stable and long lived. Foams will be stable without ruptures for up to a month. To prepare a sample, 384 mL of solution were put into a plastic two liter soda bottle. To create the foam, the bottle was shaken vigorously until the bottle was filled with a uniform, opaque foam of sub-millimeter bubbles. This sample was left to drain and coarsen for up to a week until the average bubble radius was of order centimeters and tomography could be performed.

To collect data, both the camera and rotation stage were simultaneously controlled through a LabVIEW program. The program caused the rotation stage to rotate a set interval, then once the stage had come to a complete stop a photograph was taken. A sample photograph can be seen in Fig. 6.2. This process was repeated until the bottle had been rotated a total angle of $\pi$. The bottle only needed to be rotated through a total angle of $\pi$, rather than $2\pi$, because a photograph corresponding to an angle $\theta$ is functionally equivalent to a photograph corresponding to an angle of $2\pi - \theta$. These two photographs are just mirror images of each other, and as will become clear in the section on the reconstruction method, will have the same contribution to the final reconstruction. For this experiment, the total

number of photographs taken for each run is 720. Examples of reconstructed slices made using different numbers of photographs can be seen in Fig. 6.3. Taking more photographs than this does not significantly change the quality of the image, but does significantly increase analysis time, while taking fewer results in images of a lower quality. The differences in image quality may not be immediately apparent in images scaled down to figure size, but when attempts are made to do any kind of image analysis on the images, the difference becomes clear. The time necessary to take 720 images is on the order of 5 minutes, during which time minimal coarsening occurs. Topological processes are also unlikely to occur in this time window.

## 6.3 Reconstruction

Tomographic reconstruction typically involves reconstructing materials with different absorption coefficients. The case for foam is simpler. If a ray of light does not encounter any Plateau borders on its straight line path to the camera, it arrives with the same intensity that it left. If it encounters a Plateau border at any point on its path, it is scattered and that pixel is black. In practice, scattered light can reach the camera, there can be specular reflection off of films angled closely to the light, and other complications. However, even without accounting for these factors we are able to obtain a reasonable reconstruction of the interior of the foam. To do our reconstruction, we consider a single pixel height at a time. To reconstruct a given height, $z_n$, consider the line of pixels at that height from a given photograph.

Figure 6.2: Sample photograph of bottle filled with foam sample. 720 similar photographs taken at regular angle intervals are used in the reconstruction of the foam sample slices.

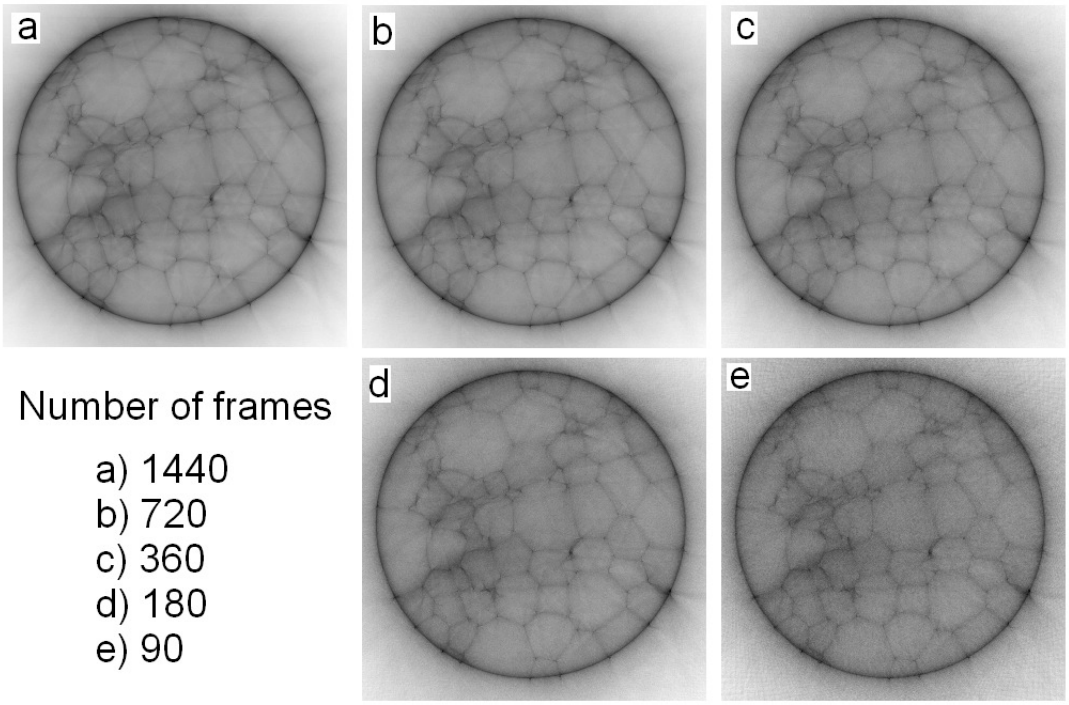


Figure 6.3: Reconstructed slices made using different number of input photographs. All reconstructions correspond to a total angular interval of $\pi$. Reconstructions made with few images are grainy and low contrast, while reconstructions with many images require significant processing time.

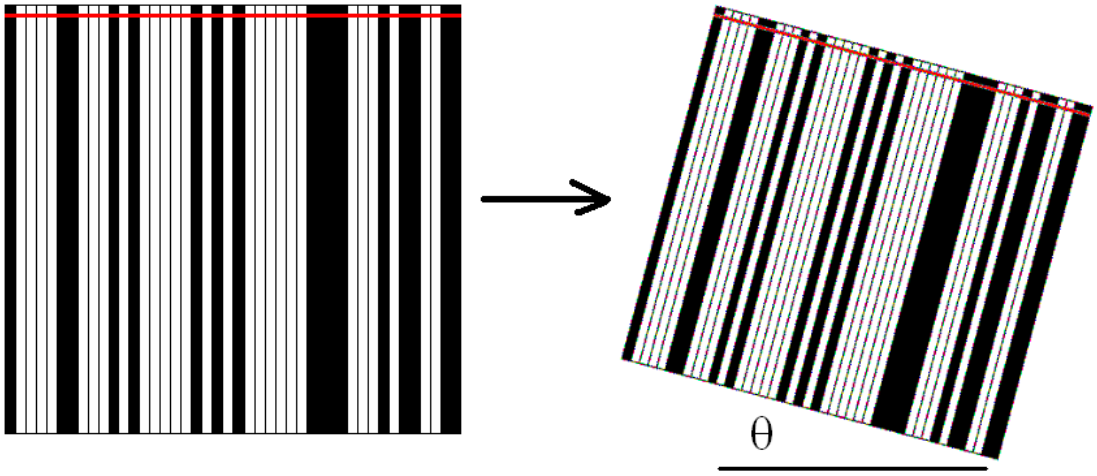


Figure 6.4: Schematic representation of the reconstruction process. The single horizontal row of pixels from a photograph is shown above the red line. This row of pixels is extended into a square. The square is then rotated according to the orientation of the photograph as recorded by the rotation stage. The reconstructed slice is the summation of these rotated squares for all photographs.

We know that if a pixel is dark there is a Plateau border somewhere along that path, and if there is no obstruction along that path then the pixel is light. To reflect this fact we expand the line of pixels to a square by repeating the line of pixels. Then this square is rotated to account for its orientation as measured by the position of the rotation stage. A schematic representation of this process can be seen in Fig. 6.4. This is done for all photographs, resulting in a number of squares equal to the number of photographs. These squares are then summed to produce a reconstructed slice. An example of a reconstructed slice can be seen in Fig. 6.5. This can be repeated for all heights of the bottle, allowing for a reconstruction of the entire sample. A vertical slice through the bottle, compiled from reconstructed horizontal slices, can be seen in Fig. 6.6.

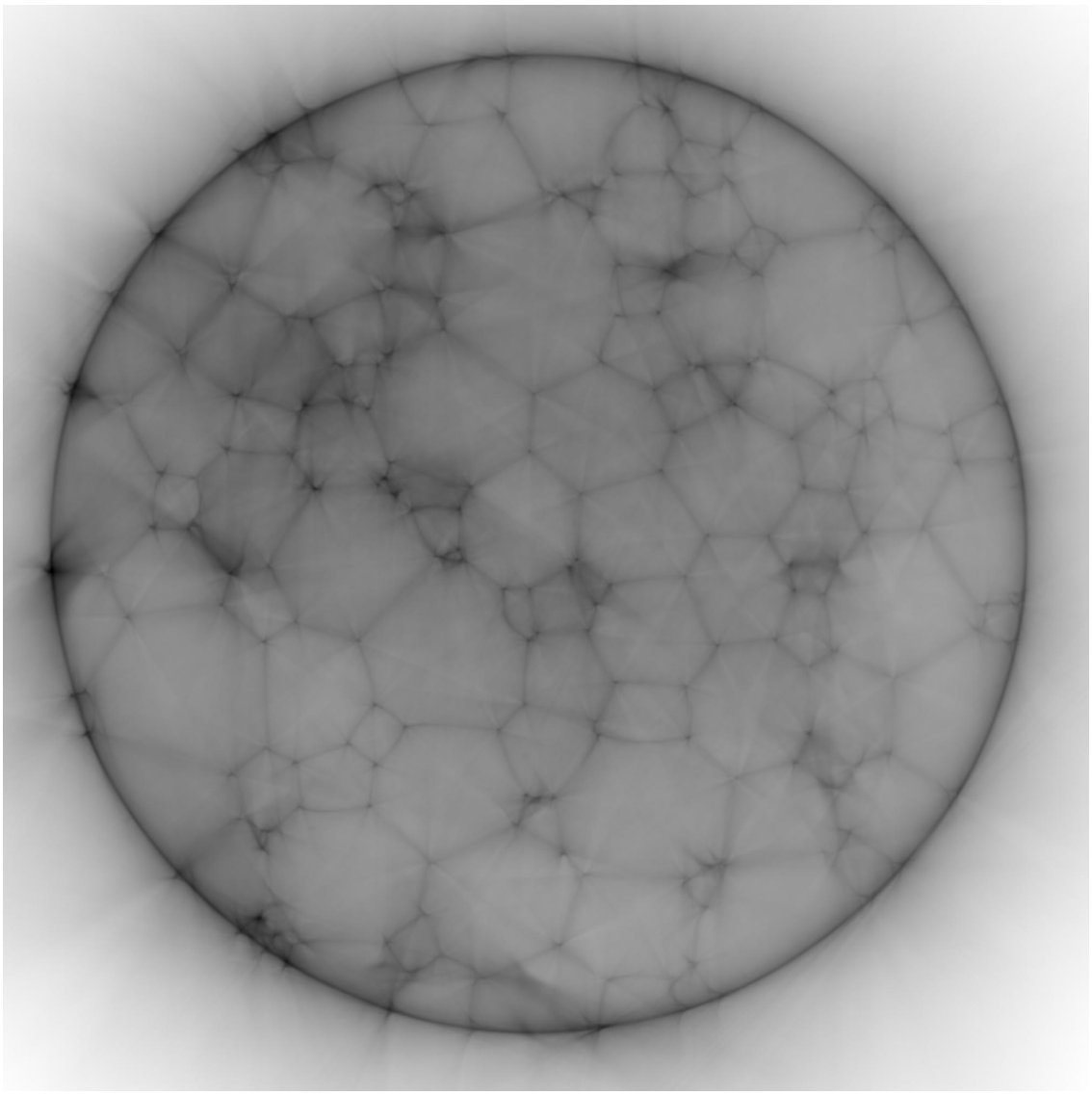

Figure 6.5: An example of a reconstructed horizontal slice.

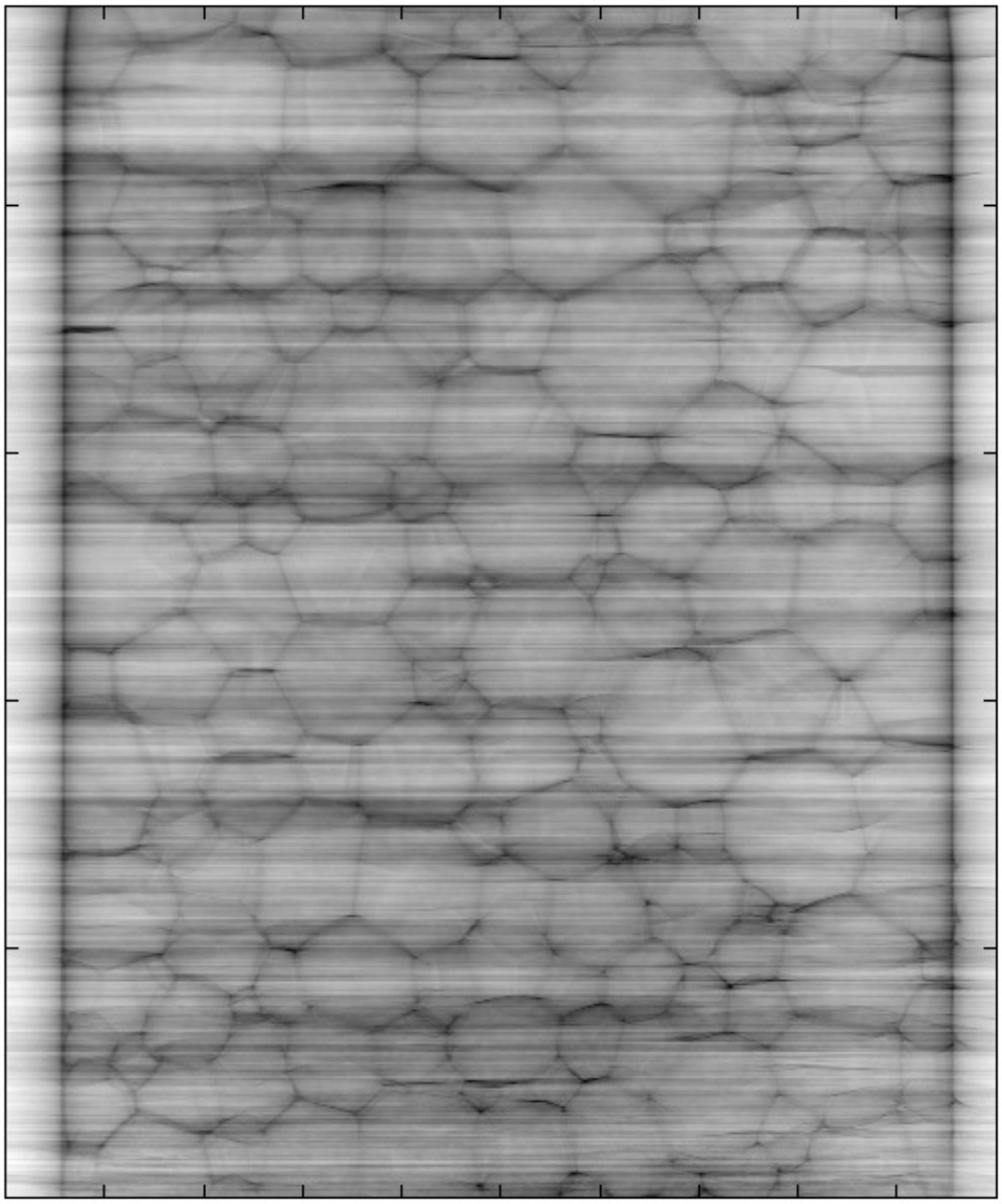

Figure 6.6: A reconstructed vertical slice of a bottle. This is made by stacking all of the horizontal reconstructed slices and taking a vertical slice of that stack. The 'streaky' appearance of this reconstruction is due to the fact that the average intensity of each horizontal slice is determined by the total amount of scattering material at that height.

The reconstructed slices of the sample show the interior structure of the foam in a way that is clearly identifiable by eye. However, these are low contrast, noisy images that are difficult to work with. Correctly identifying all Plateau borders in a single slice with no false positives is a very challenging task. However, this kind of accuracy is not necessary to properly reconstruct the foam. We know that Plateau borders are continuous across slices, with four Plateau borders meeting at an angle of $\arccos(-1/3)$ to create a vertex. If a Plateau border is missed in an individual slice, it can be extrapolated from the Plateau borders in the above and below slices, and if a Plateau border is incorrectly identified, it can be discarded from the fact that nearby slices do not also identify it. By applying Plateau's rules directly into the analysis, it may be possible to correctly reconstruct the structure of the foam, even though successful reconstruction of individual slices is extremely difficult.

## 6.4 Conclusion

Using optical tomography we were able to reconstruct horizontal slices of a three dimensional foam sample. Our technique allows for the use of very dry foams at a wide range of average bubble size. Our technique allows us to collect data at a rate much faster than the coarsening process. The resulting reconstructed slices clearly show the internal structure of the foam. By incorporating Plateau's laws into the image analysis, it may be possible to fully reconstruct the internal structure of the foam sample.

Once the structure of the foam can be reconstructed, many avenues of analysis are possible. Measurements of various statistical quantities can be made to characterize the scaling state of a three dimensional foam. This includes topological distributions such as the bubble edge number distribution, or the bubble face number distribution, or some correlations in these, as for a three dimensional analogue of the Aboav-Weaire law. There are also size distributions, such as the bubble volume distribution, or the surface area distribution. It is also possible to look at size-topology correlations, as for a three dimensional analogue of Lewis' law or Desch's law. Shape characteristics could also be measured, such as aspect ratio or elongation. In addition to these characterizations of the scaling state, dynamics may also be measured. The data collection time is small compared to the rate of coarsening, so it should be possible to analyze data at closely separated times and observe how bubble volume or other bubble measurements change over time. Much of the analytical framework applied to two dimensional foams could thus be extended to describe and characterize three dimensional foams.

## 6.5 Appendix: Determination of Axis

Due to our careful leveling and alignment of the rotation stage and camera, the axis of rotation is parallel to the center axis of the camera. However, this does not mean that they are identical. It is necessary in the reconstruction to define the correct axis of rotation. To determine this we look at the initial photograph of

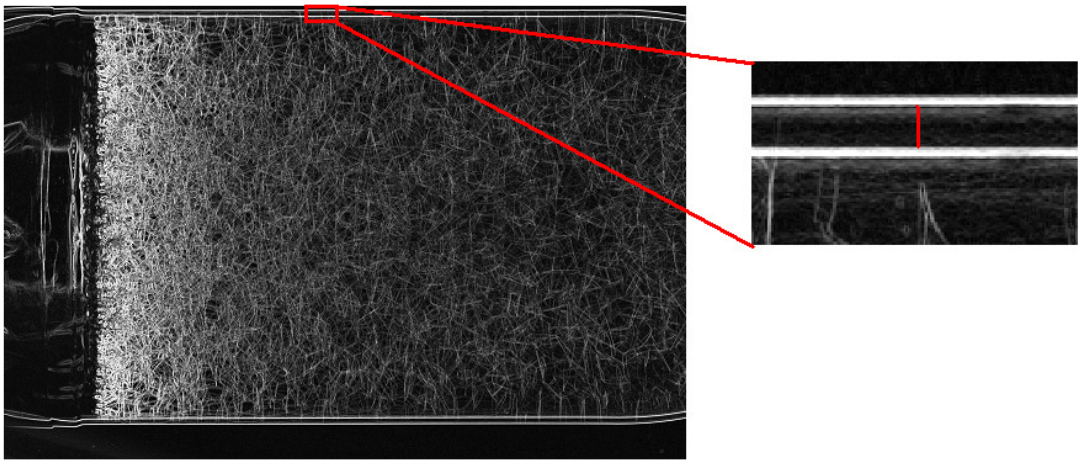

Figure 6.7: Superimposed photographs of a foam sample and the same sample after rotation by $\pi$. These photographs are shown after contrast enhancement. Callout highlights the separation of the bottle edges. The distance between them is twice the distance between the rotation axis and the central axis of the camera.

the bottle and at a photograph taken when the stage is rotated by $\pi$. Because the bottle is symmetric, if the rotation axis corresponds to the center line of the camera, the outline of the bottle will fall on top of itself in these two photographs. If the camera axis is offset from the rotation axis, there will be an apparent translation of the bottle. To measure this, we enhance the contrast of these two photographs and look at the edge of the bottle in each. The distance separating them is twice the distance between the axes. An illustration of this process is shown in Fig. 6.7

## 6.6 Appendix: Lightbox Distance

The tomography process is based on the scattering of light by the sample. An assumption made in the reconstruction is that the incident light is parallel. If the

light is not parallel then the value of a pixel does not correspond to a single section of foam, but instead receives contribution from all the various paths that terminate at that point. If the lightbox is moved too close to the sample, this becomes an issue and the image of the sample foam becomes washed out. The resulting reconstruction is also lacking in detail. This effect is illustrated in Fig. 6.8.

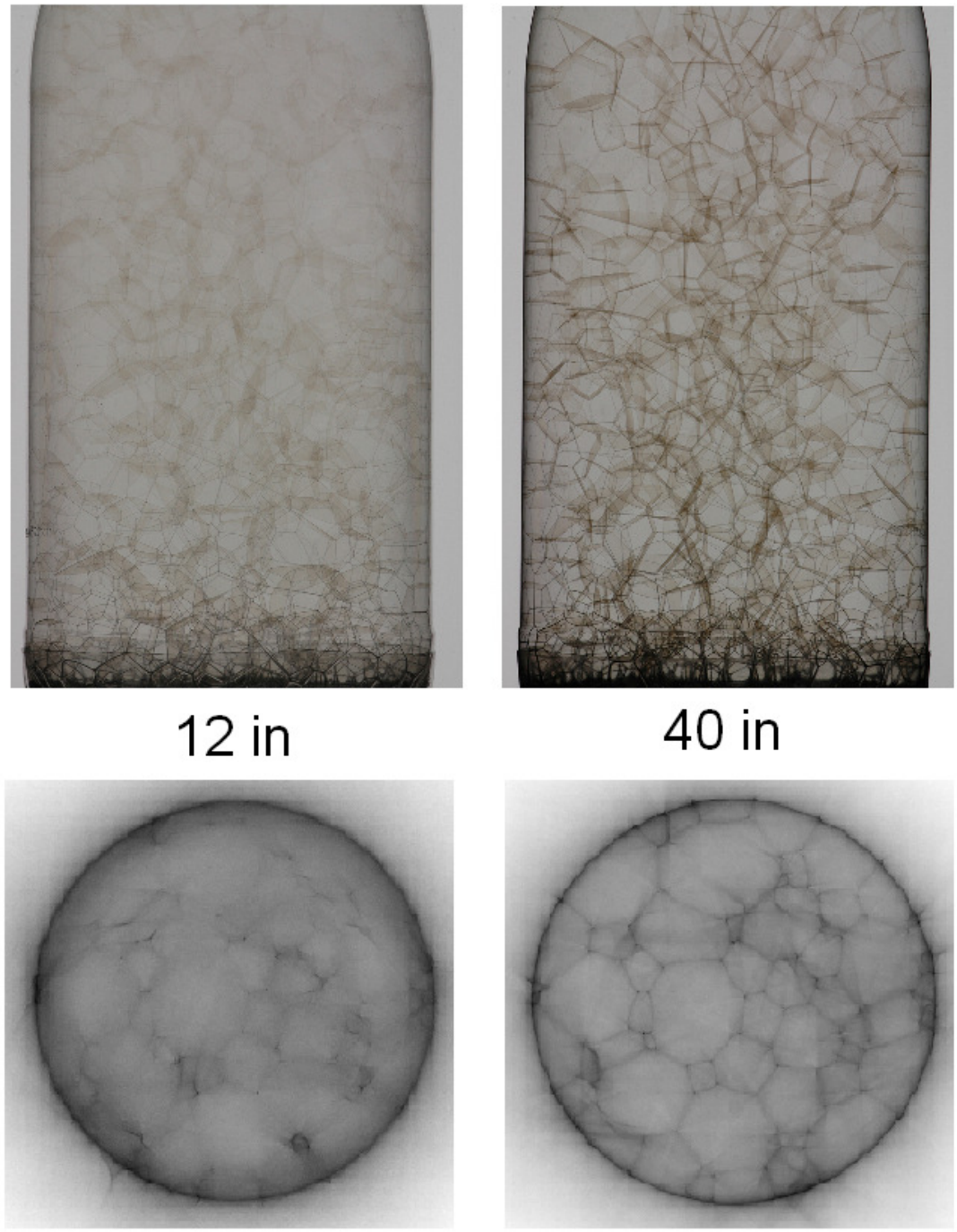


Figure 6.8: Sample photograph and sample reconstructed slice for a bottle that is 12 inches in front of the lightbox and for a bottle that is 40 inches in front of the lightbox. The distance from the bottle to the camera is the same in both cases.

# Chapter 7

# Summary and Conclusion

In this work I have done experiments to characterize foam structure and to describe and model situations of foam coarsening where von Neumann's law does not directly apply.

While von Neumann's law describes ideal, dry, two-dimensional foams, it is possible to construct experiments to see how foam behaves when some of the assumptions underlying von Neumann's law no longer hold. In this way we can gain some insight into the non-ideal effects that are commonly encountered in real world foams. In chapter 2, we varied the liquid content of foams to probe the effect of wetness on structure and coarsening. We found that liquid content does not affect the time-invariant scaling state of the foam, and so we were able to characterize in great detail the statistical properties that describe this unique state that is reached by all

two-dimensional foams when allowed sufficiently long to coarsen. We also observed the effect of liquid content on coarsening. Wetter foams coarsen slower, and very small bubbles deviate from von Neumann's law by coarsening slower than expected. We developed a simple 'border blocking' model that captures these effects. In chapter 3, we looked at other measurements of foam structure, and found that the point pattern of centroids has structure not found in the vertices.

Another assumption of von Neumann's law is that the two-dimensional foam exists in flat space. Avron and Levine [1] developed a modification of von Neumann's law that is applicable to foams that exist in curved space. In chapter 4, we created foams on surfaces of constant positive curvature and observed growth of six-sided bubbles consistent with the modified von Neumann's law. Although foam on our surface will not reach a scaling state due to the dominant growth of large bubbles at late times, at the early times we looked at we found that statistics did not vary with time. We were able to characterize this state, which is distinct from the scaling state of a two-dimensional foam in flat space.

We also looked at a kind of two-dimensional foam that coarsens by a mechanism that is not captured by von Neumann's law. The two-dimensional surface of a three-dimensional foam obeys Plateau's laws, but due to coarsening in the third dimension, does not obey von Neumann's law. In chapter 5, we looked at such a foam. This foam does reach a scaling state, but one that is distinct from the scaling state for an ordinary two-dimensional foam. We were able to measure and

characterize the statistics that define this state. We were also able to measure the coarsening of individual bubbles, which coarsen at a variety of rates, and these rates change over time. Despite this wide variety of coarsening behavior, von Neumann's law did apply on average.

Additionally, von Neumann's law applies to two-dimensional foams, but three-dimensional foams are a subject of great interest. MacPherson and Srolovitz [54] developed a three-dimensional analogue of von Neumann's law that exactly describes the coarsening of ideal dry bubbles. In order to understand structure and coarsening of foams in three-dimensions in the way that we did in two, in chapter 6 we describe a method of optical tomography that allows us to look inside a three-dimensional foam.

To look forward, all of these projects suggest extensions. For our experiment on foam wetness, we developed a model that involved two shape parameters, the circularity and the elongation. We used average values of these parameters, and found good agreement with our data, but our model should be applicable on the individual bubble level. Looking closely at small, wet bubbles, it should be possible to directly measure on an individual bubble level the effect of shape on coarsening rate. Additionally, our model assumes that there is no diffusion across the Plateau borders, but in practice there should be diffusion, only slower. It may be possible to incorporate this additional effect into a more sophisticated model. Also, we only looked at situations where the decoration theorem holds. It may be interesting to

see how things change as the bubbles start to become circular.

We looked at foam in curved geometries only for a single surface of constant positive curvature. We were able to observe deviation from von Neumann's law, but the effect may be more interesting in more complicated geometries. For example, in our dome apparatus, there are no stable stationary bubbles. All bubbles with greater than five sides grow, and bubbles with five or less sides, will always grow or shrink. If a bubble with five or less sides has the area term cancel out the number of sides term, this is unstable. However, in an apparatus with negative curvature, it will be possible to get bubbles that do not have changing area and are stable against perturbations. Also, in a cell with nonconstant curvature, it may be possible to observe bubble segregation and other effects.

We were able to describe the structure and average coarsening behavior of surface foam, but can this give us insight into the bulk behavior? Also we could try to combine this project with the curvature project, and look at the surfaces of three dimensional foams against a curved boundary.

And we have developed a tool to look inside three dimensional foams, but have not yet used it to characterize three dimensional foam structure and coarsening. It is possible to repeat all the kinds of analysis done for the two dimensional foams in three dimensions. We could do a good characterization of the scaling state of three dimensional foam, including topological statistics, such as the distribution of number of edges or faces. We could also look at size distributions, such as

surface area or volume. We could look at correlations between these, such as three dimensional analogues of Lewis' law or Desch's law, or the Aboav-Weaire law. We could also look at coarsening, including at an individual bubble level.

Beyond these established projects, von Neumann's law can be broken in other ways. This includes looking looking at boundary bubbles, which do not diffuse gas across the impermeable boundary. Additionally, the films meet the boundary at an angle of $\pi/2$, which changes the geometry of these kinds of bubbles. Another possibility is quasi-two-dimensional bubbles that do not have a constant height. Foams in a cell like this will have an inherent direction, the gradient of the cell, that will cause the orientation of a bubble to matter for its coarsening. It is also possible to look at foams with a gradient in liquid fraction, so that the position of the bubble matters for its coarsening.

Von Neumann's law is an amazing result, but it is only the beginning.

# Bibliography

[1] Avron, J.E., Levine, D. (1992) Geometry and foams - 2D dynamics and 3D statics. *Phys. Rev. Lett.* 69: 208-211.

[2] Beenakker, C.W.J. (1986) Evolution of two-dimensional soap-film networks. *Phys. Rev. Lett.* 57: 2454-2457.

[3] Berge, B., Simon, A.J., Libchaber, A. (1990) Dynamics of gas-bubbles in monolayers. *Phys. Rev. A* 41: 6893-6900.

[4] Bolton, F., Weaire, D. (1991) The effects of Plateau borders in the 2-dimensional soap froth. 1. Decoration theorem and diffusion lemma. *Philos. Mag. B* 63: 795-809.

[5] Bolton, F., Weaire, D. (1992) The effects of Plateau borders in the 2-dimensional soap froth. 2. General simulation and analysis of rigidity loss transition. *Philos. Mag. B* 65: 473-487.

[6] Chang, R.C., Schoen, H.M., Grove, C.S. (1956) Bubble size and bubble size determination. *Industrial and Engineering Chemistry* 48: 2035-2039.

[7] Cheng, H.C., Lemlich, R. (1983) Errors in the measurement of bubble-size distribution in foam. *Industrial and Engineering Chemistry Fundamentals* 22: 105-109.

[8] Chiu, S.N. (1995) Aboav-Weaire's and Lewis' laws - a review. *Materials Characterization* 34: 149-165.

[9] Clark, N.O., Blackman, M. (1948) The degree of dispersion of the gas phase in foam. *Transactions of the Faraday Society* 44: 1-7.

[10] Clusel, M., Corwin, E.I., Siemens, A.O.N., Brujic, J. (2009) A 'granocentric' model for random packing of jammed emulsions. *Nature* 460: 611-615.

[11] Cox, S.J., Fortes, M.A. (2003) Properties of three-dimensional bubbles of constant mean curvature. *Philos. Mag. Lett.* 83: 281-287.

[12] Davies, I.T., Cox, S.J., Lambert, J. (2013) Reconstruction of tomographic images of dry aqueous foams. *Coll. and Surf. A* In press.

[13] Duplat, J., Bossa, B., Villermaux, E. (2011) On two-dimensional foam ageing. *J. Fluid Mech.* 673: 147-179.

[14] Durand, M., Käfer, J., Quilliet, C., Cox, S., Talebi, S.A., Graner, F. (2011) Statistical mechanics of two-dimensional shuffled foams: prediction of the correlation between geometry and topology. *Phys. Rev. Lett.* 107: 168304.

[15] Durian, D.J., Weitz, D.A., Pine, D.J. (1990) Dynamics and coarsening in 3-dimensional foams. *J. Phys. Condens. Matter* 2: 433-436.

[16] Durian, D.J., Weitz, D.A., Pine, D.J. (1991) Multiple light-scattering probes of foam structure and dynamics. *Science* 252: 686-688.

[17] Durian, D.J., Weitz, D.A., Pine, D.J. (1991) Scaling behavior in shaving cream. *Phys. Rev. A* 44: 7902-7905.

[18] Feitosa, K., Durian, D.J. (2008) Gas and liquid transport in steady-state aqueous foam. *Eur. Phys. J. E* 26: 309-316.

[19] Feitosa, K., Halt, O.L., Kamien, R.D., Durian, D.J. (2006) Bubble kinetics in a steady-state column of aqueous foam. *Europhys. Lett.* 76: 683-689.

[20] Fetterman M., Tan, E., Ying, L., Stack, R., Marks, D., Feller, S., Cull, E., Sullivan, J., Munson, D., Thoroddsen, S., Brady, D. (2000) Tomographic imaging of foam. *Optics Express* 7: 186-197.

[21] Flyvbjerg, H. (1993) Model for coarsening froths and foams. *Phys. Rev. E* 47: 4037-4054.

[22] Fortes, M.A., Rosa, M.E., Afonso, L. (2002) Ageing of two-dimensional clusters of bubbles. *Philos. Mag. A* 82: 527-539.

[23] Fortuna, I., Thomas, G.L., de Almeida, R.M.C., Graner, F. (2012) Growth laws and self-similar growth regimes of coarsening two-dimensional foams: transition from dry to wet limits. *Phys. Rev. Lett.* 108: 248301.

[24] Gañán-Calvo, A.M., Fernandez, J.M., Marquez Oliver, A., Marquez, M. (2004) Coarsening of monodisperse wet microfoams. *Appl. Phys. Lett.* 84: 4989-4991.

[25] Gardiner, B.S., Dlugogorski, B.Z., Jameson, G.J. (2000) Coarsening of two- and three-dimensional wet polydisperse foams. *Philos. Mag. A* 80: 981-1000.

[26] Glazier, J.A., Anderson, M.P., Grest, G.S. (1990) Coarsening in the 2-dimensional soap froth and the large-Q Potts-model - a detailed comparison. *Philos. Mag. B* 62: 615-645.

[27] Glazier, J.A., Gross, S.P., Stavans, J. (1987) Dynamics of two-dimensional soap froths. *Phys. Rev. A* 36: 306-312.

[28] Glazier, J.A., Stavans, J. (1989) Nonideal effects in the two-dimensional soap froth. *Phys. Rev. A* 40: 7398-7401.

[29] Glazier, J.A., Weaire, D. (1992) The kinetics of cellular-patterns. *J. Phys.: Condens. Matter* 4: 1867-1894.

[30] Glicksman, M.E. (2005) Analysis of 3-D network structures. *Philos. Mag.* 85: 3-31.

[31] Glicksman, M.E., Rios, P.R., Lewis, D.J. (2007) Regular N-hedra: A topological approach for analyzing three-dimensional textured polycrystals. *Acta Materialia* 55: 4167-4180.

[32] Gonatas, C.P., Leigh, J.S., Yodh, A.G., Glazier, J.A., Prause, B. (1995) Magnetic-resonance images of coarsening inside a foam. *Phys. Rev. Lett.* 75: 573-576.

[33] Graner, F., Jiang, Y., Janiaud, E., Flament, C. (2001) Equilibrium states and ground state of two-dimensional fluid foams. *Phys. Rev. E* 63: 011402.

[34] Herdtle, T., Aref, H. (1992) Numerical experiments on 2-dimensional foam. *J. Fluid Mech.* 241: 233-260.

[35] Hilgenfeldt, S., Koehler, S.A., Stone, H.A. (2001) Dynamics of coarsening foams: Accelerated and self-limiting drainage. *Phys. Rev. Lett.* 86: 4704-4707.

[36] Hilgenfeldt, S., Kraynik, A.M., Koehler, S.A., Stone, H.A. (2001) An accurate von Neumann's law for three-dimensional foams. *Phys. Rev. Lett.* 86: 2685-2688.

[37] Hilgenfeldt, S., Kraynik, A.M., Reinelt, D.A., Sullivan, J.M. (2004) The structure of foam cells: Isotropic Plateau polyhedra. *Europhys. Lett.* 67: 484-490.

[38] Hutzler, S., Weaire, D. (2000) Foam coarsening under forced drainage. *Philos. Mag. Lett.* 80: 419-425.

[39] de Icaza, M., Jiménez-Ceniceros, A., Castaño, V. M. (1994) Statistical distribution functions in 2D foams. *J. Appl. Phys.* 76: 7317-7321.

[40] Jashnani, I.L., Lemlich, R. (1974) Foam drainage, surface viscosity, and bubble size bias. *Colloid and Interface Science* 46: 13-16.

[41] Jurine, S., Cox, S., Graner, F. (2005) Dry three-dimensional bubbles: growth-rate, scaling state and correlations. *Coll. and Surf. A* 263: 18-26.

[42] Kellaway, G.P. (1946) *Map Projections* (Methuen and Co. Ltd., London).

[43] Kermode, J.P., Weaire, D. (1990) 2D-froth - a program for the investigation of 2-dimensional froths. *Computer Phys. Comm.* 60: 75-109.

[44] Kraynik, A.M., Reinelt, D.A., van Swol, F. (2004) Structure of random foam. *Phys. Rev. Lett.* 93: 208301.

[45] Krichevsky, O., Stavans, J. (1992) Coarsening of 2-dimensional soap froths in the presence of pinning centers. *Phys. Rev. B* 46: 10579-10582.

[46] Lambert, J., Cantat, I., Delannay, R., Mokso, R., Cloetens, P., Glazier, J.A., Graner, F. (2007) Experimental growth law for bubbles in a moderately 'wet' 3D liquid foam. *Phys. Rev. Lett.* 99: 058304.

[47] Lambert, J., Cantat, I., Delannay, R., Renault, A., Graner, F., Glazier, J.A., Veretennikov, I., Cloetens, P. (2005) Extraction of relevant physical parameters from 3D images of foams obtained by X-ray tomography. *Coll. and Surf. A* 263: 295-302.

[48] Lambert, J., Graner, F., Delannay, R., Cantat, I. (2012) Experimental link of coarsening rate and volume distribution in dry foam. *Europhys. Lett.* 99: 48003.

[49] Lambert, J., Mokso, R., Cantat, I., Cloetens, P., Glazier, J.A., Graner, F., Delannay, R. (2010) Coarsening foams robustly reach a self-similar growth regime. *Phys. Rev. Lett.* 104: 248304.

[50] Levine, D., Avron, J.E., Brokman, A. (1992) Grain growth on curved surfaces. *Mater. Sci. Forum* 96: 281-284.

[51] Lewis, F.T. (1928) The correlation between cell division and the shapes and sizes of prismatic cells in the epidermis of cucumis. *Anat. Rec.* 38: 341-376.

[52] Lewis, F.T. (1930) A volumetric study of growth and cell division in two types of epithelium,the longitudinally prismatic epidermal cells of Tradescantia and the radially prismatic epidermal cells of Cucumis. *Anat. Rec.* 47: 59-99.

[53] Liu, G.Q., Yu, H.B., Song, X.Y., Qin, X.G. (2001) A new model of three-dimensional grain growth: theory and computer simulation of topology-dependency of individual grain growth rate. *Materials and Design* 22: 33-38.

[54] MacPherson, R.D., Srolovitz, D.J. (2007) The von Neumann relation generalized to coarsening of three-dimensional microstructures. *Nature* 446: 1053-1055.

[55] Mancini, M., Oguey, C. (2005) Foams in contact with solid boundaries: Equilibrium conditions and conformal invariance. *Eur. Phys. J. E* 17: 119-128.

[56] Mancini, M., Oguey, C. (2005) Equilibrium conditions and symmetries for foams in contact with solid surfaces. *Coll. and Surf. A* 263: 33-38.

[57] Mancini, M., Oguey, C. (2007) Decorated vertices with 3-edged cells in 2D foams: exact solutions and properties. *Eur. Phys. J. E* 22: 181-192.

[58] Marchalot, J., Lambert, J., Cantat, I., Tabeling, P., Jullien, M.-C. (2008) 2D foam coarsening in a microfluidic system. *Europhys. Lett.* 83: 64006.

[59] Matzke, E.B. (1946) The 3-dimensional shape of bubbles in foam - an analysis

of the role of surface forces in 3-dimensional cell shape determination. *Am. J. Botany* 33: 58-80.

[60] Meagher, A.J., Mukherjee, M., Weaire, D., Hutzler, S., Banhart, J., Garcia-Moreno, F. (2011) Analysis of the internal structure of monodisperse liquid foams by X-ray tomography. *Soft Matter* 7: 9881-9885.

[61] Monnereau, C., Pittet, N., Weaire, D. (2000) An analysis of surface curvature and growth laws for foam cells using the Surface Evolver. *Europhys. Lett.* 52: 361-367.

[62] Monnereau, C., Prunet-Foch, B., Vignes-Adler, M. (2001) Topology of slightly polydisperse real foams. *Phys. Rev. E* 63: 061402.

[63] Monnereau, C., Vignes-Adler, M. (1998) Dynamics of 3D real foam coarsening. *Phys. Rev. Lett.* 80: 5228-5231.

[64] Monnereau, C., Vignes-Adler, M., Pittet, N. (1999) Coarsening of a three-dimensional reconstructed foam under Surface Evolver. *Philos. Mag. B* 79: 1213-1222.

[65] Moore, B., Knobler, C.M., Broseta, D., Rondelez, F. (1986) Studies of phase-transitions in Langmuir monolayers by fluorescence microscopy. *J. Chem. Soc. Faraday Trans. II* 82: 1753.

[66] Neubert, L., Schreckenberg, M. (1997) Numerical simulation of two-dimensional soap froth. *Physica A* 240: 491-502.

[67] von Neumann, J. (1952) in *Metal Interfaces* (American Society for Metals, Cleveland), pp 108-110.

[68] Newhall, K.A., Pontani, L.L., Jorjadze, I., Hilgenfeldt, S., Brujic. J., (2012) Size-topology relations in packings of grains, emulsions, foams, and biological cells. *Phys. Rev. Lett.* 108: 268001.

[69] Palmer, M.A., Glicksman, M.E., Rajan, K. (1999) Grain Growth of thin films conforming to a curved surface. *Philos. Mag. A* 79: 763-774.

[70] Peczak, P., Grest, G.S., Levine, D. (1993) Monte-Carlo studies of grain-growth on curved surfaces. *Phys. Rev. E* 48: 4470-4482.

[71] Quilliet, C., Ataei Talebi, S., Rabaud, D., Käfer, J., Cox, S.J., Graner, F. (2008) Topological and geometrical disorders correlate robustly in two-dimensional foams. *Philos. Mag. Lett.* 88: 9-10.

[72] Rivier, N. (1985) Statistical crystallography - structure of random cellular networks. *Philos. Mag. B* 52: 795-819.

[73] Rivier, N., Lissowski, A. (1982) On the correlation between sizes and shapes of cells in epithelial mosaics. *J. Phys. A: Math. Gen.* 15: 143-148.

[74] Rosa, M.E., Afonso, L., Fortes, M.A. (2002) Aging of free bubble clusters. *Philos. Mag. A* 82: 2953-2963.

[75] Rosa, M.E., Fortes, M.A. (1999) Coarsening of two-dimensional foams confined by walls. *Philos. Mag. A* 79: 1871-1886.

[76] Roth, A.E., Jones, C.D., Durian, D.J. (2012) Coarsening of a two-dimensional foam on a dome. *Phys. Rev. E* 86: 021402.

[77] Roth, A.E., Jones, C.D., Durian, D.J. (2013) Bubble statistics and coarsening dynamics for quasi-two dimensional foams with increasing liquid content. *Phys. Rev. E* 87: 042304.

[78] Rutenberg, A.D., McCurdy, M.B. (2006) Scaling state of dry two-dimensional froths: Universal angle-deviations and structure. *Phys. Rev. E* 73: 011403.

[79] Saraiva, J., Pina, P., Bandeira, L, Antunes, J. (2009) Polygonal networks on the surface of Mars; applicability of Lewis, Desch, and Aboav-Weaire laws. *Philos. Mag. Lett.* 89: 185-193.

[80] Segel, D., Mukamel, D., Krichevsky, O., Stavans, J. (1993) Selection mechanism and area distribution in 2-dimensional cellular structures. *Phys. Rev. E* 47: 812-819.

[81] Stavans, J. (1990) Temporal evolution of 2-dimensional drained soap froths. *Phys. Rev. A* 42: 5049-5051.

[82] Stavans, J. (1993) The evolution of cellular structures. *Rep. Prog. Phys.* 56: 733-789.

[83] Stavans, J. (1993) Evolution of 2-dimensional cellular structures - the soap froth. *Physica A* 194: 307-314.

[84] Stavans, J., Glazier, J.A. (1989) Soap froth revisited - dynamic scaling in the two-dimensional froth. *Phys. Rev. Lett.* 62: 1318-1321.

[85] Stevenson, P., Sederman, A.J., Mantle, M.D., Li, X., Gladden, L.F. (2010) Measurement of bubble size distribution in a gas-liquid foam using pulsed-field gradient nuclear magnetic resonance. *J. Coll. and Interface Sci.* 352: 114-120.

[86] Stine, K.J., Rauseo, S.A., Moore, B.G. (1990) Evolution of foam structures in Langmuir monolayers of pentadeconoic acid. *Phys. Rev. A* 41: 6884-6892.

[87] Stine, K.J., Rauseo, S.A., Moore, B.G., Wise, J.A., Knobler, C.M. (1990) Evolution of foam structures in Langmuir monolayers of pentadeconoic acid. *Phys. Rev. A* 41: 6884-6892.

[88] Szeto, K.Y., Tam, W.Y. (1995) Lewis' law versus Feltham's law in soap froth. *Physica A* 221: 256-262.

[89] Teixeira, P.I.C., Fortes, M.A. (2005) Decoration Plateau borders in two-dimensional liquid foams: geometry and excess energy. *Philos. Mag.* 85: 1303-1322.

[90] Thomas, G.L., de Almeida, R.M.C., Graner, F. (2006) Coarsening of three-dimensional grains in crystals, or bubbles in dry foams, tends towards a universal, statistically scale-invariant regime. *Phys. Rev. E* 74: 021407.

[91] Torquato, S., Stillinger, F.H. (2003) Local density fluctuations, hyperuniformity, and order metrics. *Phys. Rev. E* 68: 041113.

[92] Vera, M.U., Durian, D.J. (1996) Angular distribution of diffusely transmitted light. *Phys. Rev. E* 53: 3215-3224.

[93] Vera, M.U., Durian, D.J. (2002) Enhanced drainage and coarsening in aqueous foams. *Phys. Rev. Lett.* 88: 088304.

[94] Vera, M.U., Saint-Jalmes, A., Durian, D.J. (2001) Scattering optics of foam. *Applied Optics* 40: 4210-4214.

[95] de Vries, A.J. (1957) *Foam Stability* (Rubber-Stichting, Delft).

[96] de Vries, A.J. (1972) in *Adsorptive Bubble Separation Techniques* (Academic Press, New York), ch 2.

[97] Wang, Y., Neethling, S.J. (2006) Simulating realistic froth surfaces. *Minerals Engineering* 19: 1069-1076.

[98] Wang, Y., Neethling, S.J. (2009) The relationship between the surface and internal structure of dry foam. *Coll. and Surf. A* 339: 73-81.

[99] Weaire, D. (1999) The equilibrium structure of soap froths: inversion and decoration. *Philos. Mag. Lett.* 79: 491-495.

[100] Weaire, D., Hutzler, S. (1999) *The Physics of Foams* (Oxford University Press, New York).

[101] Zachary, C.E., Jiao, Y., Torquato, S. (2011) Hyperuniform long-range correlations are a signature of disordered jammed hard-particle packings. *Phys. Rev. Lett.* 106: 178001.

[102] Zachary, C.E., Jiao, Y., Torquato, S. (2011) Hyperuniformity, quasi-long-range correlations, and void-space constraints in maximally random jammed particle packings. I. Polydisperse spheres. *Phys. Rev. E* 83: 051308.

[103] Zachary, C.E., Jiao, Y., Torquato, S. (2011) Hyperuniformity, quasi-long-range correlations, and void-space constraints in maximally random jammed particle packings. II. Anisotropy in particle shape. *Phys. Rev. E* 83: 051309.

[104] Zachary, C.E., Torquato, S. (2009) Hyperuniformity in point patterns and two-phase random heterogeneous media. *J. Stat. Mech.* P12015.